Title
Thermal Conductivity Measurements Across a Pressure-Induced Phase Transition: Application to Heat Flow in Earth's Interior

Author
McGuire, Christopher

Publication Date
2018

Peer reviewed|Thesis/dissertation

UNIVERSITY OF CALIFORNIA
Los Angeles

Thermal Conductivity Measurements Across a Pressure-Induced Phase Transition: Application to Heat Flow in Earth's Interior

A dissertation submitted in partial satisfaction
of the requirements for the degree
Doctor of Philosophy in Geology

by

Christopher McGuire

2018

ABSTRACT OF THE DISSERTATION

Thermal Conductivity Measurements Across a Pressure-Induced Phase Transition: Application to Heat Flow in Earth's Interior

by

Christopher McGuire
Doctor of Philosophy in Geology
University of California, Los Angeles, 2018
Professor Abby Kavner, Chair

The thermal conductivity of minerals in Earth's lowermost mantle is important for the thermal and chemical evolution of Earth. In the thermal boundary layer separating the core and mantle, the bulk thermal conductivity helps determine the heat flux out of the core. The core heat flux is an important unknown, which has implications for the energy available to power the core geodynamo, the age of the solid inner core, and the style of mantle convection. Measurements of thermal conductivity at high pressure and temperature conditions do not agree on the value at CMB conditions, and estimates range from about 5 W/mK to 15 W/mK. Recent experiments have helped constrain the pressure dependence of thermal conductivity at constant temperature. However, phase transitions in mantle minerals, such as the spin transition in ferropericlase, could complicate the extrapolation of lower pressure and temperature measurements to the conditions at the core-mantle boundary (CMB).

In this dissertation, I build on a new method to measure thermal conductivity at high pressures and temperatures using continuous wave laser heating in the diamond anvil cell

and apply it to pressure induced phase transitions. I test the method using the face-centered-cubic (B1) to body-centered-cubic (B2) phase transition in NaCl. This study produced the first measurement of NaCl thermal conductivity across the B1-B2 phase transition.

I use the method developed for ionic salts and apply it to the mantle mineral, ferropericlase, (Mg,Fe)O, over the pressure range of 22 GPa to 61 GPa. This range of pressure includes the reported spin transition of octahedrally coordinated iron, from the high spin state to the mixed spin state. Material properties such as the bulk modulus and sound velocity decrease sharply with pressure in the mixed spin state. I measure a correlative reduction of thermal conductivity with pressure. This measurement is consistent with independent thermo-reflectance measurements of ferropericlase thermal diffusivity.

Combining new ferropericlase thermal conductivity measurements with those of bridgmanite, and accounting for the spin transition, an updated thermal conductivity profile for the mantle can be calculated. The spin transition reduction has only a minor effect on the depth dependence of mantle thermal conductivity. This is due to the dominant modal percentage of bridgmanite, which is about 80% of the mantle by volume. Including the spin transition effect, I find an increase in thermal conductivity of the mantle by a factor of about 2 from the top of the lower mantle to the core-mantle boundary. These results are consistent with other recent studies, which use different measurement techniques.

The thermal conductivity depth dependence of ferropericlase and bridgmanite using the methods in this dissertation result in a CMB bulk thermal conductivity of 5.2 W/mK. Accounting for uncertainty in the thickness and temperature change across the CMB, this thermal conductivity maps to a total heat flux of 5.1 to 9.3 TW. This range is consistent

with an old inner core, the crystallization of which has has been integral to powering the geodynamo for a significant portion of Earth's history. Future work to bring existing measurements of thermal conductivity at CMB pressures into agreement will need to resolve questions about the temperature dependence at the extreme conditions of the lowermost mantle.

In a separate study, I use an analogous application of the heat equation to model the mass transport of sediment on hillslopes. Hillslope processes are important for understanding how surface landforms evolve over time. The application of linear diffusion to describe the transport of grains down slope is used to date geomorphic surfaces. However, several lines of evidence, from theoretical considerations, to laboratory experiments and field observations suggest that the linear diffusion equation has limited predictive power for modelling of scarp degradation. Here we use high resolution elevation data and optically stimulated luminescence dates of sediment from a set of terrace risers in New Zealand and show that those degraded terrace risers are better explained by nonlinear diffusion.

The dissertation of Christopher McGuire is approved.

Jonathan M Aurnou

Seulgi Moon

Stuart Brown

Abby Kavner, Committee Chair

University of California, Los Angeles

2018

For Allison, my love

TABLE OF CONTENTS

LIST OF FIGURES

LIST OF TABLES

ACKNOWLEDGMENTS

I thank my advisor, Abby Kavner, for helpful guidance throughout my PhD, in particular, for your patience in helping me find successful avenues of inquiry in mineral physics. Also, thanks for going above and beyond to introduce me to your many friends and colleagues at conferences.

Thanks to David Santamaria-Perez, who provided samples of the mineral xifengite and gave valuable help with analysis of diffraction patterns. Thanks also to Steve Jacobsen, who provided the single-crystal samples of ferropericlase. Martin Kunz and Andrew Doran provided essential support at ALS beamline 12.2.2, including updating software to our specifications. Thanks to Krista Sawchuk for help running experiments and for being a great colleague. I thank my committee members for their guidance throughout the project. Thanks to Seulgi Moon for spending time sharing your knowledge of quantitative geomorphology. Thanks to Jon Aurnou for helpful advice about framing my ideas and for bringing me along in your geodynamo class. Thanks to Stuart Brown for introducing me to excellent reading in solid-state physics. I also would like to thank Ed Rhodes, who enthusiastically accepted me at UCLA, even though I had little formal training, and who introduced me to field geology and luminescence dating.

I am also thankful for the support I have had from friends and colleagues. Thanks to Nathan Brown for our many interesting discussions and help learning LaTeX. Thanks to Adam Makhluf for guidance learning crystal chemistry and for enjoyable discussions about geochemistry. Thanks also to Daniel Fineman and Ellen Alexander for many enjoyable discussions in classes and around the department. Thanks to Ilan Goldstein and Joe Viana, who were always willing to talk about research with me.

I thank my parents and brother for their endless and loving support, and for accepting my plan to return to undergraduate schooling, which was instrumental in my somewhat

unusual path to the study of geology.

Thanks to my wife, Allison, for your patience, kindness and support. I love you!

A version of Chapter 4 was published as: "Isothermal equation of state and phase stability of Fe_5Si_3 up to 96 GPa and 3000 K." by C. McGuire, D. SantamariaPerez, A. Makhluf, & A. Kavner, (2017), Journal of Geophysical Research: Solid Earth.

Chapter 2 has been submitted to Journal of Applied Physics as: "Measurements of NaCl thermal conductivity across the B1-B2 phase transition." by C. McGuire, K. L. Sawchuk, & A. Kavner.

A version of Chapters 3 and 6 is being prepared for submission to Science as: "Thermal conductivity depth profile of Earth's mantle" by C. McGuire, K. L. Sawchuk, Rainey, E. & A. Kavner.

A version of Chapters 5 is being prepared for submission to Geology as: "Evidence for non-linear sediment transport on terrace riser hillslopes, South Island, New Zealand" by C. McGuire, S.G. Moon, R. Zinke, E. J. Rhodes, J. Dolan, A. Hatem, & N. Brown.

VITA

2017 C.Phil (Geology), UCLA, Los Angeles, California.

2009 B.A. (Anthropology), Duke University, Durham, North Carolina.

2015–2018 Graduate Student Researcher. Measurements of thermal conductivity in the diamond anvil cell. Experiments performed at the Advanced Light Source, Lawrence Berkeley National Lab. NSF EAR 1522560

2013–2015 Graduate Student Researcher. Luminescence dating, and fault slip rate determination. Fieldwork in South Island, New Zealand. NSF EAR 1321912

2013–2017 Teaching Assistant, Earth, Planetary, and Space Sciences Department, UCLA. Taught lab sections of mineralogy and igneous petrology.

PUBLICATIONS

McGuire, C., Santamaria-Perez, D., Makhluf, A., Kavner, A. (2017). Isothermal equation of state and phase stability of Fe5Si3 up to 96 GPa and 3000 K. Journal of Geophysical Research: Solid Earth.

Santamaria-Perez, D., Marqueo, T., MacLeod, S., Ruiz-Fuertes, J., Daisenberger, D., Chulia-Jordan, R., ... & **McGuire, C.**, Mahkluf, A. (2017). Structural evolution of CO2-filled pure silica LTA zeolite under high-pressure high-temperature conditions. Chemistry of Materials, 29(10), 4502-4510.

Zinke, R., Dolan, J. F., Rhodes, E. J., Van Dissen, R., **McGuire, C.** (2017). Highly Variable Latest PleistoceneHolocene Incremental Slip Rates on the Awatere Fault at Saxton River, South Island, New Zealand, Revealed by Lidar Mapping and Luminescence Dating. Geophysical Research Letters, 44(22).

Gray, H. J., Tucker, G. E., Mahan, S. A., **McGuire, C.**, & Rhodes, E. J. (2017). On extracting sediment transport information from measurements of luminescence in river sediment. Journal of Geophysical Research: Earth Surface, 122(3), 654-677.

Santamaria-Perez, D., **McGuire, C.**, Makhluf, A., Kavner, A., Chulia-Jordan, R., Jorda, J. L., ... & Munoz, A. (2016). Correspondence: Strongly driven Re+ CO2 redox reaction at high-pressure and high-temperature. Nature Communications, 7, 13647.

Santamaria-Perez, D., **McGuire, C.**, Makhluf, A., Kavner, A., Chulia-Jordan, R., Jorda, J.L., Pellicer-Porres, J., ... & Munoz, A. (2016). Exploring the Chemical Reactivity between Carbon Dioxide and Three Transition Metals (Au, Pt, and Re) at High-Pressure, High-Temperature Conditions. Inorganic chemistry, 55(20), 10793-10799.

McGuire, C., & Rhodes, E. J. (2015). Determining fluvial sediment virtual velocity on the Mojave River using K-feldspar IRSL: Initial assessment. Quaternary International, 362, 124-131.

McGuire, C., & Rhodes, E. J. (2015). Downstream MET-IRSL single-grain distributions in the Mojave River, southern California: Testing assumptions of a virtual velocity model. Quaternary Geochronology, 30, 239-244.

CHAPTER 1

Introduction

1.1 Overview

Physical processes that transfer heat and mass are the fundamental working parts of the study of geology. Many processes unique to Earth among terrestrial planets in the solar system are caused by the dynamic transport of heat and mass on a global scale. Accordingly, geology can be framed as applied thermodynamics and, when thought of this way, the field is furthered by advances in measurement. In this dissertation, I present several novel measurements and measurement techniques that provide new understanding of heat transfer in the deep interior and mass transport on the surface of Earth.

At the planetary scale, dynamic processes are directly related to the cooling of Earth over geologic time. As the planet cools, the temperature difference between the top and the base of the mantle promotes solid-state convection (Lay et al., 2008). Mineral thermal conductivity plays an important at Earth's thermal boundary layers. In the deep interior, the core-mantle boundary (CMB) heat flux is directly related to the thermal conductivity of the minerals stable there.The core's geodynamo, which is responsible for the magnetic field, is directly related to the thermal conductivity of minerals in the core-mantle boundary, where heat is transported principally by conduction (Buffett, 2002). The style of mantle convection can be affected by the depth dependence of mineral thermal expansion and con-

ductivity (Tosi et al., 2013). The shape and extent of mantle plumes can be affected by the spatial pattern of thermal conductivity at the base of the mantle (Ammann et al., 2014). I focus my experiments on the thermal conductivity depth dependence of ferropericlase, a major mantle mineral, with implications for mantle convection and for heat flow across the core-mantle boundary.

The chemistry and physical properties of Earth's core is related to planetary cooling. Earth's core formation likely results in a core and mantle that are not in chemical equilibrium (Karato and Murthy, 1997). Furthermore, as the planet cools, the equilibrium state of the core can change, namely by the growth of the solid, inner core, by reactions between the core and mantle, and by changes in solubility of minor elements in the liquid metal core (Knittle and Jeanloz, 1989; Stixrude et al., 1997; ORourke and Stevenson, 2016). In order to evaluate the composition of the core and how it changes with time, it is important to measure the equilibrium properties of iron alloys and compounds at extreme pressure and temperature conditions (Jeanloz, 1990). I present measurements of the isothermal equation of state of the inter-metallic compound Fe_5Si_3, the mineral xifengite, and its high temperature stability at high pressures.

Planetary cooling is also broadly important for the long term evolution of the Earth's surface. Plate tectonics is the surface expression of a hot interior ($> 5000K$), driven out of equilibrium with a cold boundary condition ($300K$). Plate tectonics is responsible for forcing rock out of chemical equilibrium, where weathering creates sediment, leading to erosion and transport (Burbank and Anderson, 2011). The mass flux of sediment describes the process by which landscapes form and evolve over time. I present evidence for a non-linear mass flux law on hillslopes from a high resolution topography dataset on the South Island, New Zealand.

1.2 Earth's Heat

Earth can be thought of as a heat engine, which converts the loss of primordial and radiogenic heat into mechanical energy, driving mantle convection and plate tectonics, which recycle elements from the crust to the core-mantle boundary (Lay et al., 2008). The rate of heat loss from the core helps determine the power available to drive the geodynamo, which is responsible for Earth's long-lived intrinsic magnetic field (Stevenson et al., 1983). These planetary scale processes are related to the ability of the terrestrial minerals and metals to conduct heat (Manga and Jeanloz, 1997).

In order to link the structures observed by seismic tomography (French and Romanowicz, 2015) to the physical properties of the rocks present in Earths mantle, it is important to know the depth profile of thermal conductivity. The large low shear velocity provinces (LLSVP's; red colors in Fig. 1.1) in the lower mantle provide a snapshot of the heat and mass transfer that occurs over billions of years (McNamara and Zhong, 2005). Geochemical evidence shows that LLSVP's bring to the surface chemically primordial (e.g. unmixed) regions from the lowermost mantle (Jackson et al., 2017). Likewise, crustal material may descend as subducted slabs all the way to the core-mantle boundary, as evidenced by phase relations of oceanic lithosphere at high pressures and temperatures (Hirose et al., 1999). This planetary scale cycling of heat and mass has fundamental consequences for how and why Earth has plate tectonics and has maintained an atmosphere and oceans. Dynamical simulations of mantle convection have shown that the depth dependence of thermal conductivity can have profound effects on the structures that emerge in the mantle and the fate of subducted oceanic crust (Tosi et al., 2013). The depth profile of thermal conductivity in the

mantle requires in-situ measurements of mineral thermal conductivity at high pressure and temperature conditions.

The thermal conductivity of at the very base of the lower mantle, in the core-mantle boundary (CMB) region, plays a major role in the thermal evolution of Earth. The CMB is the thermal and chemical boundary layer that separates the solid silicates and oxides of Earth's mantle from the liquid, iron-rich fluid in Earth's outer core. Heat is transported by conduction in the CMB, according to boundary layer theory (Bejan, 2013). The flux of heat across the CMB is proportional to the temperature gradient, as given by Fourier's law, $q = -\kappa \nabla T$, where κ is the bulk thermal conductivity (Fig. 1.2). Uncertainty in the thermal gradient and material properties of the CMB result in a total heat flux between 4 TW to 20 TW (Kavner and Rainey, 2016). Between these bounds exist a remarkable set of planetary thermal histories. A high heat flux, significantly above 10 TW implies a young crystallization age ($< 1Ga$) of the inner core and requires exotic mechanisms, such as MgO crystallization, to maintain the magnetic field for most of Earth's history (Lay et al., 2008; Olson, 2016; ORourke and Stevenson, 2016). A low heat flux significantly less than 10 TW implies an older inner core, the crystallization of which has played a significant long-term role in producing the magnetic field.

The thermal conductivity of simple dielectric materials, such as minerals in Earth's mantle, can be described as the sum of lattice, electrical and radiative components (Klemens, 1969). In the upper mantle, the radiative and electrical components are negligible, and thermal conductivity is determined by the lattice component. At lower mantle conditions, the high temperatures may result in a significant contribution of radiative heat transport, which increases with temperature (Hofmeister, 1999), though there is considerable discrepancy in the magnitude of the radiative component to the total thermal conductivity (Keppler et al.,

2008; Goncharov et al., 2008; Rainey, 2014). In this dissertation, I focus measurements and on the lattice component of thermal conductivity.

The lattice component can be estimated by Debye theory,

$$\kappa_{lat} = C_v v l \tag{1.1}$$

where C_v is the constant volume heat capacity, v is the group velocity, and l is the mean free path (Klemens, 1969). For minerals in the mantle, acoustic phonons are the major carriers of heat, so that κ_{lat}can be approximated as the average sound speed (Roufosse and Klemens, 1973). At high pressures and temperatures, thermal conductivity can be quantified by extrapolating from ambient condition values using Liebfried-Schlomann (LS) theory (de Koker, 2010). Even without deriving LS theory, inspection of Eq. 1.1 reveals that the thermal conductivity should increase with pressure, because the speed of sound of dielectric materials increases with pressure. Conversely, as temperature is raised, the mean free path, l, decreases, so the thermal conductivity should decrease with increasing temperature (Roufosse and Klemens, 1974). The result for a single phase in the mantle is that the lattice thermal conductivity should moderately increase as pressure and temperature increase with depth in the Earth.

Measurements of lattice thermal conductivity at high pressures are of two types. Transient techniques use pump-probe pulsed laser heating to make time-resolved measurements, typically of thermo-reflectance, and calculate thermal diffusivity using the time-dependent heat equation (Kang et al., 2008; Ohta et al., 2012; Dalton et al., 2013). Thermal conductivity is calculated from the diffusivity measurements using the heat capacity and density of the material. Steady state techniques use continuous wave laser heating, make measurements

of temperature, and calculate thermal conductivity using steady-state heat flow modeling (Rainey and Kavner, 2014). The thermal conductivity of the mantle is determined by the conductivity of the minerals stable there. In a pyrolitic lower mantle, the minerals present are $(Mg, Fe)SiO_3$ bridgmanite (75%), $(Mg, Fe)O$ ferropericlase (20%) and Ca-perovskite (5%), where percentages are by volume (Mattern et al., 2005; Cottaar et al., 2014) . The high pressure thermal conductivity of $MgSiO_3$ bridgmanite has been measured at lower mantle pressures, but over a limited range of temperatures (Osako and Ito, 1991; Manthilake et al., 2011; Ohta et al., 2012). At room temperature, $MgSiO_3$ bridgmanite thermal conductivity increases with pressure dependence, $\frac{dlnk}{dln\rho} = 5.6$, increasing to 30 W/mK at 120 GPa (Ohta et al., 2012). Along a mantle temperature profile (e.g. Fig. 1.2), the thermal conductivity of $MgSiO_3$ bridgmanite increases from about 5 W/mK to 12 W/mK at core-mantle boundary conditions (Osako and Ito, 1991; Ohta et al., 2012).

The addition of iron to the structure reduces the thermal conductivity of brigmanite and may also reduce the pressure dependence (Manthilake et al., 2011; Rainey, 2014; Hsieh et al., 2017). The pressure dependence of thermal conductivity of Fe-bearing bridgmanite has been measured by the steady state method to be significantly lower than the pure-Mg bridgmanite, with $\frac{dlnk}{dln\rho} = 3.4$ (Rainey, 2014). A similar pressure dependence was obtained using ab initio calculations of Fe-bearing bridgmanite thermal conductivity (Tang and Dong, 2010).

The thermal conductivity of periclase (MgO) has been measured at high pressures and temperatures (Dalton et al., 2013; Rainey and Kavner, 2014; Manthilake et al., 2011). At ambient pressure conditions and 300 K, MgO thermal conductivity is 50 W/mK (Hofmeister, 2014). As pressure increases at constant temperature, the thermal conductivity increases,

with a pressure dependence $\frac{dlnk}{dln\rho} = 5.0$ (Dalton et al., 2013). Along a mantle temperature profile (e.g. Fig. 1.2), the thermal conductivity increases from 12 W/mK at the top of the lower mantle to about 20 W/mK at the core-mantle boundary, depending on the choice of CMB thermal gradient. MgO thermal conductivity has been extensively modeled using ab initio techniques, which are generally in agreement with experiments (de Koker, 2010; Stackhouse et al., 2010; Tang and Dong, 2010).

The addition of Fe into the structure of (Mg,Fe)O reduces the thermal conductivity significantly (Goncharov et al., 2015a; Ohta et al., 2017). Additionally, (Mg,Fe)O undergoes a spin transition between 40 and 60 GPa from high spin to low spin configuration of iron (Badro et al., 2003). The spin transition has been shown to reduce thermal diffusivity as a function of pressure, at constant temperature (Ohta et al., 2017). The range of pressures and temperatures over which measurements have been made of ferropericlase is shown in Figure 1.3.

Existing measurements of lattice thermal conductivity of the major mantle minerals indicate an increase of a factor of between 1.5 and 3 over the pressure range of the lower mantle. The discrepancy between measurements depends on how iron is accounted for and on the measurement technique. In general, though, thermal conductivity increases with depth in the lower mantle, based on existing measurements. However, phase transitions in the lower mantle have not been accounted for in depth profiles of thermal conductivity, and could introduce discontinuities in thermal conductivity with depth in the lower mantle.

High-pressure phase transitions in the lower mantle complicate modeling of thermal conductivity of the mantle. Ferropericlase undergoes a phase transition from high spin to low

spin, with a broad mixed spin state throughout most of the lower mantle (Badro et al., 2003; Tsuchiya et al., 2006; Holmström and Stixrude, 2015). It is therefore important to make *in-situ* measurements of thermal conductivity for bridgmanite and ferropericlase at the pressure and temperature conditions of the lower mantle. In Chapter 2, I develop a technique to measure thermal conductivity across a phase transition, using the method of Rainey and Kavner (2014) and the ionic salt NaCl as a test material. In Chapter 3, I apply this method to measure thermal conductivity from the high spin to mixed spin state of ferropericlase and show that thermal conductivity decreases significantly in the mixed spin state.

1.3 Earth's Core

The Earth's present-day core is divided into a liquid outer core and solid inner core. The composition of the core is uncertain, but it is known from seismic observations that the outer core is 8% less dense than pure liquid iron, and the inner core is about 5% less dense than pure solid iron (Jeanloz, 1990; Poirier, 1994) (see Figure 1.4). The density difference is consistent with the presence of light alloying elements, which are preferentially partitioned into the liquid as the inner-core freezes out. The identity of plausible light elements in the core depends on their pressure-temperature-density relationship (Campbell, 2016). The equilibrium phase diagrams at high pressure and temperature for iron alloys are also necessary to identify light element candidates (Fischer et al., 2013; Campbell, 2016). Silicon has long been considered a candidate for a major light element in the core due to its abundance in the bulk Earth the solubility of Si in solid Fe alloy at ambient conditions (Poirier, 1994; Lin et al., 2003; Kubaschewski, 2013). Geochemical and cosmochemical isotopic fractionation evidence suggests that a significant amount of Si (6 weight %) may be sequestered in the core (Georg et al., 2007). In Chapter 4, I report the isothermal equation of state of an

inter-metallic iron-silicon compound, Fe_5Si_3, the mineral xifengite. Additionally, I show that xifengite is not stable at high temperatures $> 1200K$, confirming previous work that there is a miscibility gap in the Fe-FeSi system at high pressures (Lin et al., 2009; Fischer et al., 2013).

1.4 Earth's Surface

Sediment mass flux on the surface of Earth is typically parameterized as the movement of particles due to forces exerted by a fluid, namely air or water (Anderson and Anderson, 2010). Sand grains are being transported in bedload or suspension in rivers and along shorelines, and by saltation under the effect of strong winds in desert and coastal environments. But for the majority of the terrestrial surface area of Earth, and other solar system bodies, sediments are transported by stochastic motion in a gravitational field (Tucker and Bradley, 2010). This process is broadly termed hillslope transport.

The transport of sediment on hillslopes is important for understanding the shape of the landscape, the flux of sediment over long timescales and for geo-engineering applications (Tucker and Bras, 1998). It has long been known, from observations in the field, that the shape of hillslopes is convex, and that this shape is broadly consistent with solutions to the diffusion equation (Culling, 1960, 1963, 1965). It has been inferred, then, that linear diffusion, analogous to the heat equation, explains the bulk transport of sediment grains over time, with a characteristic hillslope diffusivity, which may depend on variables such as sediment grain size and climate. However, though linear diffusion may describe hillslope transport in many cases, studies suggest that nonlinear transport laws may be more appropriate for steep landscapes (Roering et al., 1999; Heimsath et al., 2005; Tucker and Bradley, 2010). Non-linear transport laws are difficult to prove directly in part because of the lack of

combined datasets of high-resolution topography and geochronology. Using a LiDAR digital elevation dataset from New Zealand, in conjunction with unprecedented sampling density with luminescence-based age control, I show in Chapter 5 that a non-linear mass flux law is consistent with observations of degraded terrace risers ranging in height from 2m to 14m and in age from 4.2 ka to 7.5 ka.

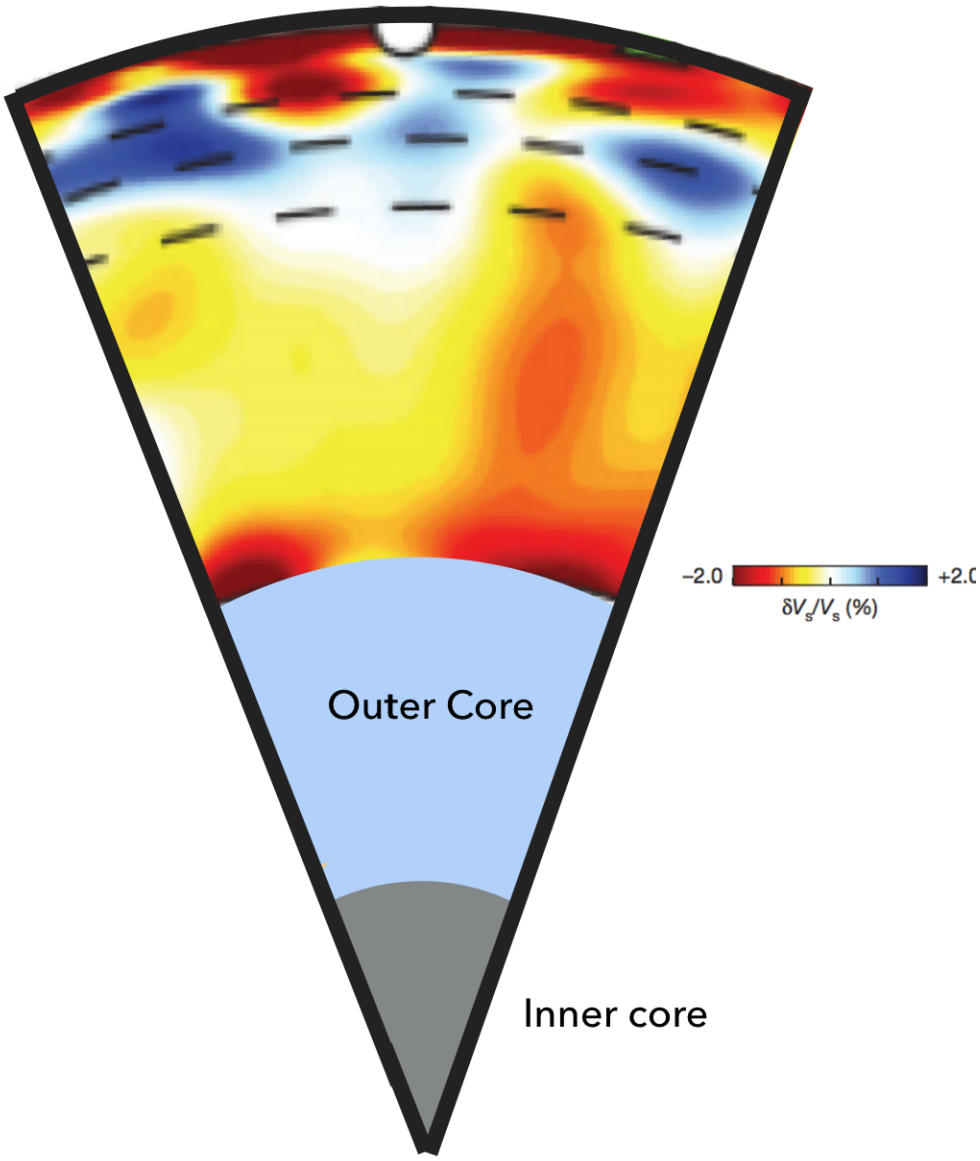

Figure 1.1: Seismic tomography inversion (Figure adapted from French and Romanowicz (2015)) provides evidence for global mantle structures extending from the core-mantle boundary to the upper mantle. 3D mantle structures of large low shear velocity provinces (LLSVPs) are interpreted from the large (red) reduced velocity region. Major phase transitions in the upper mantle are marked by the dotted lines.

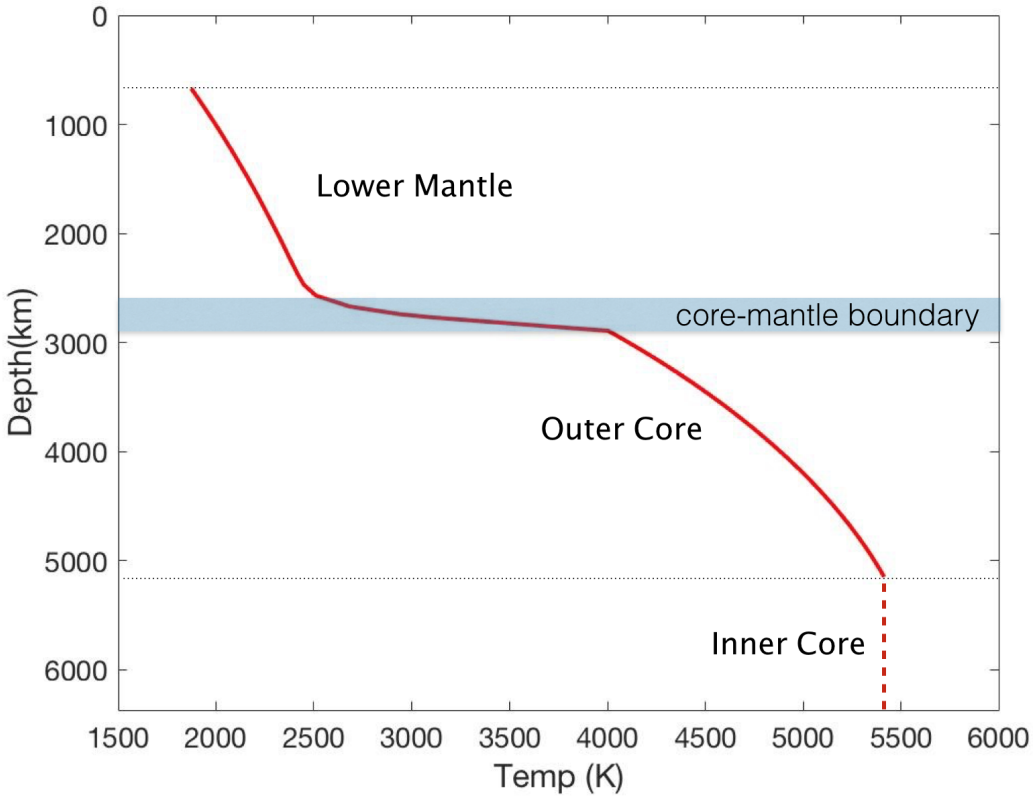

Figure 1.2: The temperature in the Earth from the lower mantle to the inner core boundary. The temperature gradient in the core-mantle (CMB) boundary region is determined by a conduction profile appended to the lower mantle temperature profile (Wolf et al., 2015) with a lower tie point at the temperature at the top of the outer core. The core temperature is determined by the melting temperature of iron at the inner-core boundary (Jackson et al., 2013).

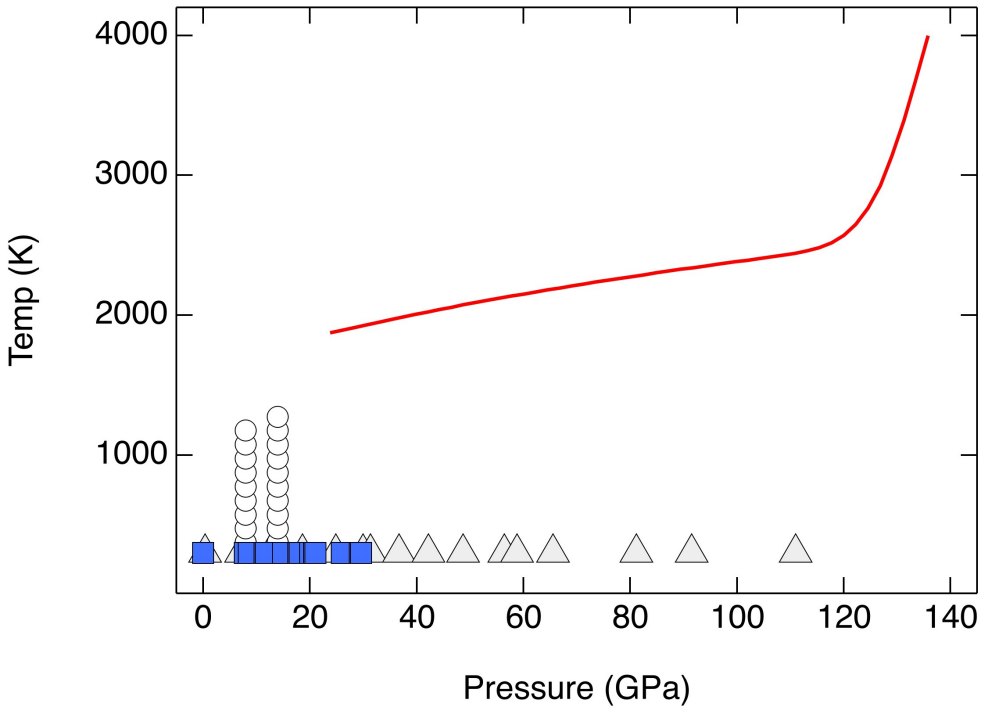

Figure 1.3: The pressure and temperature conditions of thermal conductivity measurements of iron-bearing ferropericlase are shown in the symbols. Ambient temperature measurements of (Ohta et al., 2017) are shown with upward triangles, and the blue squares are from (Goncharov et al., 2015b). High temperature measurements of (Manthilake et al., 2011) are shown in circles. A lower mantle geotherm is shown with the solid red line (Wolf et al., 2015).

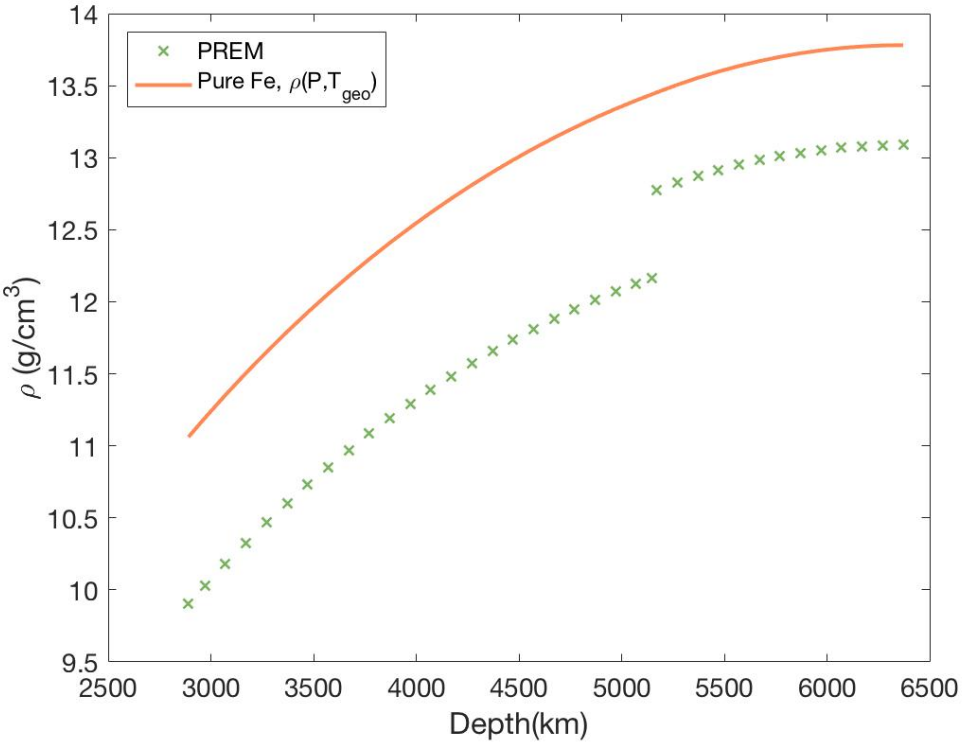

Figure 1.4: The density of the outer and inner core of Earth from the preliminary reference earth model (PREM) is shown in the green symbols. The density of solid, pure iron, along the core geotherm shown in Fig. 1.2 is shown as the solid orange line.

Bibliography

Ammann, M.W., Walker, A.M., Stackhouse, S., Wookey, J., Forte, A.M., Brodholt, J.P., Dobson, D.P., 2014. Variation of thermal conductivity and heat flux at the earth's core mantle boundary. Earth and Planetary Science Letters 390, 175–185.

Anderson, R.S., Anderson, S.P., 2010. Geomorphology: the mechanics and chemistry of landscapes. Cambridge University Press.

Badro, J., Fiquet, G., Guyot, F., Rueff, J.P., Struzhkin, V.V., Vankó, G., Monaco, G., 2003. Iron partitioning in earth's mantle: toward a deep lower mantle discontinuity. Science 300, 789–791.

Bejan, A., 2013. Convection heat transfer. John wiley & sons.

Buffett, B.A., 2002. Estimates of heat flow in the deep mantle based on the power requirements for the geodynamo. Geophysical Research Letters 29.

Burbank, D.W., Anderson, R.S., 2011. Tectonic geomorphology. John Wiley & Sons.

Campbell, A.J., 2016. Phase diagrams and thermodynamics of core materials. Deep Earth: Physics and Chemistry of the Lower Mantle and Core 217, 191.

Cottaar, S., Heister, T., Rose, I., Unterborn, C., 2014. Burnman: A lower mantle mineral physics toolkit. Geochemistry, Geophysics, Geosystems 15, 1164–1179.

Culling, W., 1960. Analytical theory of erosion. The Journal of Geology 68, 336–344.

Culling, W., 1963. Soil creep and the development of hillside slopes. The Journal of Geology 71, 127–161.

Culling, W., 1965. Theory of erosion on soil-covered slopes. The Journal of Geology 73, 230–254.

Dalton, D.A., Hsieh, W.P., Hohensee, G.T., Cahill, D.G., Goncharov, A.F., 2013. Effect of mass disorder on the lattice thermal conductivity of mgo periclase under pressure. Scientific reports 3, 2400.

Fischer, R.A., Campbell, A.J., Reaman, D.M., Miller, N.A., Heinz, D.L., Dera, P., Prakapenka, V.B., 2013. Phase relations in the fe–fesi system at high pressures and temperatures. Earth and Planetary Science Letters 373, 54–64.

French, S.W., Romanowicz, B., 2015. Broad plumes rooted at the base of the earth's mantle beneath major hotspots. Nature 525, 95.

Georg, R.B., Halliday, A.N., Schauble, E.A., Reynolds, B.C., 2007. Silicon in the earths core. Nature 447, 1102.

Goncharov, A.F., Haugen, B.D., Struzhkin, V.V., Beck, P., Jacobsen, S.D., 2008. Radiative conductivity in the earths lower mantle. Nature 456, 231.

Goncharov, A.F., Lobanov, S.S., Tan, X., Hohensee, G.T., Cahill, D.G., Lin, J.F., Thomas, S.M., Okuchi, T., Tomioka, N., 2015a. Experimental study of thermal conductivity at high pressures: Implications for the deep earths interior. Physics of the Earth and Planetary Interiors 247, 11–16.

Goncharov, A.F., Lobanov, S.S., Tan, X., Hohensee, G.T., Cahill, D.G., Lin, J.F., Thomas, S.M., Okuchi, T., Tomioka, N., 2015b. Experimental study of thermal conductivity at high pressures: Implications for the deep earths interior. Physics of the Earth and Planetary Interiors 247, 11–16.

Heimsath, A.M., Furbish, D.J., Dietrich, W.E., 2005. The illusion of diffusion: Field evidence for depth-dependent sediment transport. Geology 33, 949–952.

Hirose, K., Fei, Y., Ma, Y., Mao, H.K., 1999. The fate of subducted basaltic crust in the earth's lower mantle. Nature 397, 53.

Hofmeister, A., 1999. Mantle values of thermal conductivity and the geotherm from phonon lifetimes. Science 283, 1699–1706.

Hofmeister, A.M., 2014. Thermal diffusivity and thermal conductivity of single-crystal mgo and al 2 o 3 and related compounds as a function of temperature. Physics and Chemistry of Minerals 41, 361–371.

Holmström, E., Stixrude, L., 2015. Spin crossover in ferropericlase from first-principles molecular dynamics. Physical review letters 114, 117202.

Hsieh, W.P., Deschamps, F., Okuchi, T., Lin, J.F., 2017. Reduced lattice thermal conductivity of fe-bearing bridgmanite in earth's deep mantle. Journal of Geophysical Research: Solid Earth .

Jackson, J.M., Sturhahn, W., Lerche, M., Zhao, J., Toellner, T.S., Alp, E.E., Sinogeikin, S.V., Bass, J.D., Murphy, C.A., Wicks, J.K., 2013. Melting of compressed iron by monitoring atomic dynamics. Earth and Planetary Science Letters 362, 143–150.

Jackson, M., Konter, J., Becker, T., 2017. Primordial helium entrained by the hottest mantle plumes. Nature 542, 340.

Jeanloz, R., 1990. The nature of the earth's core. Annual Review of Earth and Planetary Sciences 18, 357–386.

Kang, K., Koh, Y.K., Chiritescu, C., Zheng, X., Cahill, D.G., 2008. Two-tint pump-probe measurements using a femtosecond laser oscillator and sharp-edged optical filters. Review of Scientific Instruments 79, 114901.

Karato, S.I., Murthy, V.R., 1997. Core formation and chemical equilibrium in the earthi. physical considerations. Physics of the Earth and Planetary Interiors 100, 61–79.

Kavner, A., Rainey, E.S., 2016. Heat transfer in the core and mantle. Deep Earth: Physics and Chemistry of the Lower Mantle and Core , 31–42.

Keppler, H., Dubrovinsky, L.S., Narygina, O., Kantor, I., 2008. Optical absorption and radiative thermal conductivity of silicate perovskite to 125 gigapascals. Science 322, 1529–1532.

Klemens, P., 1969. Thermal conductivity, vol. 1, edited by rp tye. Academic (New York, 1969) p 1.

Knittle, E., Jeanloz, R., 1989. Simulating the core-mantle boundary: An experimental study of high-pressure reactions between silicates and liquid iron. Geophysical Research Letters 16, 609–612.

de Koker, N., 2010. Thermal conductivity of mgo periclase at high pressure: implications for the d region. Earth and Planetary Science Letters 292, 392–398.

Kubaschewski, O., 2013. IronBinary phase diagrams. Springer Science & Business Media.

Lay, T., Hernlund, J., Buffett, B.A., 2008. Core–mantle boundary heat flow. Nature Geoscience 1, 25.

Lin, J.F., Scott, H.P., Fischer, R.A., Chang, Y.Y., Kantor, I., Prakapenka, V.B., 2009. Phase relations of fe-si alloy in earth's core. Geophysical Research Letters 36.

Lin, J.F., Struzhkin, V.V., Sturhahn, W., Huang, E., Zhao, J., Hu, M.Y., Alp, E.E., Mao, H.k., Boctor, N., Hemley, R.J., 2003. Sound velocities of iron-nickel and iron-silicon alloys at high pressures. Geophysical Research Letters 30.

Manga, M., Jeanloz, R., 1997. Thermal conductivity of corundum and periclase and implications for the lower mantle. Journal of Geophysical Research: Solid Earth 102, 2999–3008.

Manthilake, G.M., de Koker, N., Frost, D.J., McCammon, C.A., 2011. Lattice thermal conductivity of lower mantle minerals and heat flux from earths core. Proceedings of the National Academy of Sciences 108, 17901–17904.

Mattern, E., Matas, J., Ricard, Y., Bass, J., 2005. Lower mantle composition and temperature from mineral physics and thermodynamic modelling. Geophysical Journal International 160, 973–990.

McNamara, A.K., Zhong, S., 2005. Thermochemical structures beneath africa and the pacific ocean. Nature 437, 1136.

Ohta, K., Yagi, T., Hirose, K., Ohishi, Y., 2017. Thermal conductivity of ferropericlase in the earth's lower mantle. Earth and Planetary Science Letters 465, 29–37.

Ohta, K., Yagi, T., Taketoshi, N., Hirose, K., Komabayashi, T., Baba, T., Ohishi, Y., Hernlund, J., 2012. Lattice thermal conductivity of mgsio3 perovskite and post-perovskite at the core–mantle boundary. Earth and Planetary Science Letters 349, 109–115.

Olson, P., 2016. Mantle control of the geodynamo: Consequences of top-down regulation. Geochemistry, Geophysics, Geosystems 17, 1935–1956.

Osako, M., Ito, E., 1991. Thermal diffusivity of mgsio3 perovskite. Geophysical Research Letters 18, 239–242.

ORourke, J.G., Stevenson, D.J., 2016. Powering earths dynamo with magnesium precipitation from the core. Nature 529, 387.

Poirier, J.P., 1994. Light elements in the earth's outer core: a critical review. Physics of the earth and planetary interiors 85, 319–337.

Rainey, E., Kavner, A., 2014. Peak scaling method to measure temperatures in the laser-heated diamond anvil cell and application to the thermal conductivity of mgo. Journal of Geophysical Research: Solid Earth 119, 8154–8170.

Rainey, E.S.G., 2014. The Thermal Conductivity of the Earth's Lower Mantle and Implications for Heat Flow at the Core-Mantle Boundary. University of California, Los Angeles.

Roering, J.J., Kirchner, J.W., Dietrich, W.E., 1999. Evidence for nonlinear, diffusive sediment transport on hillslopes and implications for landscape morphology. Water Resources Research 35, 853–870.

Roufosse, M., Klemens, P., 1973. Thermal conductivity of complex dielectric crystals. Physical Review B 7, 5379.

Roufosse, M.C., Klemens, P., 1974. Lattice thermal conductivity of minerals at high temperatures. Journal of Geophysical Research 79, 703–705.

Stackhouse, S., Stixrude, L., Karki, B.B., 2010. Thermal conductivity of periclase (mgo) from first principles. Physical review letters 104, 208501.

Stevenson, D.J., Spohn, T., Schubert, G., 1983. Magnetism and thermal evolution of the terrestrial planets. Icarus 54, 466–489.

Stixrude, L., Wasserman, E., Cohen, R.E., 1997. Composition and temperature of earth's inner core. Journal of Geophysical Research: Solid Earth 102, 24729–24739.

Tang, X., Dong, J., 2010. Lattice thermal conductivity of mgo at conditions of earths interior. Proceedings of the National Academy of Sciences 107, 4539–4543.

Tosi, N., Yuen, D.A., de Koker, N., Wentzcovitch, R.M., 2013. Mantle dynamics with pressure-and temperature-dependent thermal expansivity and conductivity. Physics of the Earth and Planetary Interiors 217, 48–58.

Tsuchiya, T., Wentzcovitch, R.M., da Silva, C.R., de Gironcoli, S., 2006. Spin transition in magnesiowüstite in earths lower mantle. Physical Review Letters 96, 198501.

Tucker, G.E., Bradley, D.N., 2010. Trouble with diffusion: Reassessing hillslope erosion laws with a particle-based model. Journal of Geophysical Research: Earth Surface 115.

Tucker, G.E., Bras, R.L., 1998. Hillslope processes, drainage density, and landscape morphology. Water Resources Research 34, 2751–2764.

Wolf, A.S., Jackson, J.M., Dera, P., Prakapenka, V.B., 2015. The thermal equation of state of (mg, fe) sio3 bridgmanite (perovskite) and implications for lower mantle structures. Journal of Geophysical Research: Solid Earth 120, 7460–7489.

CHAPTER 2

Measurements of NaCl Thermal Conductivity Across the B1-B2 Phase Transition

2.1 Introduction

The pressure dependence of transport properties is of interest for design of electronic materials under strain and for deep Earth geophysics (Lyeo et al., 2006; Lay et al., 2008; Li et al., 2010). For dielectric materials, theoretical work based on Liebfried-Schlomann (LS) theory predicts an increase in the lattice thermal conductivity with pressure (Roufosse and Klemens, 1973; de Koker, 2010). These predictions are in good agreement with experimental results (Chen et al., 2011). A pressure-induced phase transition, however, can introduce discontinuities in transport properties of solids, including thermal conductivity (Roufosse and Jeanloz, 1983). In Earth's solid, rocky mantle, high pressure (> 25 GPa) structural and electronic phase changes may significantly affect the transport of heat in the interior of terrestrial planets (Ohta et al., 2012, 2017).

KCl and NaCl ionic salts undergo a structural phase transition from face-centered cubic (B1) to body-centered cubic (B2) at 1.9 GPa and 27 GPa respectively (Li and Jeanloz, 1987; Walker et al., 2002). The thermal conductivity of ionic salts across the B1-B2 phase transition has been explored experimentally and theoretically (Roufosse and Jeanloz, 1983; Andersson, 1985; Slack and Ross, 1985). For salts that undergo the B1-B2 transition at

pressures below 5 GPa, the thermal conductivity has been measured for both phases and can be described by LS theory (Andersson, 1985; Slack and Ross, 1985).

However, at such small compression, it is difficult to test the efficacy of LS theory to describe the experiments (Chen et al., 2011). The B1-B2 phase transition for NaCl occurs at 27 GPa (Li and Jeanloz, 1987), and the thermal conductivity has not previously been measured across the phase boundary for this material. Existing measurements of bulk thermodynamic properties of NaCl (Decker, 1971; Whitfield et al., 1976; Prencipe et al., 1995; Brown, 1999), allows the description of thermal conductivity using LS theory and can be compared with measurements in the diamond anvil cell (DAC).

2.2 Experiments

Here we measure the lattice thermal conductivity of ionic salts KCl and NaCl at extreme conditions of pressure and temperature in the DAC. Our approach combines experimental laser-heated DAC methods with a 3-D numerical heat flow model of the sample and cell components to interpret the measurements (Rainey et al., 2013). In the experiment, a sample consisting of a salt medium surrounding a transition metal infrared laser-absorber is loaded into a gasketted sample chamber in the DAC. The sample is heated from one side using an infrared laser. The sample temperature is measured as a function of laser power yielding a series of temperature - laser power curves (Fig. 2.1a,b). The heat flow model delineates the relationship between input laser power and temperature for a given sample configuration and set of material properties (Fig. 2.1c,d).

A series of measurements of temperature as a function of laser power were performed at the ALS 12.2.2 beamline. Experiments were performed on multiple materials (KCl and NaCl) and at several pressure steps. A thin ($5 - 10\mu m$) Fe metal absorber, surrounded by either KCl or NaCl salt pressure media, was loaded in a diamond cell equipped with

$300\mu m$ culets, within a $100\mu m$ hole drilled in a pre-compressed spring-steel gasket. For each sample loading, the initial gasket thickness was measured using a micrometer. Pressure was calibrated using ruby fluorescence (Mao et al., 1986) with a small piece of ruby placed on the diamond culet opposite from the heating side. The crystal structure of the salt layer was determined at each pressure step *in-situ* by x-ray diffraction (Brown, 1999; Walker et al., 2002; Dorogokupets and Dewaele, 2007). High temperatures were generated using variable power from a 100 W fiber-based laser source operating at $1.07\mu m$. The temperature was measured using spectroradiometry techniques that obtain an average temperature for the entire hotspot, combined with a two-dimensional map of the hotspot intensity radial profile (Kavner and Nugent, 2008; Rainey and Kavner, 2014).

At each pressure step, the laser power was increased in 0.5 W steps. The threshold laser power for coupling was noted, and then increased by steps of 0.5 W. At each laser power, 2-5 separate temperature measurements were obtained. In all cases, as laser power was increased, a threshold occurred where additional laser power no longer resulted in a temperature increase. After the threshold was released, the temperature-laser power relationship showed significant hysteresis. This threshold is observed in most experiments and for a broad variety of materials, including metals, salts, oxides, silicates, and fluid noble gas environments. However, its origin is uncertain, though it can be modeled by assuming a linear relation between power and absorber reflectivity (Geballe and Jeanloz, 2012). Therefore, in all cases, we analyze only the points on the increasing temperature-laser power curve, where a plateau is defined as two or more sequential points of constant or decreasing temperature with increasing laser power. Following a heating cycle, the pressure in the cell was increased, and an additional temperature-laser power curve was measured, using the same protocol.

2.3 Results

Temperature-laser power (T-LP) curves were measured for KCl medium surrounding an Fe foil (Fig. 2.1 b) and show the curves shifted to the right, indicating progressively lower temperatures for a given laser power as pressure increases. Figure 2.2 shows T-LP curves of KCl between 15 GPa and 24 GPa, with the temperature plateau data not plotted for clarity. Between 15 GPa and 19 GPa, the T-LP curves shift to the right and the temperature decreases by 260 K . Between 19 and 24 GPa, the temperature decreases by 190 K (Fig. 2.2).

An additional experiment on B2 KCl was carried out using stainless steel (316L) foil as a laser absorber, instead of iron. The T-LP curves over the pressure range 5.6 GPa to 22 GPa is shown in Figure 2.3. The temperature decreases by 310 K between 5.6 and 13.2 GPa and by 430 K between 13.2 and 22 GPa. For comparison, the Fe absorber temperature decreases by 457 K between 15 GPa and 24 GPa. These results are consistent, for both laser absorbers, and for different diamond anvil cell loadings.

Results for an Fe foil surrounded by NaCl (Fig. 2.4) show a more complicated pattern with pressure increase. The measured T-LP curve shifts to the right and decreases by 160 K between 14 and 18.6 GPa. But between 18.6 and 29.2 GPa, the measured T curve shifts to the left and increases by 475 K. The sign of temperature shift changes again between 29.2 and 43.2 GPa, where the curve shifts to the right and decreases by 280 K.

2.4 Heat flow model

The finite element heat flow model calculates the relationship between laser power and measured temperature. The sample and cell assembly geometry, absorption properties, and thermal conductivity and its temperature dependence are explicitly parameterized. The heat

flow model solves the steady state heat equation:

$$\nabla \cdot \kappa(T) \nabla T + H = 0 \tag{2.1}$$

Details of the numerical model and applications to measuring thermal conductivity of MgO are in (Rainey and Kavner, 2014). We assume the metal foil is opaque so that heating (H in Eq. 2.1) occurs by laser coupling at the surface of the foil only.

The thinning of the materials in the cell, including the gasket, sample and metal foil, can affect the peak temperature measured. Figure 2.1d shows the temperature versus laser power output of a set of heat flow model runs describing a hypothetical sample undergoing pressure-induced changes in geometry and thermal conductivity. For a given sample geometry and thickness, an increase in thermal conductivity of 10% causes the temperature at a given power to decrease by 200 K. When thinning (5% reduction in thickness) due to deformation of the gasket is included in addition to thermal conductivity increase (Fig. 2.1d), the temperature decreases by a further 50 K.

2.4.1 Radiative heat transport

Heat transport in dielectric materials at high temperatures requires consideration of radiative as well as conductive heat transport, but in the DAC, the length scale of the sample and the temperature gradient in the cell limits radiative transport to a negligible value (Manga and Jeanloz, 1997). Radiative heat flux can be approximated as:

$$Q_{rad} = n^2 \epsilon \sigma T^4 \tag{2.2}$$

where n is the index of refraction, set to 1.5, ϵ is the emissivity, approximated as a blackbody ($\epsilon = 1$), and σ is the Stephan-Boltzmann constant. The conductive heat flux is simply:

$$Q_{cond} = -\kappa \nabla T \tag{2.3}$$

where κ is the thermal conductivity. In a cell with a $10\mu m$ layer dielectric material, with $\kappa = 10\ W/mK$, and at our maximum temperatures of 2500 K, where radiative transport of heat would be highest, $Q_{rad} = 4.98 * 10^6\ W/m^2$ and $Q_{cond} = 2.22 * 10^9\ W/m^2$, meaning that radiative transport is, at most, 0.23% of total heat transport in our experiments. This calculation demonstrates the validity of considering only the lattice component of thermal conductivity in our heat flow model of the DAC.

2.4.2 Thermal conductivity temperature dependence

The thermal conductivity of materials in our experiments is strongly temperature dependent, and since our measurements are at simultaneous high pressure and temperature, a temperature dependence for each material must be assigned in the heat flow model. The thermal conductivity of each material is referenced to an ambient temperature value and assumed to follow a $\frac{T_0}{T}^m$ functional form at elevated temperature (de Koker, 2010). In the simplest case, m =1, and the thermal conductivity follows a 1/T form. This assumption is based on semi-classical anharmonic three-phonon scattering being responsible for thermal resistance (Roufosse and Klemens, 1974). However, high-temperature, ambient-pressure thermal conductivity data for NaCl fits a $\left(T_0/T\right)^m$ power law, with $m = 1.2$ (Birch and Clark, 1940; Kleiner et al., 2017). The thermal conductivity of solid NaCl decreases faster than predicted by the simplest model. This can be seen in Figure 2.5.

A possible explanation for this behavior is the the non-trivial interaction of optical phonons with acoustic phonons, which has been shown to be present for NaCl (Tiwari, 1978). Another possible explanation is that higher order scattering contributes significantly to thermal conductivity at high temperature (Feng et al., 2017). At constant pressure, (i.e. at each pressure step), we use $(\kappa)_P = \kappa_0\left(\frac{T_{ref}}{T}\right)^m$, where m = 1.2 is fit to NaCl data. As a check, the use of m = 1.2 does not reduce the crystalline thermal conductivity below the

measured liquid thermal conductivity (Nagasaka et al., 1992), as shown in Figure 2.5.

Another assumption implied by this temperature model is that the thermal conductivity continues to decrease with temperatures above 1200 K. This assumption should be valid until the phonon mean-free path approaches the inter-atomic spacing of the material, at which point the perturbational method used to derive the T_0/T thermal conductivity dependence is no longer valid (Roufosse and Klemens, 1974; de Koker, 2010). This condition likely occurs at high enough temperature for most dielectric materials that the functional form of thermal conductivity does not saturate over the experimental temperatures reported here (Roufosse and Klemens, 1974).

2.5 Heat flow modeling results

To interpret the experimental results in terms of pressure-induced changes in sample thermal conductivity, we ran a series of numerical models representing each experiment. For a set of measurements on a single sample as a function of pressure, the first and lowest-pressure T-LP curve is used to tune the laser power input in the numerical model required to reproduce the observed temperature versus power relationship. Then the numerical models are rerun using the calibrated laser powers, incorporating calculations of the pressure-dependent changes in sample thickness. The model is run iteratively, changing sample thermal conductivity using Newton's method of optimization until the modeled changes in temperature as a function of laser power reproduce the observed offsets (quantified as ΔT) in the T-LP curve.

Note that because we use the first T-LP curve in a set of measurements to tune the laser power in the numerical code, this means that we do not make a measurement of an absolute value of thermal conductivity. However, the measurement of the pressure dependence of thermal conductivity is robust (Rainey and Kavner, 2014). The numerical calculations require an assumed set of physical properties of the metallic laser absorber, including the

pressure and temperature dependence of its thermal conductivity. The starting values used in the numerical calculations are shown in Table 2.1. The absolute value for the thermal conductivity of iron at these pressure conditions is uncertain, but estimates range between 50 and 70 W/m/K (Deng et al., 2013; Seagle et al., 2013; Konôpková et al., 2016). On the other hand, fairly good agreement exists on the value of $\frac{dlnk}{dln\rho}$ (Seagle et al., 2013; Konôpková et al., 2016; Ohta et al., 2016). For our models, the initial thermal conductivity of hcp iron at 14 GPa and 300 K is approximated as 60 W/mK and the thermal conductivity is increased to the experimental pressure according to the average pressure slope of $1\% GPa^{-1}$ for iron.

The results of heat flow modeling are reported as relative values, normalized to a reference thermal conductivity and density, where ($g \equiv \frac{dln\kappa}{dln\rho}$). This form is convenient for analysis because g describes the density dependent exponential increase of thermal conductivity in LS theory. For KCl, from 14 to 24 GPa, with iron laser absorber, the heat flow model and temperature data require that $\frac{dlnk}{dln\rho} = 3.9$.

The results for NaCl give $\frac{dlnk}{dln\rho} = 1.8$, in the B1 phase, and $\frac{dlnk}{dln\rho} = 2.2$. The thermal conductivity increases with increasing density (or pressure) as expected. But across the B1-B2 phase boundary, from 19 GPa to 29 GPa, the thermal conductivity decreases. The temperature measurements require a reduction of 37% over this pressure range, or $\frac{dlnk}{dln\rho} = -9.4$. This result is consistent with other ionic salts, such as KCl, for which thermal conductivity has previously been observed to decrease across the B1-B2 phase transition.

2.6 Discussion

LS theory predicts the lattice thermal conductivity of a dielectric material will increase with density corresponding with (de Koker, 2010):

$$\kappa = \kappa_0 \left(\frac{\rho}{\rho_0}\right)^g \left(\frac{T_0}{T}\right)^m \tag{2.4}$$

where $g = 3\gamma + 2q - 1/3$. The thermo-elastic properties of KCl, including the equation of state of KCl and volume-dependent values for the Gruneisen parameter, $\gamma = 1.48$, and its pressure derivative, $q = 1.04$, (Decker, 1971; Walker et al., 2002) are used to inform Eq. 2.4 (Table 2.2).

Figure 2.7 shows the calculated pressure dependent changes in thermal conductivity required to explain the observed ΔT data for B2 KCl up to 24 GPa. Also shown in Figure 2.7, is independent data for the thermal conductivity of B1 and B2 KCl (Andersson, 1985). The low pressure data (Andersson, 1985) and our higher pressure results agree very well, with LS theory for B1 and B2 KCl.

The thermo-elastic properties of NaCl ($\gamma = 1.5$, $q = 1.4$) (Brown, 1999) are likewise used with Eq. 2.4 (Table 2.2). Following measurements and analysis from (Dorogokupets and Dewaele, 2007), the values for γ and q are constant across the B1-B2 phase transition (Table 2.2). Plots of Eq. 2.2 calculated for NaCl are shown as solid lines in Fig. 2.8. Our measured B1 phase $g \equiv \frac{dlnk}{dln\rho} = 1.8$ is less than half the slope calculated by LS theory ($g = 4.0$) while the measured $g = 2.2$ is about $\frac{1}{3}$ lower than the B2 phase calculated slope. The value of g, which is extrapolated from ambient pressure using the thermal equation of state, could be lowered from the theoretical value of 4.0 to 1.8 to match our observations of NaCl thermal conductivity in the B1 phase from 14 to 18.6 GPa. Alternatively, additional scattering mechanisms could be important in NaCl, as indicated by the ambient pressure, high-temperature thermal conductivity data (Birch and Clark, 1940; Feng et al., 2017; Kleiner et al., 2017). Additional scattering processes are not accounted for by LS theory and may contribute to the pressure dependence of thermal conductivity.

The implications of our assumptions about material properties can be explored using the heat flow model. We set up a series of runs in which we change the temperature dependence of thermal conductivity. Here we demonstrate the sensitivity of our results to changes in

our model assumptions. We use four cases, varying properties and methods, labeled S1 – S4, and shown in 2.3. In Case S1, NaCl has a temperature dependence of T^{-1} instead of $T^{-1.2}$. In Case S2, the laser power calibration curve is changed to the first T-LP curve in the B2 phase (i.e. the P = 29 GPa curve). In Case S3, we consider that the iron thermal conductivity does not change with pressure, and is fixed at a constant value of 60 W/mK. In Case S4, we consider that the iron thermal conductivity and the gasket thickness remain fixed to the 14 GPa values (60 W/mK and 36.48μm). The results of these cases are shown in Figure 2.9 The largest change occurs for considering that iron thermal conductivity does not change with pressure which causes the reduction in thermal conductivity across the B1/B2 transition to become smaller (37% reduction and 31% reduction, for pressure dependent and constant iron thermal conductivity, respectively).

We conclude that over the pressure range of the B1-B2 phase transition, a description of thermal conductivity using the assumptions of Liebfried & Schlomann and the Gruneisen parameter volume dependence can, in general, explain the thermal conductivity pressure dependence of salts in the B1 and B2 phase, though for NaCl, a more detailed treatment may be necessary. The experimental methods developed and described here have been shown to measure the pressure dependence of thermal conductivity in a single phase and measure the decrease in thermal conductivity across the B1-B2 phase transition of NaCl.

P (GPa)	τ_{tot} (μm)	τ_{Fe} (μm)	$\kappa_0^{Fe}(Wm^{-1}K^{-1})$
14	36.48	9.86	60
19	36.19	9.782	63
29	35.7	9.649	69
43	35.16	9.502	78

Table 2.1: Starting values for heat flow model

Material	$V_0(cm^3mol^{-1})$	$K_0(GPa)$	K_0'	γ	q	$\theta_D(K)$
NaCl B1	27.015	23.74	5.32	1.5	1.4	270
NaCl B2	24.53	29.72	5.4	1.5	1.4	270
KCl B1	37.57	17.1	5.32	1.48	1.04	236
KCl B2	32.25	17.2	5.89	1.48	1.04	236

Table 2.2: Thermal equation of state parameters for NaCl and KCl

Case	Calib. Press.	m	K_0^{Fe}	τ_{gasket}
Init.	P2	1.2	$\kappa_0^{Fe}(P)$	$\tau(P)$
S1	P2	1.0	$\kappa_0^{Fe}(P)$	$\tau(P)$
S2	P3	1.0	$\kappa_0^{Fe}(P)$	$\tau(P)$
S3	P2	1.0	κ_0^{Fe} fixed	$\tau(P)$
S4	P2	1.0	κ_0^{Fe} fixed	τ fixed

Table 2.3: Sensitivity test values for heat flow model

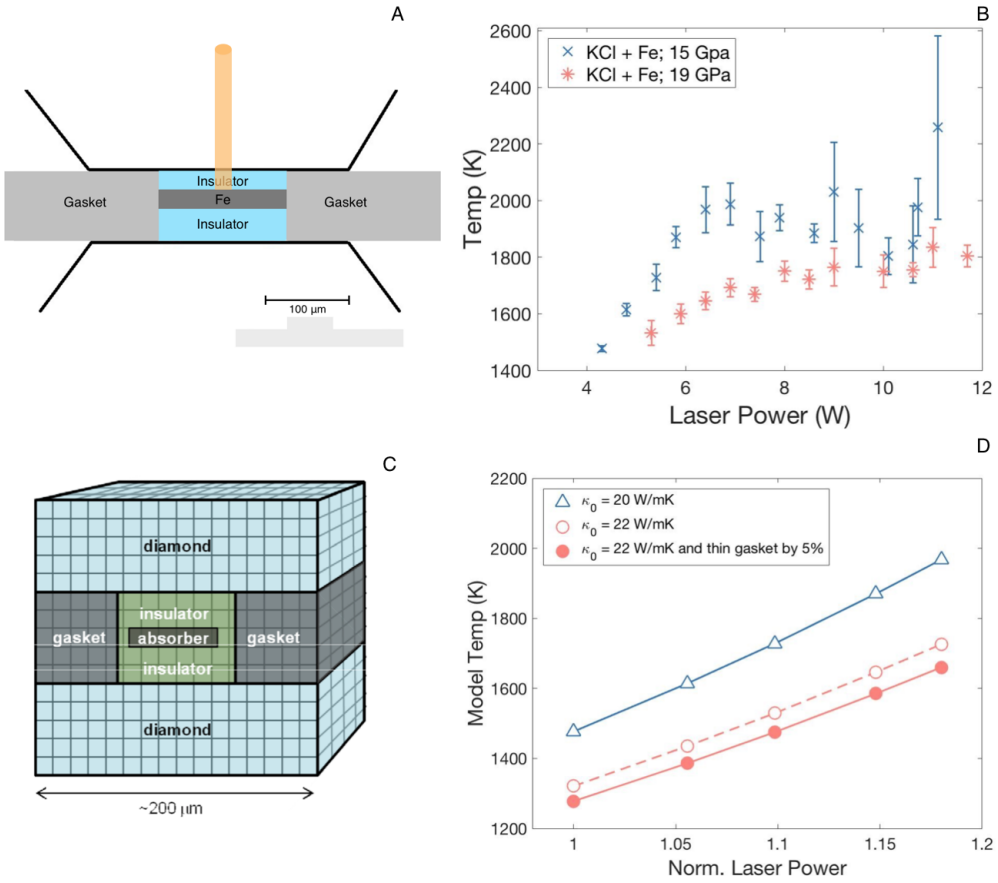

Figure 2.1: (a) Schematic of the sample geometry. An IR laser heats a metal foil surrounded by a salt insulating medium (either NaCl or KCl), loaded in a diamond anvil cell. (b) a typical series of temperature measurements as a function of laser power, shown at two different pressures. (c) A schematic of the geometry for the numerical heat flow code. (d) Calculated temperature as a function of laser power for a series of numerical models with changing thermal conductivity and thickness of insulation layer.

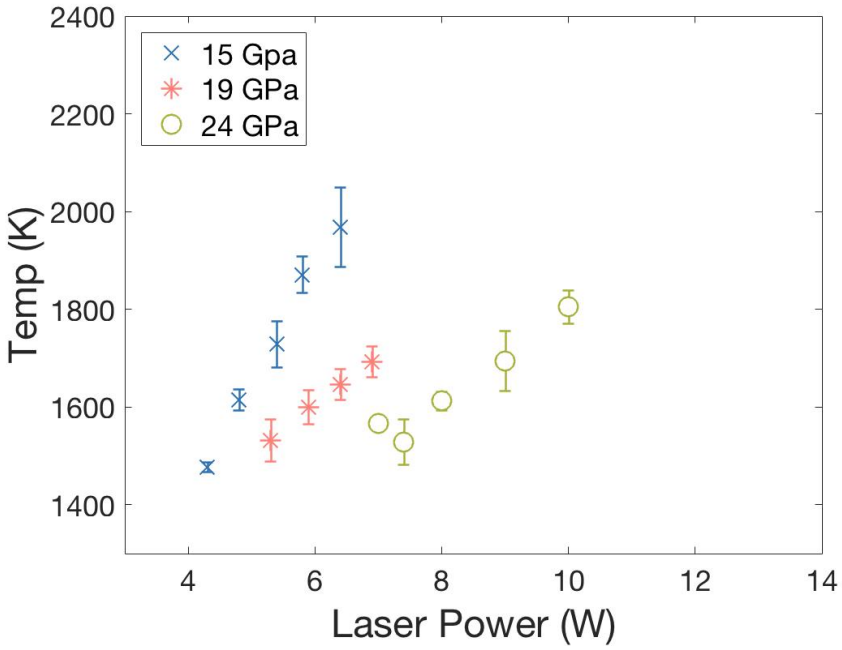

Figure 2.2: Measured temperature versus laser power is shown for KCl with Fe absorber from 15 Gpa to 24 GPa.

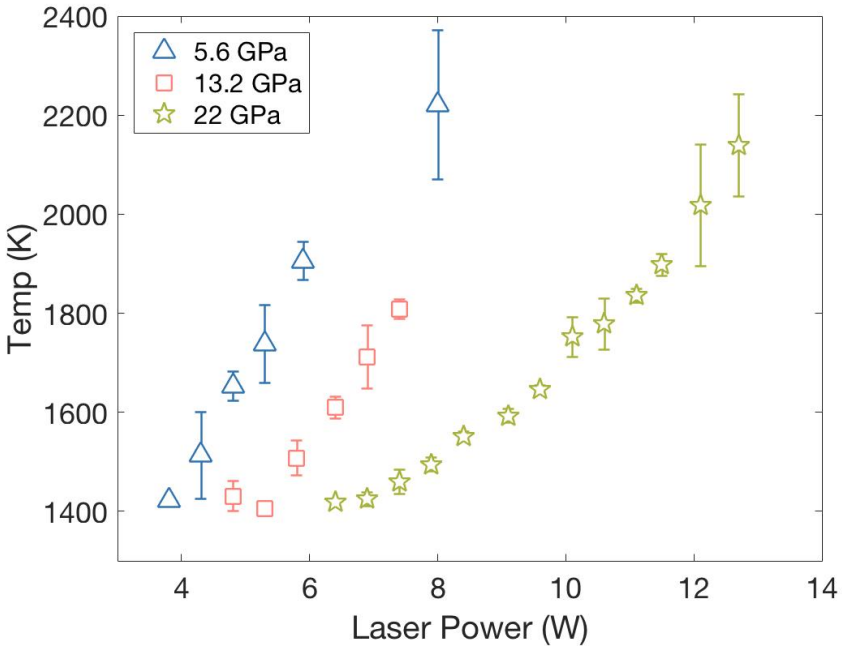

Figure 2.3: Measured temperature versus laser power is shown for KCl with stainless steel absorber from 5.6 Gpa to 22 GPa.

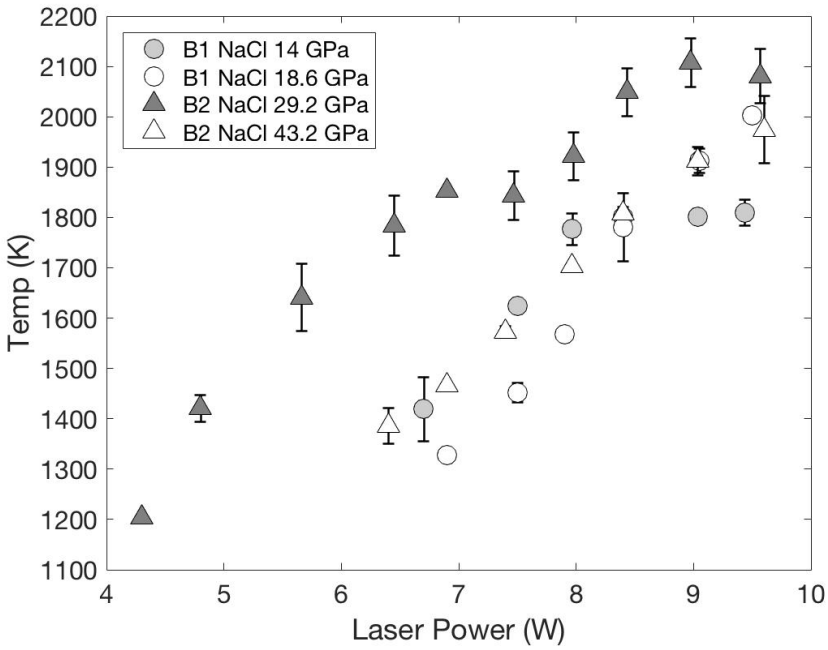

Figure 2.4: Measured temperature versus laser power is shown for NaCl from 14 GPa to 43 GPa. Circles and squares indicate the B1 and B2 phases, respectively.

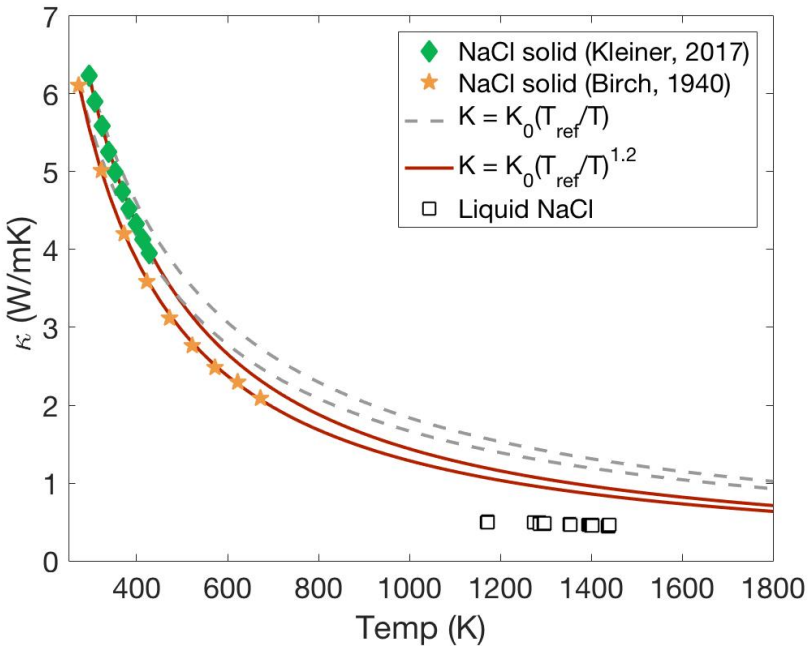

Figure 2.5: Comparison of the temperature dependence of thermal conductivity of NaCl with the T^{-1} dependence and $T^{-1.2}$ dependence.

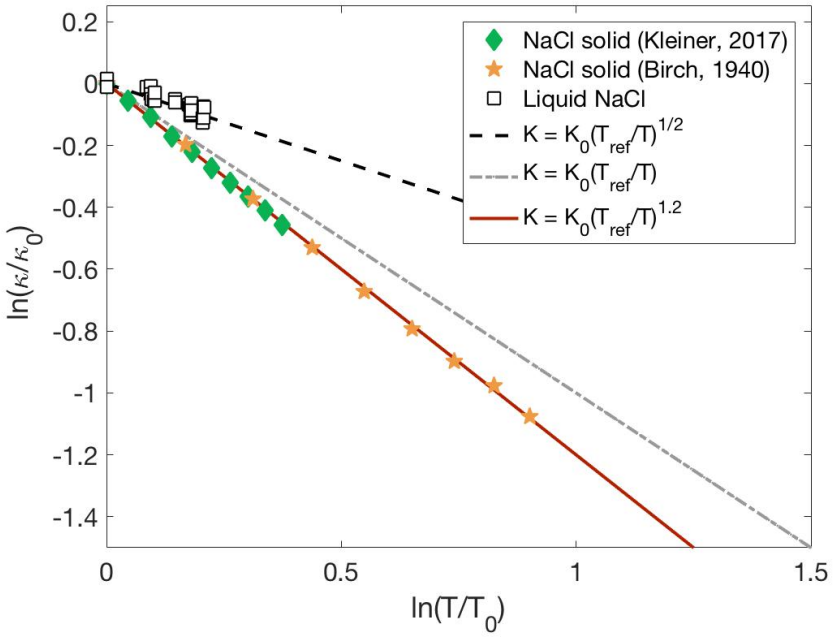

Figure 2.6: The logarithmic derivative of thermal conductivity as a function of temperature at ambient pressure shows that $\left(\frac{T_{ref}}{T}\right)^m$, where m = 1.2. Also shown is liquid NaCl, which follows m = 0.5. The liquid NaCl κ_0 is defined at the first liquid data point ($K = 0.497 W/mK$) at $1170K$.

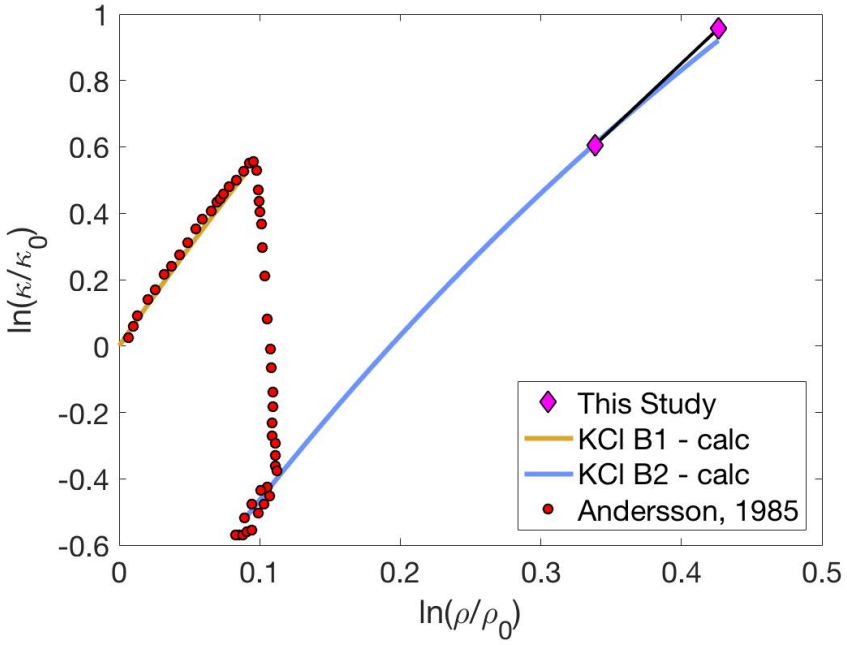

Figure 2.7: Normalized density dependence of of log thermal conductivity of KCl up to 24 GPa with the $\frac{dlnk}{dln\rho}$ results required by our temperature data, plotted with LS calculation using thermo-elastic parameters for KCl from Walker et al. (2002) and Decker (1971).

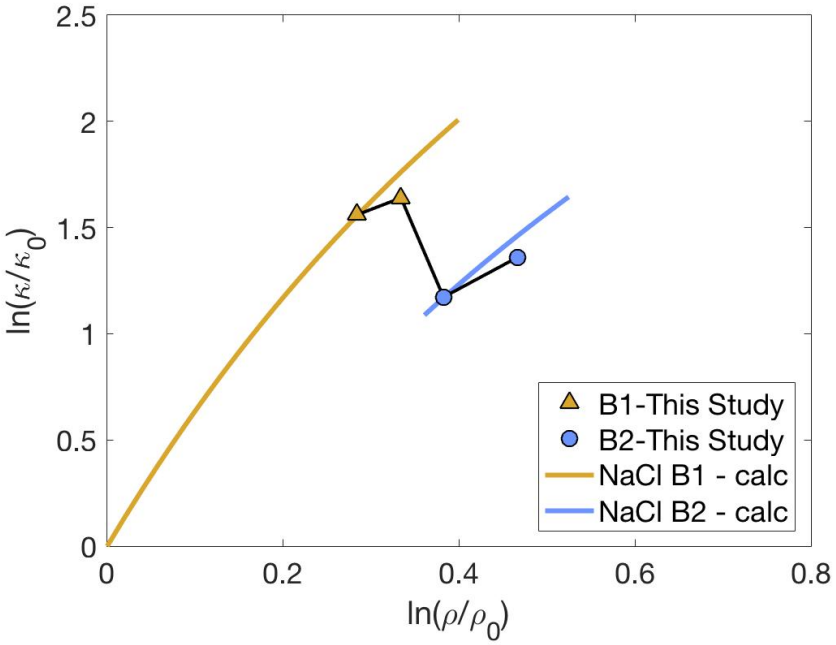

Figure 2.8: Measurements and models of thermal conductivity as a function of pressure for NaCl across the B1-B2 phase transition. The solid orange and blue lines show calculated NaCl thermal conductivity for B1 and B2 phases, respectively, according to LS theory.

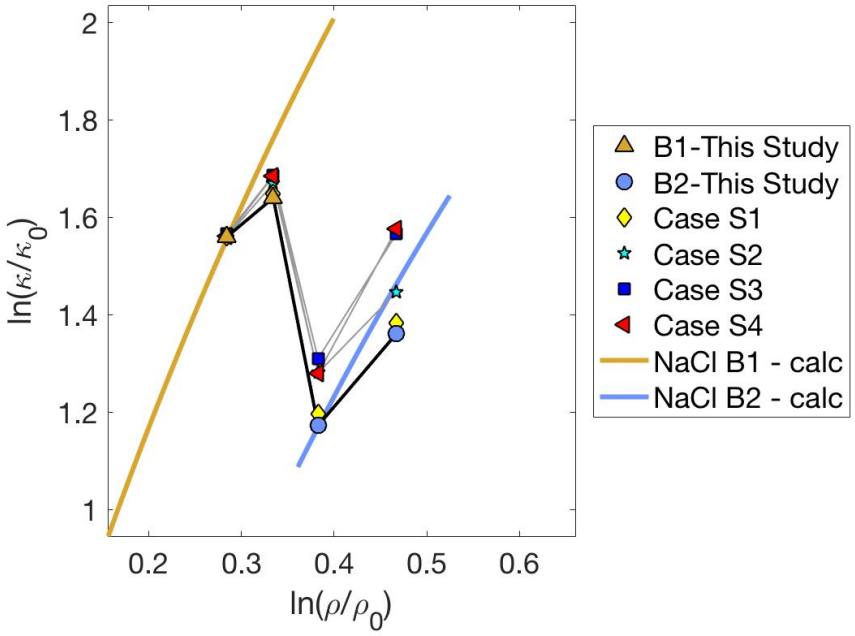

Figure 2.9: Log thermal conductivity, normalized to the ambient pressure and temperature is plotted against log normalized density with the results for each case, along with the initial case assumed in the text.

Bibliography

Andersson, P., 1985. Thermal conductivity under pressure and through phase transitions in solid alkali halides. i. experimental results for kcl, kbr, ki, rbcl, rbbr and rbi. Journal of Physics C: Solid State Physics 18, 3943.

Birch, F., Clark, H., 1940. The thermal conductivity of rocks and its dependence upon temperature and composition; part ii. American journal of Science 238, 613–635.

Brown, J.M., 1999. The nacl pressure standard. Journal of Applied Physics 86, 5801–5808.

Chen, B., Hsieh, W.P., Cahill, D.G., Trinkle, D.R., Li, J., 2011. Thermal conductivity of compressed h 2 o to 22 gpa: A test of the leibfried-schlömann equation. Physical Review B 83, 132301.

Decker, D.L., 1971. High-pressure equation of state for nacl, kcl, and cscl. Journal of Applied Physics 42, 3239–3244.

Deng, L., Seagle, C., Fei, Y., Shahar, A., 2013. High pressure and temperature electrical resistivity of iron and implications for planetary cores. Geophysical Research Letters 40, 33–37.

Dorogokupets, P., Dewaele, A., 2007. Equations of state of mgo, au, pt, nacl-b1, and nacl-b2: Internally consistent high-temperature pressure scales. High Pressure Research 27, 431–446.

Feng, T., Lindsay, L., Ruan, X., 2017. Four-phonon scattering significantly reduces intrinsic thermal conductivity of solids. Physical Review B 96, 161201.

Geballe, Z.M., Jeanloz, R., 2012. Origin of temperature plateaus in laser-heated diamond anvil cell experiments. Journal of applied physics 111, 123518.

Kavner, A., Nugent, C., 2008. Precise measurements of radial temperature gradients in the laser-heated diamond anvil cell. Review of Scientific Instruments 79, 024902.

Kleiner, F., Posern, K., Osburg, A., 2017. Thermal conductivity of selected salt hydrates for thermochemical solar heat storage applications measured by the light flash method. Applied Thermal Engineering 113, 1189–1193.

de Koker, N., 2010. Thermal conductivity of mgo periclase at high pressure: implications for the d region. Earth and Planetary Science Letters 292, 392–398.

Konôpková, Z., McWilliams, R.S., Gómez-Pérez, N., Goncharov, A.F., 2016. Direct measurement of thermal conductivity in solid iron at planetary core conditions. Nature 534, 99.

Lay, T., Hernlund, J., Buffett, B.A., 2008. Core–mantle boundary heat flow. Nature Geoscience 1, 25.

Li, X., Jeanloz, R., 1987. Measurement of the b1-b2 transition pressure in nacl at high temperatures. Physical Review B 36, 474.

Li, X., Maute, K., Dunn, M.L., Yang, R., 2010. Strain effects on the thermal conductivity of nanostructures. Physical Review B 81, 245318.

Lyeo, H.K., Cahill, D.G., Lee, B.S., Abelson, J.R., Kwon, M.H., Kim, K.B., Bishop, S.G., Cheong, B.k., 2006. Thermal conductivity of phase-change material ge 2 sb 2 te 5. Applied Physics Letters 89, 151904.

Manga, M., Jeanloz, R., 1997. Thermal conductivity of corundum and periclase and implications for the lower mantle. Journal of Geophysical Research: Solid Earth 102, 2999–3008.

Mao, H., Xu, J.A., Bell, P., 1986. Calibration of the ruby pressure gauge to 800 kbar under quasi-hydrostatic conditions. Journal of Geophysical Research: Solid Earth 91, 4673–4676.

Nagasaka, Y., Nakazawa, N., Nagashima, A., 1992. Experimental determination of the thermal diffusivity of molten alkali halides by the forced rayleigh scattering method. i. molten licl, nacl, kcl, rbcl, and cscl. International Journal of Thermophysics 13, 555–574.

Ohta, K., Kuwayama, Y., Hirose, K., Shimizu, K., Ohishi, Y., 2016. Experimental determination of the electrical resistivity of iron at earths core conditions. Nature 534, 95.

Ohta, K., Yagi, T., Hirose, K., Ohishi, Y., 2017. Thermal conductivity of ferropericlase in the earth's lower mantle. Earth and Planetary Science Letters 465, 29–37.

Ohta, K., Yagi, T., Taketoshi, N., Hirose, K., Komabayashi, T., Baba, T., Ohishi, Y., Hernlund, J., 2012. Lattice thermal conductivity of mgsio3 perovskite and post-perovskite at the core–mantle boundary. Earth and Planetary Science Letters 349, 109–115.

Prencipe, M., Zupan, A., Dovesi, R., Apra, E., Saunders, V., 1995. Ab initio study of the structural properties of lif, naf, kf, licl, nacl, and kcl. Physical Review B 51, 3391.

Rainey, E., Hernlund, J., Kavner, A., 2013. Temperature distributions in the laser-heated diamond anvil cell from 3-d numerical modeling. Journal of Applied Physics 114, 204905.

Rainey, E., Kavner, A., 2014. Peak scaling method to measure temperatures in the laser-heated diamond anvil cell and application to the thermal conductivity of mgo. Journal of Geophysical Research: Solid Earth 119, 8154–8170.

Roufosse, M., Klemens, P., 1973. Thermal conductivity of complex dielectric crystals. Physical Review B 7, 5379.

Roufosse, M.C., Jeanloz, R., 1983. Thermal conductivity of minerals at high pressure: the effect of phase transitions. Journal of Geophysical Research: Solid Earth 88, 7399–7409.

Roufosse, M.C., Klemens, P., 1974. Lattice thermal conductivity of minerals at high temperatures. Journal of Geophysical Research 79, 703–705.

Seagle, C.T., Cottrell, E., Fei, Y., Hummer, D.R., Prakapenka, V.B., 2013. Electrical and thermal transport properties of iron and iron-silicon alloy at high pressure. Geophysical Research Letters 40, 5377–5381.

Slack, G.A., Ross, R.G., 1985. Thermal conductivity under pressure and through phase transitions in solid alkali halides. ii. theory. Journal of Physics C: Solid State Physics 18, 3957.

Tiwari, M., 1978. Contribution of optical phonons in lattice thermal conductivity of nacl. Il Nuovo Cimento B (1971-1996) 48, 102–108.

Walker, D., Cranswick, L.M., Verma, P.K., Clark, S.M., Buhre, S., 2002. Thermal equations of state for b1 and b2 kcl. American Mineralogist 87, 805–812.

Whitfield, C.H., Brody, E.M., Bassett, W.A., 1976. Elastic moduli of nacl by brillouin scattering at high pressure in a diamond anvil cell. Review of Scientific Instruments 47, 942–947.

CHAPTER 3

Thermal conductivity of ferropericlase from the high spin to mixed spin state

3.1 Introduction

The thermal conductivity of the mantle mineral assemblage is important for understanding the long term thermal and chemical evolution of Earth. The core-mantle boundary (CMB) region is a thermal boundary layer, where heat is transported primarily by conduction. The bulk thermal conductivity of the mineral assemblage present at the CMB helps determine the heat flow out of the core (Lay et al., 2008). The globally averaged CMB heat flux has wide-ranging implications for (1) the thermal history of the planet, (2) the maintenance of the geodynamo, and (3) the age of the inner core (Buffett, 2000; Olson, 2016). Throughout the mantle, the depth dependence of thermal conductivity is an important parameter for models of mantle convection, and has been shown to influence the structures that result from parameterized convection models (Tosi et al., 2013). A detailed understanding of the thermal conductivity of the major lower mantle minerals can help elucidate the mechanisms behind the emergence of 3D thermo-chemical structures in the mantle, which are known from seismic tomography (French and Romanowicz, 2015).

In a solid dielectric materials, such as the major minerals present in Earth's lower mantle, the thermal conductivity can be described as the sum of lattice, electrical and radiative

components (Klemens, 1969). The dominant transport terms for the oxides and silicates in Earth's mantle are the lattice and radiative components. The lattice component for a single phase increases with pressure, along an isotherm (Dalton et al., 2013). As temperature is increases, the thermal conductivity of mantle oxides and silicates decreases (Roufosse and Klemens, 1974). Assuming that there are no phase transitions, the competing effects of pressure and temperature lead to moderately increasing thermal conductivity as pressure and temperature increase with depth in the Earth's mantle.

Phase transitions can complicate models of the pressure dependence of thermal conductivity. A volume reduction and structural change due to the B1-B2 phase transition in ionic salts has been associated with a decrease in thermal conductivity (Roufosse and Jeanloz, 1983). Experiments detailed in Chapter 2 confirm this theoretical prediction. Recent measurements of thermal diffusivity of (Mg,Fe)O show a decrease across the mixed spin state pressure range at ambient temperature (Ohta et al., 2017; Hsieh et al., 2018). This leads us to ask whether phase transitions in Earth's mantle can cause a decrease in thermal conductivity with pressure.

In this work, we use a finite element heat flow model of the diamond anvil cell in conjunction with high pressure, high temperature measurements to determine thermal conductivity as a function of pressure across a phase transition. Our approach is developed and tested using NaCl across the B1-B2 phase transition, described in Chapter 2. We apply this method to ferropericlase ($Mg_{.76}Fe_{.24}O$), over a pressure range consistent with the high-spin to mixed-spin transition, from 22 GPa to 61 GPa.

3.2 Heat flow modeling

The finite-element 3D heat flow model is used to simulate temperature distributions in the laser-heated diamond anvil cell (Fig. 3.1). The model solves the steady-state heat

equation in three dimensions using a full approximation storage grid method. (Rainey et al., 2013; Rainey and Kavner, 2014) The model is benchmarked to an analytical solution to the nonlinear heat equation in a cylinder, with temperature dependent thermal conductivity (Panero and Jeanloz, 2001).

Heat flow in the diamond anvil cell is dominated by the high thermal mass of the diamonds. The time to thermally equilibrate the sample is on the order of $10^{-6}s$ (Rainey et al., 2013; Geballe and Jeanloz, 2012). For continuous wave laser heating, we assume a steady state heating model:

$$\nabla \cdot \kappa(T) \nabla T + Q = 0 \tag{3.1}$$

Heat transport is assumed to be by conduction. Radiative heat transport will occur in the diamond anvil cell as well; however, the length scale of the sample is small enough ($30\mu m$), that radiative heat transport across the sample is negligible (Manga and Jeanloz, 1997; Rainey et al., 2013).

The model assigns material properties to the diamonds, gasket, pressure transmitting medium and absorber, and allows flexible inputs for the gasket thickness and the radius of the gasket hole. The sample contained by the gasket may be a single material or a combination of an absorbing and transparent material, with both parameterized as a cylinder. Each element in the model is assigned a thermal conductivity with a temperature dependence $k_0(\frac{T_0}{T})^m$, were m is assumed to be 1 for pure materials, but may be as low as 0.5 if impurity scattering is significant. Heat is input to each cell based on the shape of the laser beam profile, an adjustable parameter, so that:

$$\begin{aligned} Q &= \alpha I \qquad \text{beam-present} \\ Q &= 0 \qquad \text{otherwise} \end{aligned} \tag{3.2}$$

If the absorber is opaque, as is the case for a metal foil, then the power input is simply the incident laser power. In the case of a partially absorbing sample, such as ferropericlase, the heat absorbed in each cell is governed by the Beer-Lambert law:

$$\begin{aligned} dQ &= \alpha I \\ Q &= P\big(1 - e^{(\alpha I)}\big) \end{aligned} \tag{3.3}$$

where P, the laser power, is delivered to each cell and decays with depth in the sample.

Model simulations show that the peak temperature in the cell is primarily controlled by the geometry, sample thermal conductivity and heat input due to laser heating (Rainey et al., 2013). Compression will change the thickness of the gasket in addition to the thermal conductivity of the materials in the cell. We explicitly model gasket thickness changes using the equation of state of iron and ferropericlase for the gasket and sample, respectively. This assumes that our experiments are in the thin gasket regime, where the pre-compressed gasket is thin enough that plastic deformation of the gasket does not dominate the change in thickness with compression (Dunstan, 1989). The reduction in thickness due to compression results in a reduction in peak temperature of less than 10 percent. Considerations of modeling sample absorption specific to ferropericlase is discussed in the results section.

3.3 Experiments

Experiments were conducted at beam line 12.2.2 at the Advanced Light Source (ALS) at Lawrence Berkeley National Lab. High temperatures in the diamond anvil cell (DAC) were achieved by single-sided laser heating ($\lambda = 1.07\mu m$). Temperature was measured by spectro-radiometry with a wide-slit spectrometer and 2D high dynamic range camera (Fig 3.1). Details of the laser heating system and temperature measurement are described elsewhere (Kunz et al., 2005; Rainey and Kavner, 2014).

The experiment was carried out on $(Mg, Fe)O$ single crystal sample synthesized by interdiffusion of Fe and Mg with pure MgO single crystal, on loan from Jacobsen et al. (2002). Chemical composition, $(Mg_{.76}Fe_{.24}O)$, and oxidation state, $Fe^{3+}/\sum Fe < 0.01$, was determined by microprobe analysis and Mössbauer spectroscopy, respectively (Jacobsen et al., 2002). A spring steel gasket was pre-compressed to 33 μm in a DAC aligned with 300μm diamonds. A gasket hole was laser milled with 100μm hole in diameter. A small amount of ruby power, as a pressure calibrant, was loaded onto the piston side diamond. The ferropericlase sample was loaded on top of the ruby powder and then gas loaded with neon, which serves as both the pressure transmitting medium and insulator.

A heating cycle was conducted at a series of pressures. The heating cycle constructs a temperature versus laser power (T-LP) curve by increasing the laser power until blackbody radiation is observed in the 2D imaging spectrometer. A temperature measurement is made at 0.5 watt increments as the laser power is increased (Fig. 3.1). In all T-LP cycles, the peak temperature increases with laser power until reaching a plateau. The plateau cannot be uniquely assigned to physical properties of the materials in the cell (Geballe and Jeanloz, 2012). We collect T-LP curves until the plateau is observed, and then reduce power, until blackbody radiation is no longer observable. T-LP curves were measured at 22, 32, 42, 52 and 61 GPa.

3.4 Results

The peak temperature versus laser power results for ferropericalse are shown in Figure 3.2. The temperature curve for one pressure is compared to the temperature curve at a higher pressure. A curve that shifts to the right with a pressure increase indicates that the thermal conductivity has increased. A simple way to understand this result is that for a curve that shifts to the right, the temperature at the same laser power decreases, which is consistent with

more efficient heat removal (i.e. higher thermal conductivity). The temperature difference at the same laser power indicates both the sign and magnitude of the change in thermal conductivity of the sample. If the temperature increases as pressure is increased, then heat is less effectively removed, and the thermal conductivity of the sample has decreased. With this basic framework in mind, Figure 3.2 shows that the thermal conductivity increases from 22 to 32 GPa and again up to 42 GPa. But from 42 to 52 GPa, and again to 61 GPa, the thermal conductivity decreases.

In order to quantify changes in thermal conductivity with pressure, we use the 3D heat flow model, in an iterative fashion. The model laser power (LP*) is tuned to the lowest pressure measurements using approximate ambient temperature thermal conductivity (a) (κ_0) of the partially absorbing (Mg,Fe)O sample, (b) (κ_0) of the Ne pressure medium and (c) the measured thickness of the gasket after pre-compression. A complication with the partially absorbing sample is the treatment of laser power absorption as a function of depth through the sample. The absorption coefficient for $(Mg_{1-x}, Fe_x)O$, with $x = .24$, has been measured at high pressure and room temperature conditions (Goncharov et al., 2006). We use this data as an approximation of the absorption coefficient at high pressure, high temperature conditions. The thermal conductivity of the neon pressure transmitting medium is not known precisely, but a model based on the equation of state of neon can constrain the pressure dependence of its thermal conductivity (Weston and Daniels, 1984).

The thermal conductivity change for the first pressure step, from 22 to 32 GPa, is solved for iteratively using LP* from the 22 GPa temperature curve. The pressure steps from 42 GPa to 52 GPa use a new LP*, re-calculated to the 42 GPa curve. This LP* is also used for the 52 GPa to 61 GPa pressure step. The modeling results for each pressure step and laser power are given in Tables 3.1 and 3.2. As a check, the LP* from 42 GPa is also used to calculate 22 and 32 GPa curves and gives similar results.

The results presented in Figure 3.3 show the log-normalized thermal conductivity as a function of normalized density ($\frac{dln\kappa}{dln\rho}$) for $(Mg, Fe)O$. The values in Figure 3.3 are the change in thermal conductivity required by the heat flow model to reproduce experimentally observed temperatures at the higher of two pressure steps, normalized to ambient temperature and 1 bar condition values. Thermal conductivity increases from 22 to 32 GPa. This pressure range is consistent with the high spin state of ferropericlase (Badro et al., 2003). The pressure slope of thermal conductivity is positive from 22 to 32 Gpa and up to 42 Gpa, where ($\frac{dln\kappa}{dln\rho}$) = 4.0, and ($\frac{dln\kappa}{dln\rho}$) = 14.2, at each pressure step respectively. Over the pressure range of 22 to 42 GPa, a linear regression to the heat flow model results gives a g-value, $\frac{dln\kappa}{dln\rho} = 8.5 \pm 1.8$. At higher pressures, the thermal conductivity decreases from 42 to 52 GPa ($\frac{dln\kappa}{dln\rho}$) = -4.6 and again from 52 to 61 GPa ($\frac{dln\kappa}{dln\rho}$) = -11.2. The cause of the decrease with pressure is explored below.

3.5 Discussion

The thermal conductivity in a dielectric material can be described by the Boltzmann transport equation (Ziman, 1972; Tang and Dong, 2010):

$$\kappa_{lat} = \frac{1}{V_{BZ}} \left[\int_{BZ} \sum_{i} C_v(i,k) v(k,i) l(k,i)/3 \right] dk \tag{3.4}$$

where C_v is the phonon heat capacity, v is the group velocity, l is the mean free path, summed over the phonon modes (i) and k-points in the Brillouin zone (BZ). In general, thermal conductivity of a single phase increases with pressure, since the majority of heat is transported by acoustic phonons, and since the sound speed in most materials increases with pressure (Roufosse and Klemens, 1973). LS theory makes this observation quantitative, and the thermal conductivity as a function of pressure is given by the following set of equations

(de Koker, 2010):

$$\kappa = \kappa_0 \left(\frac{\rho}{\rho_0}\right)^g \left(\frac{T_0}{T}\right)^m \tag{3.5}$$

The exponent, $g = 3\gamma + 2q - 1/3$, is related to the Gruneisen parameter (γ) and its volume derivative ($q = -(\frac{dln\gamma}{dlnV})_T$). The g parameter can be determined from the thermal equation of state of the material. The exponent, m, in Eq. 5 allows the temperature dependence to depart from the 1/T ideal relationship, due, for example, to the effects of impurity scattering (Manthilake et al, 2011).

The prediction of the thermal conductivity pressure dependence from Eq. 5 matches measurements from 22 to 32 GPa using the thermal equation of state of $(Mg, Fe)O$. Over this same pressure range, the theoretical value of g is 5.6 for ferropericlase (compared with our experimental value of 4.0) (Jacobsen et al., 2005). Including the 42 GPa results significantly increases the g-value, to 8.5 $\pm$ 1.8, higher than the theoretical, equation-of-state-derived value of 5.6. This result is consistent with thermal conductivity measurements of a similar composition, $(Mg_{.81}, Fe_{.19})O$, by time-resolved methods (Goncharov et al., 2015). However, Eq. 5 does not predict the reduction in thermal conductivity at higher pressures that is observed in our data set. Using the same underlying assumptions (e.g. Liebfried-Schlomann) it is possible to reformulate Eq. 5 in terms of more useful quantities:

$$\kappa_{lat} = A\frac{v^3\rho}{3\gamma^2 T} \tag{3.6}$$

where v is the phonon wave speed, ρ is density, γ is the Gruneisen parameter, and A is a constant that does not depend on pressure (Roufosse and Jeanloz, 1983). A model for mixed spin reduction in thermal conductivity can be constructed using the thermal equation of state with Eq. 6. We use published K_S values across the spin transition to calculate

the bulk sound velocity $\left(\sqrt{\frac{K_S}{\rho}}\right)$ and substitute these values directly into Eq. 6 (Lin et al., 2013). The constant A is calculated using ambient pressure and temperature values. This calculation is shown with our measurements in Fig. 3.4.

The results are consistent with previous measurements of thermal diffusivity at high pressure and ambient temperature (Ohta et al., 2017). The magnitude of the reduction in thermal conductivity required by our data is larger and over a broader pressure range than that previously reported by (Ohta et al., 2017), possibly due to the fact that our measurements are at high temperatures, where the mixed spin state extends over a wider phase space (Tsuchiya et al., 2006; Holmström and Stixrude, 2015).

3.6 Conclusion

The thermal conductivity of minerals across phase transitions has important implications for the thermal evolution of the planet. We have shown that $(Mg, Fe)O$ exhibits an anomalous lattice thermal conductivity decrease with pressure in the mixed spin state. This decrease could produce an unusual depth profile of thermal conductivity through the Earth's mantle. In order to investigate this further, we calculate a simple mixture model of the thermal conductivity of major lower mantle phases. The thermal conductivity of Fe-bearing bridgmanite, $(Mg, Fe)SiO_3$, has been previously measured up to 58 GPa using the techniques describe here (Rainey, 2014). We use a Voigt-Reuss-Hill averaging scheme, with 20% ferropericlase and 80% bridgmanite, by volume, to calculate the thermal conductivity of the lower mantle. This calculation is shown in Figure 3.5. The thermal conductivity as a function of pressure levels off over the pressure range of 45 to 60 GPa.

This result suggests that thermal conductivity may not be a strong function of depth for a significant portion of the lower mantle, especially given that the mixed spin state of

ferropericlase occupies a broader phase space at high temperatures and may even extend to the core-mantle boundary (Holmström and Stixrude, 2015). A weakly pressure dependent thermal conductivity in the mantle could have profound implications for the style of mantle convection, the shape of plumes, and the stagnation of downwelling slabs (Tosi et al., 2013). A model for thermal conductivity of ferropericlase through the mantle, accounting for spin transition is presented in Chapter 6.

P (GPa)	τ	Temp (K)	LP_{data} (W)	LP_{model} (W)	K_0 (W/mK)
22	4.3002	1367	5.8	1.70014	11.4
		1684	7.2	1.85582	9.9
		1767	8.0	1.94694	10.3
		1837	8.6	2.01903	10.3
		1916	9.5	2.12278	10.7
32	4.5689	1192	7.4	1.70014	13.8
		1367	8.1	1.85582	11.9
		1478	8.55	1.94694	11.1
42	5.3117	1055	12.5	2.45945	21.8
		1124	13.1	2.52209	20.4
		1181	13.8	2.61092	20
		1274	14.6	2.69861	18.7

Table 3.1: Temperature and laser power data for $(Mg_{1-x}, Fe_x)O$, where x = 0.24, with modeling laser power inputs and thermal conductivity results, for 22 GPa to 42 GPa.

P (GPa)	τ	Temp (K)	LP_{data} (W)	LP_{model} (W)	K_0 (W/mK)
52	7.4300	1186	5.8	2.29573	17.4
		1232	7.2	2.42066	18.0
		1274	8.0	2.46692	17.7
		1337	8.6	2.51805	17.0
62	7.9692	1177	5.8	2.00286	12
		1313	7.2	2.20151	12 (set)
		1381	8.0	2.29456	12 (set)
		1443	8.6	2.37775	12 (set)
		1479	8.6	2.42526	12 (set)

Table 3.2: Temperature and laser power data for $(Mg_{1-x}, Fe_x)O$, where x = 0.24, with modeling laser power inputs and thermal conductivity results, for 52 GPa to 62 GPa.

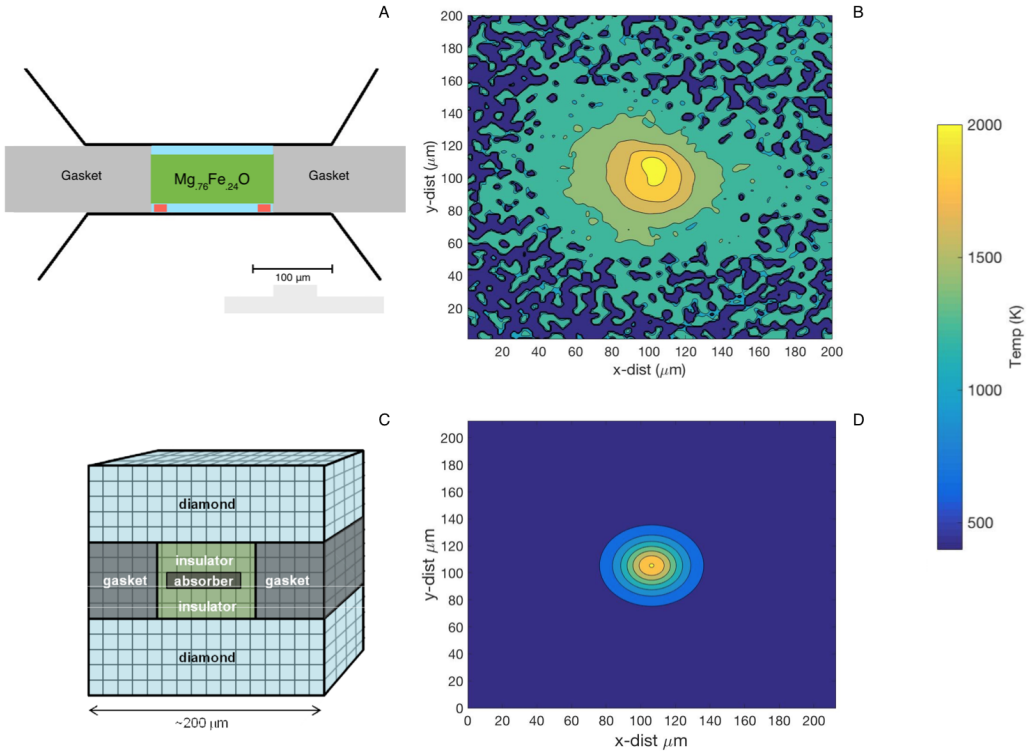

Figure 3.1: Experimental and model setup. (a) The the ferropericlase sample ($Mg_{.76}Fe_{.24}O$) is loaded in neon (shown in blue) pressure transmitting medium. Ruby power (orange squares) is added on culet, opposite side of laser heating. (b) Example of a 2D temperature measurement using the peak scaling method at ALS beamline 12.2.2, with a peak temperature of 1705 K. (c) Heat flow model finite element parameterization, with flexible inputs for geometry and material properties. (d) Example of a 2D slice of the model output, converged to 1705 K by iteratively changing the thermal conductivity of the sample.

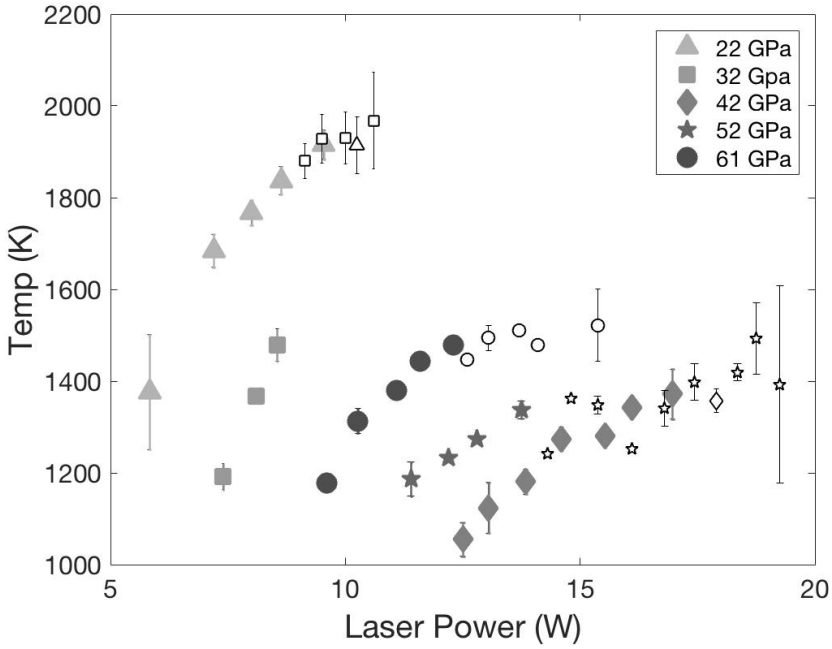

Figure 3.2: Measured peak temperature is plotted versus laser power for $Mg_{.76}Fe_{.24}O$. Error bars represent the standard deviation of 3-5 measurements at the same laser power. Filled symbols show T-LP curves before plateau, open symbols show the plateau, which is not considered in modeling.

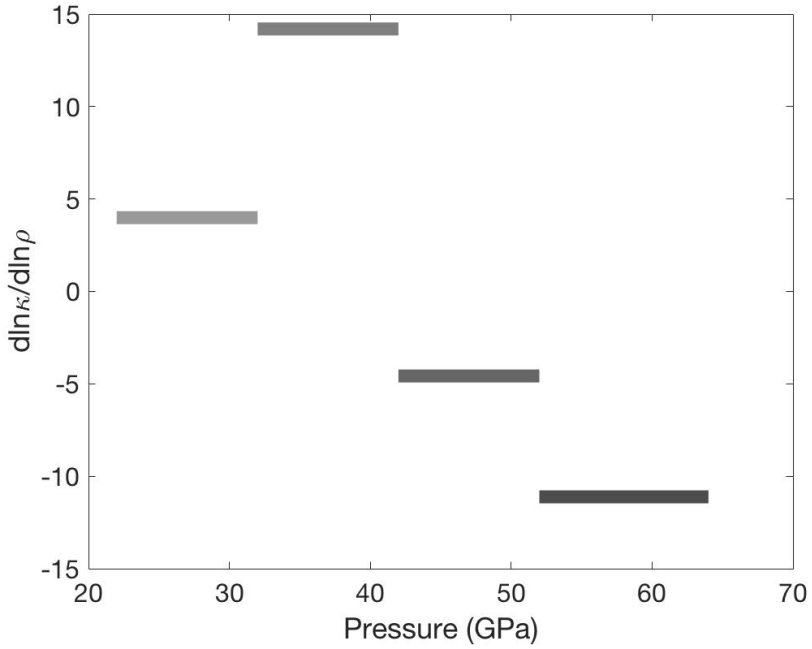

Figure 3.3: The logarithmic slopes (g-values) of thermal conductivity with respect to density if plotted against pressure. From 22 to 42 GPa, the slopes are positive, and from 42 to 64 GPa, the slopes are negative, indicating that the pressure dependence of thermal conductivity has flipped sign starting at 42 GPa.

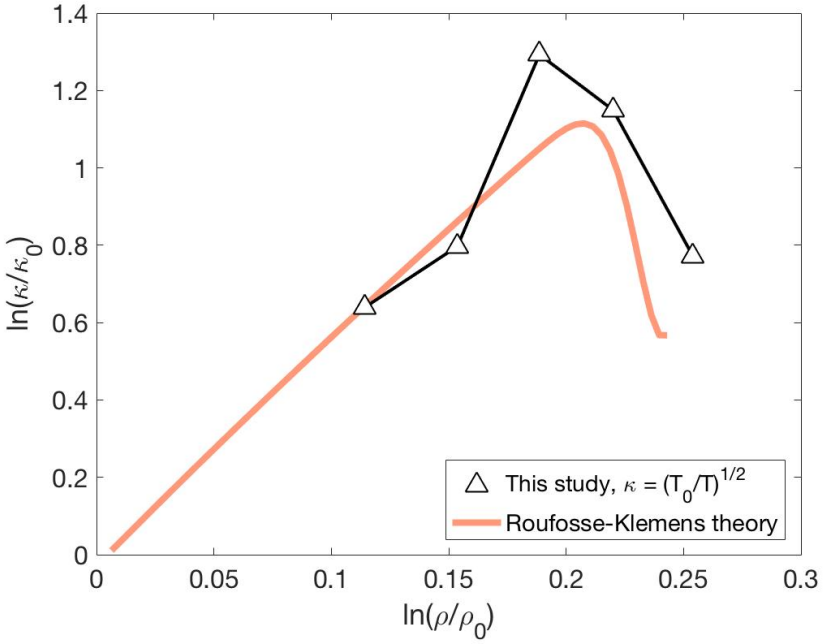

Figure 3.4: The log-normalized thermal conductivity required by our temperature data is plotted given assumptions about the temperature dependence of thermal conductivity. The model based on LS theory and bulk sound velocity is shown in the solid orange line.

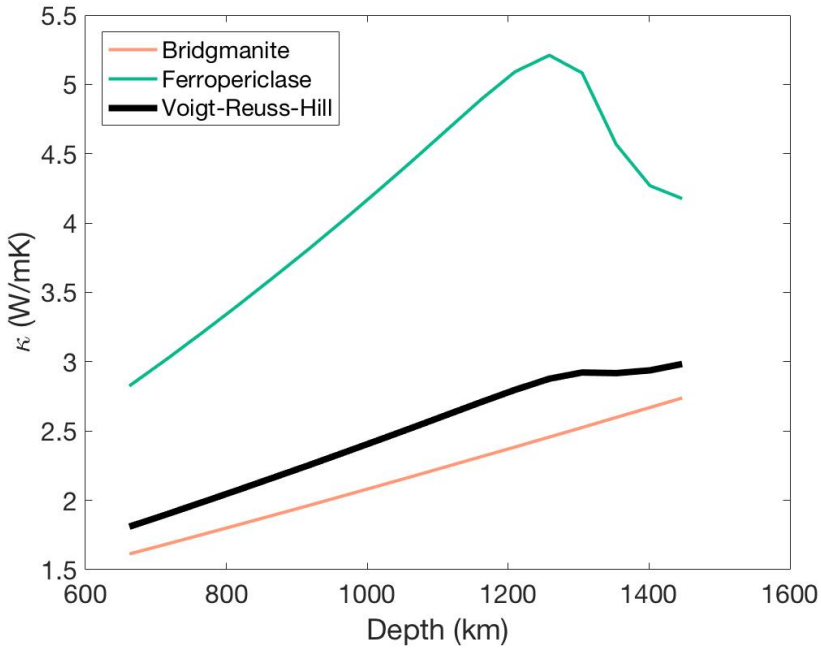

Figure 3.5: Thermal conductivity of ferropericlase (solid green line) and Fe-bearing bridgmanite (solid orange line), at 300 K with the Voigt-Reuss-Hill volumetric average of the lower mantle, assuming pyrolite composition.

Bibliography

Badro, J., Fiquet, G., Guyot, F., Rueff, J.P., Struzhkin, V.V., Vankó, G., Monaco, G., 2003. Iron partitioning in earth's mantle: toward a deep lower mantle discontinuity. Science 300, 789–791.

Buffett, B.A., 2000. Earth's core and the geodynamo. Science 288, 2007–2012.

Dalton, D.A., Hsieh, W.P., Hohensee, G.T., Cahill, D.G., Goncharov, A.F., 2013. Effect of mass disorder on the lattice thermal conductivity of mgo periclase under pressure. Scientific reports 3, 2400.

Dunstan, D., 1989. Theory of the gasket in diamond anvil high-pressure cells. Review of Scientific Instruments 60, 3789–3795.

French, S.W., Romanowicz, B., 2015. Broad plumes rooted at the base of the earth's mantle beneath major hotspots. Nature 525, 95.

Geballe, Z.M., Jeanloz, R., 2012. Origin of temperature plateaus in laser-heated diamond anvil cell experiments. Journal of applied physics 111, 123518.

Goncharov, A.F., Lobanov, S.S., Tan, X., Hohensee, G.T., Cahill, D.G., Lin, J.F., Thomas, S.M., Okuchi, T., Tomioka, N., 2015. Experimental study of thermal conductivity at high pressures: Implications for the deep earths interior. Physics of the Earth and Planetary Interiors 247, 11–16.

Goncharov, A.F., Struzhkin, V.V., Jacobsen, S.D., 2006. Reduced radiative conductivity of low-spin (mg, fe) o in the lower mantle. Science 312, 1205–1208.

Holmström, E., Stixrude, L., 2015. Spin crossover in ferropericlase from first-principles molecular dynamics. Physical review letters 114, 117202.

Hsieh, W.P., Deschamps, F., Okuchi, T., Lin, J.F., 2018. Effects of iron on the lattice thermal conductivity of earths deep mantle and implications for mantle dynamics. Proceedings of the National Academy of Sciences , 201718557.

Jacobsen, S.D., Reichmann, H.J., Spetzler, H.A., Mackwell, S.J., Smyth, J.R., Angel, R.J., McCammon, C.A., 2002. Structure and elasticity of single-crystal (mg, fe) o and a new method of generating shear waves for gigahertz ultrasonic interferometry. Journal of Geophysical Research: Solid Earth 107.

Klemens, P., 1969. Thermal conductivity, vol. 1, edited by rp tye. Academic (New York, 1969) p 1.

de Koker, N., 2010. Thermal conductivity of mgo periclase at high pressure: implications for the d region. Earth and Planetary Science Letters 292, 392–398.

Kunz, M., MacDowell, A.A., Caldwell, W.A., Cambie, D., Celestre, R.S., Domning, E.E., Duarte, R.M., Gleason, A.E., Glossinger, J.M., Kelez, N., et al., 2005. A beamline for high-pressure studies at the advanced light source with a superconducting bending magnet as the source. Journal of synchrotron radiation 12, 650–658.

Lay, T., Hernlund, J., Buffett, B.A., 2008. Core–mantle boundary heat flow. Nature Geoscience 1, 25.

Lin, J.F., Speziale, S., Mao, Z., Marquardt, H., 2013. Effects of the electronic spin transitions of iron in lower mantle minerals: Implications for deep mantle geophysics and geochemistry. Reviews of Geophysics 51, 244–275.

Manga, M., Jeanloz, R., 1997. Thermal conductivity of corundum and periclase and implications for the lower mantle. Journal of Geophysical Research: Solid Earth 102, 2999–3008.

Ohta, K., Yagi, T., Hirose, K., Ohishi, Y., 2017. Thermal conductivity of ferropericlase in the earth's lower mantle. Earth and Planetary Science Letters 465, 29–37.

Olson, P., 2016. Mantle control of the geodynamo: Consequences of top-down regulation. Geochemistry, Geophysics, Geosystems 17, 1935–1956.

Panero, W., Jeanloz, R., 2001. Temperature gradients in the laser-heated diamond anvil cell. Journal of Geophysical Research: Solid Earth 106, 6493–6498.

Rainey, E., Hernlund, J., Kavner, A., 2013. Temperature distributions in the laser-heated diamond anvil cell from 3-d numerical modeling. Journal of Applied Physics 114, 204905.

Rainey, E., Kavner, A., 2014. Peak scaling method to measure temperatures in the laser-heated diamond anvil cell and application to the thermal conductivity of mgo. Journal of Geophysical Research: Solid Earth 119, 8154–8170.

Rainey, E.S.G., 2014. The Thermal Conductivity of the Earth's Lower Mantle and Implications for Heat Flow at the Core-Mantle Boundary. University of California, Los Angeles.

Roufosse, M., Klemens, P., 1973. Thermal conductivity of complex dielectric crystals. Physical Review B 7, 5379.

Roufosse, M.C., Jeanloz, R., 1983. Thermal conductivity of minerals at high pressure: the effect of phase transitions. Journal of Geophysical Research: Solid Earth 88, 7399–7409.

Roufosse, M.C., Klemens, P., 1974. Lattice thermal conductivity of minerals at high temperatures. Journal of Geophysical Research 79, 703–705.

Tang, X., Dong, J., 2010. Lattice thermal conductivity of mgo at conditions of earths interior. Proceedings of the National Academy of Sciences 107, 4539–4543.

Tosi, N., Yuen, D.A., de Koker, N., Wentzcovitch, R.M., 2013. Mantle dynamics with pressure-and temperature-dependent thermal expansivity and conductivity. Physics of the Earth and Planetary Interiors 217, 48–58.

Tsuchiya, T., Wentzcovitch, R.M., da Silva, C.R., de Gironcoli, S., 2006. Spin transition in magnesiowüstite in earths lower mantle. Physical Review Letters 96, 198501.

Weston, H., Daniels, W., 1984. Temperature and volume dependence of the thermal conductivity of solid neon. Physical Review B 29, 2709.

Ziman, J.M., 1972. Principles of the Theory of Solids. Cambridge university press.

CHAPTER 4

Isothermal equation of state and phase stability of Fe_5Si_3 up to 96 GPa and 3000 K

4.1 Introduction

The light element(s) in the core play important roles in our understanding of Earth's current state, chemical evolution and core formation process. The coupled core-mantle thermal and chemical evolution depends on light element concentrations in the core. In addition, the light elements' ability to alter the electronic structure of liquid iron helps determine the thermal and electrical properties of the outer core that are responsible for the Earth's geodynamo (de Koker et al., 2012; Pozzo et al., 2012; Vočadlo, 2015). However, the identity of the primary alloying element is not certain (see Vočadlo (2015) for a review). Silicon is a candidate for the major light element in the core based on its geochemical abundance and alloying properties with iron at high pressures and temperatures (Ringwood, 1977; Poirier, 1994; Allègre et al., 2001; Lin et al., 2003). Recent estimates of the thermoelastic properties of Fe-Si alloys at high pressures and temperatures provide an improved match to the geophysically observed properties of the core, compared with other light elements (Badro et al., 2007; Antonangeli et al., 2010). Modeling the physical and chemical behavior of the core at the relevant high pressures and temperatures requires thermodynamic data of the candidate iron alloys, including the phase stability diagram of alloys and compounds, and their equations of state at high pressures and temperatures.

Here we present measurements of the high pressure and high temperature phase stability and isothermal (room temperature) equation of state of an intermetallic Fe-Si compound, Fe_5Si_3, and the mineral xifengite, at pressures up to 96 GPa under hydrostatic conditions. We also make measurements of the stable structures at high temperature and at room temperature after quenching, providing new high pressure phase diagram information.

At ambient conditions, the Fe-FeSi phase diagram is complex, with known stoichiometric phases Fe_2Si, Fe_5Si_3, $FeSi$, and $FeSi_2$ (Brandes and Brook, 2013). High pressure and temperature experimental studies of the Fe-FeSi system suggest that it may simplify at core conditions relative to ambient pressure, due to a lack of compositional intermediate phases with distinct crystal structures Kuwayama et al. (2008); Fischer et al. (2013); Tateno et al. (2015). Theoretical work on the Fe-FeSi phase diagram has shown that the intermediate stoichiometric phase Fe_5Si_3 is not stable with respect to the ordered alloy phase (DO_3, isostructural with Fe_3Si) and FeSi at the pressures and temperature conditions of the Earth's core (Brosh et al., 2009; Zhang and Oganov, 2010; Caracas, 2016). Experimental work on the Fe-FeSi system provides support for this prediction, but the stability of Fe_5Si_3 at high pressure and high temperature has not been experimentally determined.

The crystal structure and pressure–volume equation of state for Fe_5Si_3 has been measured at room temperature to 75 GPa using NaCl and silicone oil as pressure transmitting media (Santamarıa-Pérez et al., 2004; Errandonea et al., 2008). The use of NaCl and silicone oil as pressure transmitting media has been shown to result in nonhydrostatic conditions at room temperature, which may cause an overestimation of volume as a function of pressure, biasing the equation of state to a stiffer bulk modulus (Kinsland and Bassett, 1976; Shen

et al., 2004). In the present study, the pressure range is extended to 96 GPa using noble gas (Ne and Ar) as pressure transmitting medium, to achieve improved hydrostatic conditions in the diamond anvil cell.

Our revised quasihydrostatic equation of state for Fe_5Si_3 can be combined with existing data on the equation of state of alloys and compounds within the Fe-FeSi system (Dobson et al., 2002; Santamaría-Pérez and Boehler, 2008; Geballe and Jeanloz, 2014; Fischer et al., 2013) to help constrain thermodynamic models of the mixing behavior of Si substitution within Fe metal.

4.2 Experiment and Methods

Samples of Fe_5Si_3 were synthesized by solid-state reaction using the method detailed in (Errandonea et al., 2008). Two diamond cells with 100 μm culet diamonds were prepared with precompressed Re metal gaskets and a 50 μm hole centered on the culet. The cells were loaded with polycrystalline Fe_5Si_3 compressed into a foil and ruby chips for pressure calibration (Mao et al., 1986). KCl was used in both cells to thermally isolate the laser-absorbing Fe_5Si_3 from the diamond surface and as an internal pressure calibrant (Walker et al., 2002).

Both samples were loaded with noble gas pressure media to maintain a hydrostatic environment. The first sample was loaded with Ar, and room temperature diffraction patterns were collected at three pressure steps up to 18 GPa. At this pressure, the cell was laser heated to 2800 K, quenched, and then increased to 38 GPa. The diamonds failed during a second heating attempt. The second sample was loaded with Ne as a pressure medium, and

Xray diffraction patterns were made in pressure steps of about 5 GPa up to 96 GPa before laser heating at that pressure. Two laser heating and temperaturequenched runs were completed at 96 GPa, with a maximum temperature of 3600 K. The diamonds failed during the first decompression step, so we were unable to collect Xray diffraction data during decompression. The sample was preserved in the gasket, and ambient pressure and temperature patterns were taken to determine the stable phase at these conditions. Additional pressure calibration was obtained using the equation of state of solid Ne (Dewaele et al., 2008).

Laser heating and X-ray diffraction experiments were performed at the GSECARS 13 IDD beamline at the Advanced Photon Source (Prakapenka et al., 2008). High temperatures were generated using an $1.07\mu m$ fiber laserbased doublesided heating system (Shen et al., 2004), and temperature was measured using the installed spectrometer systems and the gray body approximation. The alignment of the 3 x 3 μm Xray beam and the 20 μm laserheated spot was checked before and after each heating cycle by examining for agreement between the position of Xray fluorescence and the position of the hotspot.

Xray diffraction patterns of the sample were obtained using monochromatic radiation $\lambda = 0.3344$Å. Patterns were measured before, during, and after heating at each pressure step and collected on a two-dimensional MAR 345 image plate, with the sample-to-detector distance calibrated by a CeO_2 standard. The software package Dioptas (Prescher and Prakapenka, 2015) was used to integrate the two-dimensional diffraction images into one-dimensional intensity–2θ data. Diffraction pattern indexing at each pressure and temperature step was carried out using the PowderCell (Kraus and Nolze, 1998) and FullProf (Rodríguez-Carvajal, 1993) program packages.

4.3 Phase Stability

The preheat diffraction pattern is compared with the high temperature and quench patterns at 18 GPa in Figure 4.1. Prior to heating, diffraction patterns corresponding to the Fe_5Si_3 structure, KCl, and Ar are present. At high temperature, diffraction peaks corresponding with Fe_5Si_3 structure ($P6_3/mcm$) disappear as soon as the laser couples with the sample. Figure 1b shows a representative diffraction pattern at 18 GPa and 1800 K. We are able to fit the diffraction peaks present (that are not KCl and Ar) with two cubic structures: Fm3m ($a = 5.548$Å) and $P2_13$ ($a = 4.405$Å), compatible with Fe_3Si and the B20 phase of FeSi, respectively (Fig. 4.2). It is important to note that ordered Fe–Si alloy with the DO_3 structure is indistinguishable from stoichiometric Fe_3Si, from Xray diffraction (XRD) data alone. When the laser is turned off, peaks corresponding to the $P6_3/mcm$ structure Fe_5Si_3 reappear. Diffraction peaks from the Fm3m and $P2_13$ structures remain after laser heating is turned off.

A second cell was compressed to 96 GPa before laser heating at that pressure. Peaks from Fe_5Si_3 disappear as soon as the laser begins to couple (Figure 4.3). When heated to temperatures below 2500 K, new peaks immediately appear; however, these could not be indexed with a cubic Fm3m phase nor does a body-centered tetragonal distortion of the cubic phase match the peaks (I4/mmm subgroup of Fm3m). The existence of a Fe-rich, hcp-structured alloy was also ruled out. A satisfactory indexing can be achieved with the Pm3m (B2) structure ($a = 2.605$Å), consistent with the B2 unit cell of FeSi. As the sample was laser heated to temperatures above 2500 K, additional diffraction peaks appeared that could not be identified from diffraction alone. A reaction with the Re gasket is plausible, given the high temperatures and pressures reached during this run.

These results show that Fe_5Si_3 is not stable at high temperatures and pressures. While X-ray diffraction alone, as used here, cannot unequivocally demonstrate the stability of phases, the evidence presented in this study is consistent with theoretical predictions that intermediate silicides are unstable at core conditions with respect to a Fe_3Si-like Fe-Si alloy structure and B2 FeSi (Brosh et al., 2009; Zhang and Oganov, 2010; Caracas, 2016). Experimental studies have shown that at pressures above 60 GPa, DO_3 FeSi alloys decompose into Si-poor hcp FeSi alloy and Si-rich B2 phase (Lin et al., 2002, 2009; Fischer et al., 2012; Tateno et al., 2015). The reappearance of Fe_5Si_3 diffraction peaks at room temperature provides evidence that the $P6_3/mcm$ structure of Fe_5Si_3 is stable at ambient temperature and high pressure.

Combined with previous theory and experiment, the present study shows that the Fe-FeSi T-X phase diagram is simpler at high pressure than at ambient pressure (Brandes and Brook, 2013; Fischer et al., 2013). Previous experiments, which have used FeSi alloys and B2 FeSi as end-members to investigate the T-X phase diagram, are justified in ignoring compositional intermediates, since these phases are not stable at the relevant pressures and temperatures (Lin et al., 2002; Fischer et al., 2013).

4.4 Isothermal equation of state

The isothermal equation of state of Fe_5Si_3 was measured at room temperature up to 96 GPa. Integrated powder X-ray diffraction patterns taken at room temperature and elevated pressure were indexed based on the Fe_5Si_3 structure (Fig. 4.4), and the best fit volume was calculated for the diffraction pattern at each pressure (Fig. 4.5). A nonlinear least squares fit of our Fe_5Si_3 volume as a function of pressure to the third-order Birch-Murnaghan equation

of state (EOS) was done using the LevenbergMarquardt algorithm. The value for V_0 was determined from XRD of the quenched sample, from the run that went to 96 GPa. Our fits for both isothermal compression runs together (Ne and Ar pressure media) give $K_{T,0} = 167(8)$ GPa and $K'_{T,0} = 5.1(2)$.

Our new EOS for Fe_5Si_3 has a lower bulk modulus than those obtained in previous experiments, as shown in Figure 4.5 and Table 4.1 (Errandonea et al., 2008; Santamarıa-Pérez et al., 2004). The difference between our bulk modulus and previous experiments is about 25% when compared with silicone oil pressure medium results and about 40% when compared with NaCl pressure medium results. One possible explanation for this discrepancy is that the earlier experiments were run using silicone oil and NaCl as pressure media, and their first pressure derivative, $K'_{T,0} < 4$ (see Table 4.1). Both of these media can retain significant differential stress during compression at room temperature, thus biasing the X-ray determined lattice parameter values upward due to the combined effects of an excess uniaxial stress component in the diamond cell and the diamond cell normal X-ray geometry (Kinsland and Bassett, 1976). The Ar and Ne noble gas pressure media employed in our study helps guarantee a more quasihydrostatic environment.

A plot of the data using normalized pressure (F) versus Eulerian strain coordinates (Fig. 4.6) highlights the deviation of the data from the thirdorder Birch-Murnaghan functional form (Heinz and Jeanloz, 1984). Uncertainties in normalized pressure and strain are calculated according to propagation of errors (Heinz and Jeanloz, 1984). A linear fit to the data set on the F-f plot gives the y intercept ($K_{T,0} = 167$ GPa) and the slope of 290 GPa/f which implies a $K'_{T,0}$ of 5.1, indicating departure from $K_{T,0} = 4$ (i.e., if slope = 0, $K_{T,0} = 4$; if slope > 0, $K_{T,0} > 4$). The F-f plot (Fig. 4.6) shows some departure from a straight line, at low strain values. Such a shape for an F-f plot can indicate an error in V_0. As a visual example,

V_0 was increased and decreased by 0.2% and a synthetic F-f curve was recalculated (Fig. 4.6, red lines), keeping other parameters the same. The shape of the data suggests that our measured V_0 is too large. Correlation of errors between the isothermal bulk modulus, its pressure derivative, and the initial volume are well known (Wolf et al., 2015).

It is noteworthy that our best fit EOS indicates that the compressional elastic behavior of Fe_5Si_3 is similar to that of pure iron (Table 4.1). To examine the mixing trends between iron and silicon, we calculate two end-member substitutional ideal mixing scenarios in the Fe-FeSi system at pressures corresponding to the outer core. For one end-member, the crystal structure of FeSi (B2 structure) is used as a starting point, and the volume is calculated at 137 GPa from the equation of state of FeSi (Fischer et al., 2014). The corresponding density as a function of iron content is calculated, assuming ideal iron substitution for silicon, without change in lattice parameter. For the other end-member, the volume of hcp iron is calculated at 137 GPa (and room temperature) using the values in Table 4.1, and the corresponding Fe end-member density is used as a starting point for ideal Si substitution in the iron lattice (again, without changing in the lattice parameters). The results of these calculations are shown as parallel ideal mixing trends in Figure 4.7.

A comparison of measured Fe-Si alloy and iron silicide compound density data (calculated at 137 GPa and room temperature) with the trends provided by the ideal mixing relationships gives an indication of the thermodynamic mixing activity coefficients and their deviation from ideality (Fig. 4.7). The density of FeSi alloys plot below the mixing line determined by adding Si to Fe, by $\delta\rho = 2.0\%$ (Hirao et al., 2004; Fischer et al., 2014). This corresponds to an effective expansion of the Fe lattice as Si is incorporated; alternatively, this can be interpreted as an increase in bulk modulus for the Fe-alloy as Si is added. The DO_3 structure alloy and compounds Fe_5Si_3 and FeSi plot below the hcp Fe-Si ideal mixing

line by $\delta\rho = 3.6\%$. This deviation is expected since the intermediate structures are not close packed and a change in crystal structure is, de facto, evidence of nonideality. Surprisingly, the DO_3 structure alloy and Fe–Si compounds plot nearly along a mixing line from the FeSi end-member.

The deviations in density due to lattice contraction/elastic stiffening of the Fe-Si alloys and a change in phase are on the same order. This observation may explain why Fischer et al. obtain very consistent values for the maximum Si content in Earth's core, centered at 11.3 ± 0.6 wt % Si, regardless of whether stoichiometric B2 FeSi or alloy phases are used in the linear mixing scheme. Since Fe_5Si_3 and FeSi plot on the same mixing line, a hypothetical mixing model of either of these phases with pure iron would arrive at the same maximum for Si in the core to match seismic observations.

Currently, there are significant efforts to produce accurate, predictive models for multi-component systems of iron, with the goal of understanding the diversity of planets in our solar system and around other stars (Unterborn et al., 2016). A significant challenge for such models is incorporating solid solution and predicting the formation of an alloy versus a compound. Our measurements will, more broadly, provide experimental evidence for future modeling efforts of planetary formation thermodynamics. The addition of Si in the Fe-FeSi system contributes only small changes to the molar volume, even in the case of different crystal structures. This result, coupled with our observation that Fe_5Si_3 is stable at high pressure and room temperature, provides important information for thermodynamic and first-principles models of the mixing of Fe and Si.

In summary, the investigation of Fe_5Si_3 at high pressures and high temperatures shows

that this stoichiometric compound is not stable at Earth's core conditions. The present study provides evidence that the B2 FeSi and the Fe_3Si structures are the preferred phases, as predicted by previous theoretical and experimental work on the Fe-FeSi phase diagram (Brosh et al., 2009; Zhang and Oganov, 2010; Fischer et al., 2013; Tateno et al., 2015). The stability of Fe_5Si_3 at high pressure and ambient temperature indicates a new point on the highpressure phase diagram. The revised isothermal EOS of Fe_5Si_3 in the present study reveals similar compressibility as pure iron. Our revision significantly lowers the bulk modulus of Fe_5Si_3 from previous measurements. Broadly for the Fe-FeSi system, the addition of Si in hcp alloys increases molar volume, while the addition of Si in ordered alloys (DO_3 structure) and compounds has little effect on molar volume. The implications of these results are that differences in crystal structures in the Fe-FeSi system play a minor role in density changes at high pressure, meaning that linear mixing of endmembers can reasonably approximate the maximum Si that can satisfy observations from seismology.

Material	$\rho_0(g/cm^3)$	$V_0(cm^3/mol)$	$K_{T,0}(GPa)$	$K'_{T,0}$
Fe_5Si_3 (this study)	6.46	56.29	167(8)	5.1(2)
Fe_5Si_3 (Errandonea et al., 2008)	6.45	56.35	215(14)	3.6(6)
Fe_5Si_3 (Santamarıa-Pérez et al., 2004)	6.45	56.35	249(9)	3.4(9)
Fe (Boehler et al., 2008)	8.26	56.35	161(6)	5.6(2)
Fe (Dewaele et al., 2006)	8.27	6.76	163(8)	5.38(16)
Fe (Brown and McQueen, 1986)	7.85	7.11	172(3)	5.14(7)

Table 4.1: Pressure-Volume equation of state parameters for iron-silicon compounds and alloys

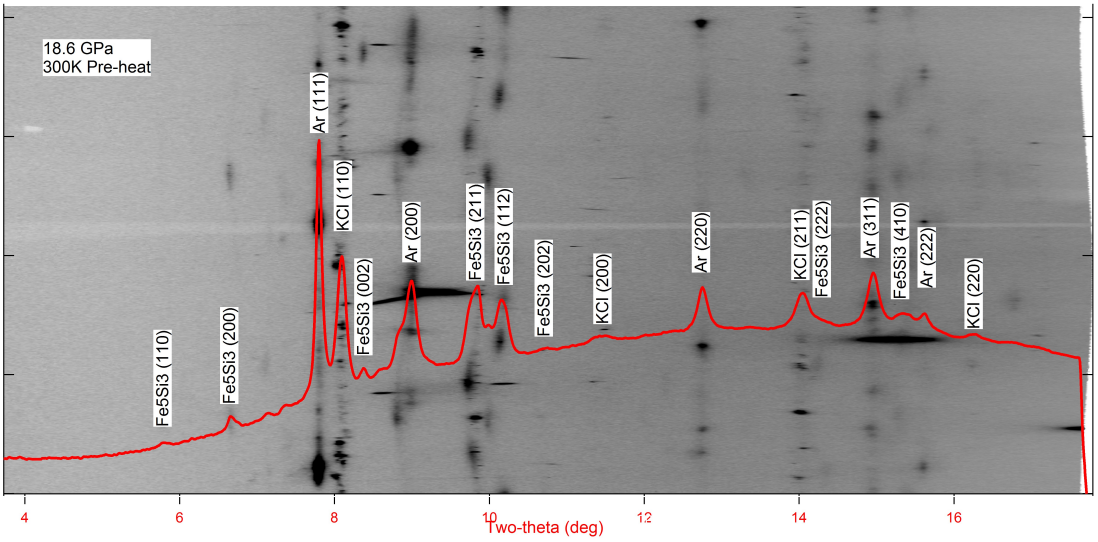

Figure 4.1: Diffraction patterns at 18 GPa are shown at room temperature, prior to heating.

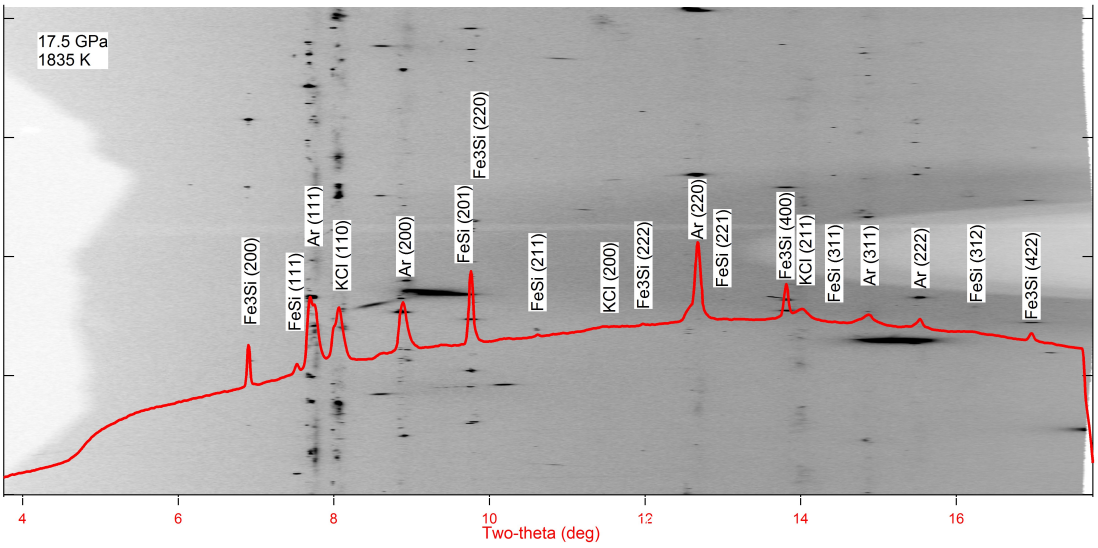

Figure 4.2: At high temperature, the Fe_5Si_3 diffraction lines are no longer present. Highly textured diffraction intensity corresponds well with Fe_3Si ($Fm3m, a = 5.548$Å), and FeSi ($P2_13, a = 4.405$Å). No elemental iron is observed in the high-temperature diffraction pattern.

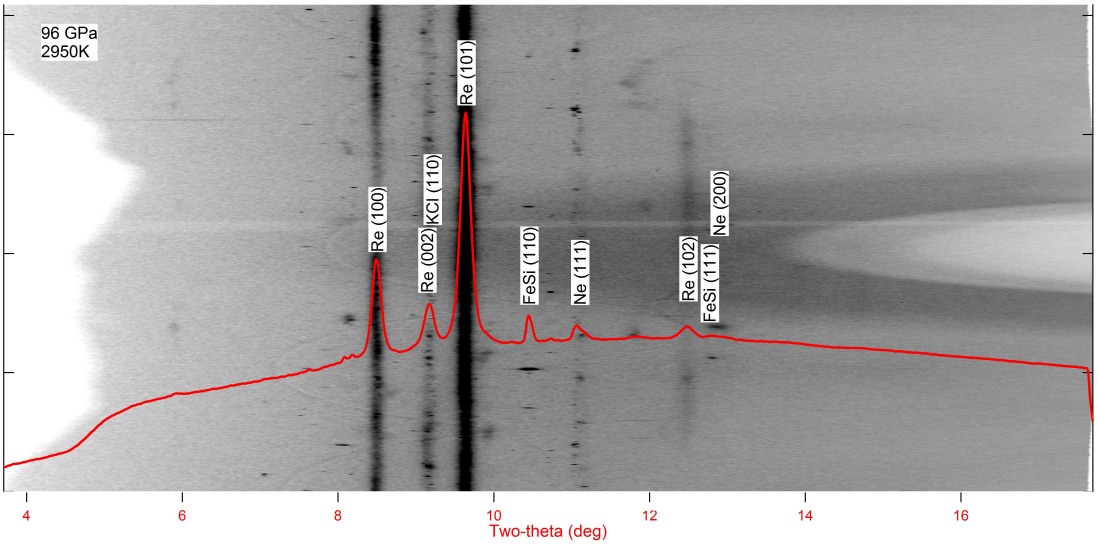

Figure 4.3: Diffraction pattern at 96 GPa and 2900 K shows that the B2 phase of FeSi is present, but Fe_5Si_3 is not. Another, larger unit cell material is also present but could not be identified unequivocally. Re is present in this diffraction pattern, since the sample was close to the gasket edge.

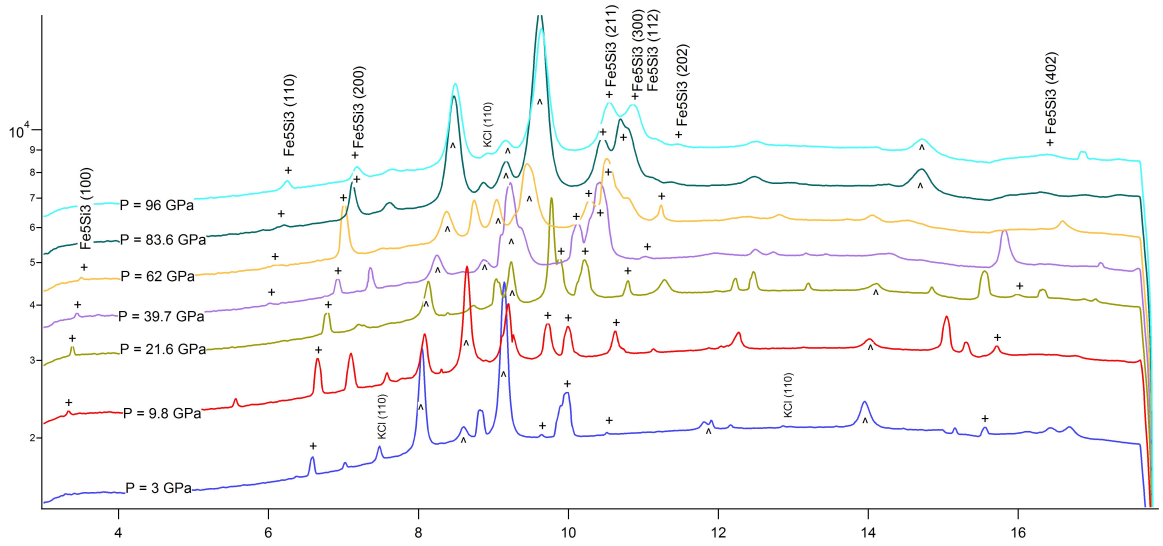

Figure 4.4: Room temperature diffraction patterns of Fe_5Si_3. The Fe_5Si_3 peaks used to calculate unit cell volume are labeled with their miller indices.

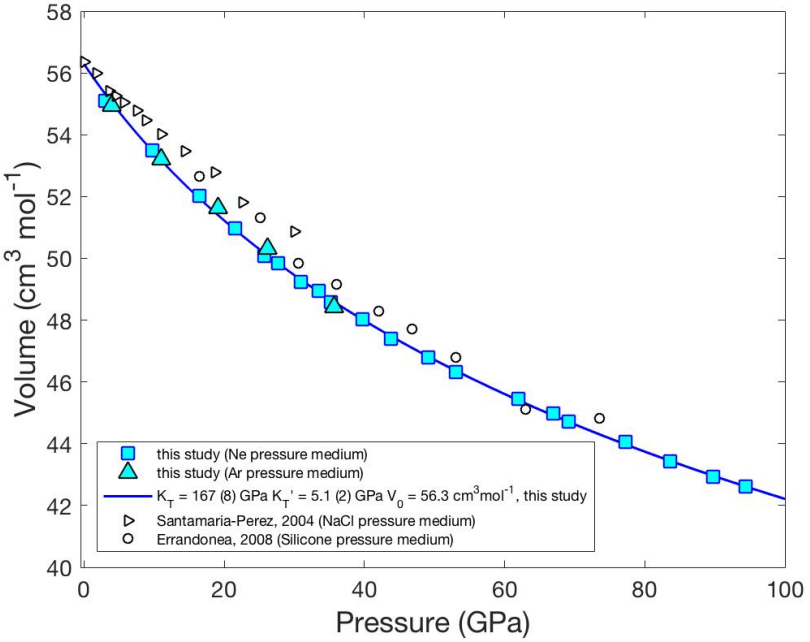

Figure 4.5: Volume versus pressure data for Fe_5Si_3. Solid line shows the best fit Birch-Murnaghan isothermal equation of state through the data. Error bars are smaller than marker size.

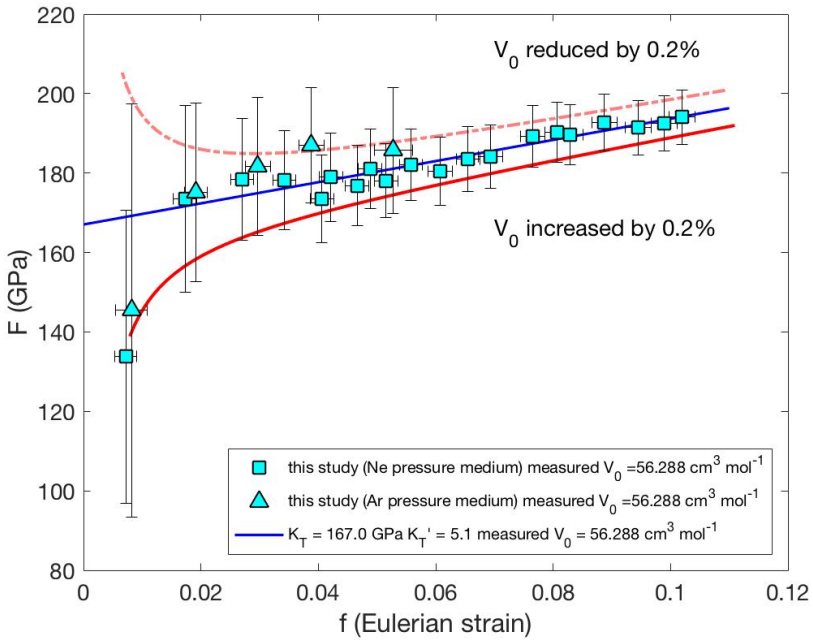

Figure 4.6: Normalized pressure (F) plotted versus Eulerian strain (f) with uncertainty in pressure and Eulerian strain propagated according to propagation of errors (Heinz and Jeanloz, 1984). The best fit equation of state parameters from the nonlinear fit of the pressure-volume data in Figure 4.5 are plotted as the blue line. Red lines above and below show the effect of perturbing the V_0 by 0.2%.

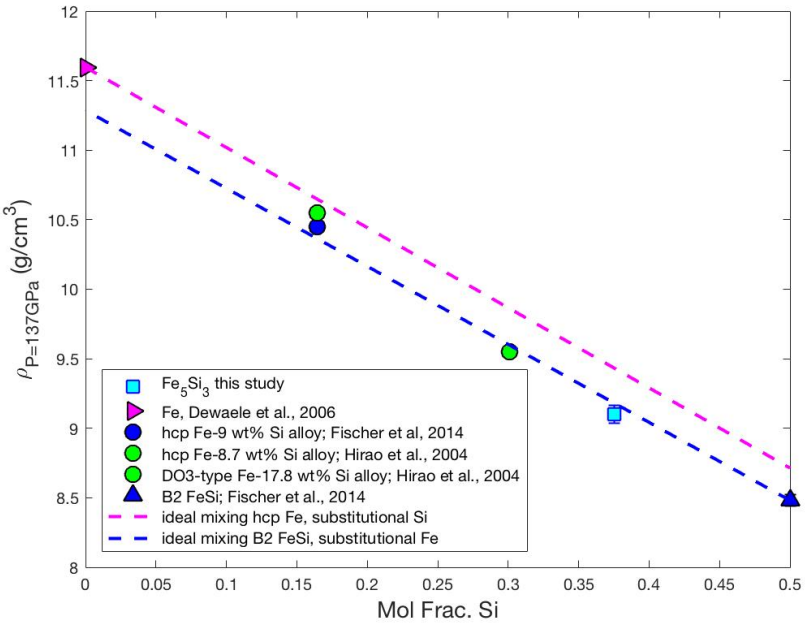

Figure 4.7: Density of solids in the Fe-FeSi system at 137 GPa calculated from equations of state for each material. Error bars are calculated using a Monte Carlo scheme which incorporates reported Birch-Murnaghan EOS parameter errors. The trend suggests linear changes in density, independent of structure, for increasing mole fraction of silicon. A hypothetical ideal mixing of hcp iron with substitutional silicon is shown with dashed line.

Bibliography

Allègre, C., Manhès, G., Lewin, É., 2001. Chemical composition of the earth and the volatility control on planetary genetics. Earth and Planetary Science Letters 185, 49–69.

Antonangeli, D., Siebert, J., Badro, J., Farber, D.L., Fiquet, G., Morard, G., Ryerson, F.J., 2010. Composition of the earth's inner core from high-pressure sound velocity measurements in fe–ni–si alloys. Earth and Planetary Science Letters 295, 292–296.

Badro, J., Fiquet, G., Guyot, F., Gregoryanz, E., Occelli, F., Antonangeli, D., d'Astuto, M., 2007. Effect of light elements on the sound velocities in solid iron: implications for the composition of earth's core. Earth and Planetary Science Letters 254, 233–238.

Boehler, R., Santamaría-Pérez, D., Errandonea, D., Mezouar, M., 2008. Melting, density, and anisotropy of iron at core conditions: New x-ray measurements to 150 gpa, in: Journal of Physics: Conference Series, IOP Publishing. p. 022018.

Brandes, E.A., Brook, G., 2013. Smithells metals reference book. Elsevier.

Brosh, E., Makov, G., Shneck, R.Z., 2009. Thermodynamic analysis of high-pressure phase equilibria in fe–si alloys, implications for the inner-core. Physics of the Earth and Planetary Interiors 172, 289–298.

Brown, J.M., McQueen, R.G., 1986. Phase transitions, grüneisen parameter, and elasticity for shocked iron between 77 gpa and 400 gpa. Journal of Geophysical Research: Solid Earth 91, 7485–7494.

Caracas, R., 2016. Crystal structures of core materials. Deep Earth: Physics and Chemistry of the Lower Mantle and Core 217, 57.

Dewaele, A., Datchi, F., Loubeyre, P., Mezouar, M., 2008. High pressure–high temperature equations of state of neon and diamond. Physical Review B 77, 094106.

Dewaele, A., Loubeyre, P., Occelli, F., Mezouar, M., Dorogokupets, P.I., Torrent, M., 2006. Quasihydrostatic equation of state of iron above 2 mbar. Physical Review Letters 97, 215504.

Dobson, D.P., Vocadlo, L., Wood, I.G., 2002. A new high-pressure phase of fesi. American mineralogist 87, 784–787.

Errandonea, D., Santamaría-Perez, D., Vegas, A., Nuss, J., Jansen, M., Rodríguez-Hernandez, P., Muñoz, A., 2008. Structural stability of fe 5 si 3 and ni 2 si studied by high-pressure x-ray diffraction and ab initio total-energy calculations. Physical Review B 77, 094113.

Fischer, R.A., Campbell, A.J., Caracas, R., Reaman, D.M., Dera, P., Prakapenka, V.B., 2012. Equation of state and phase diagram of fe–16si alloy as a candidate component of earth's core. Earth and Planetary Science Letters 357, 268–276.

Fischer, R.A., Campbell, A.J., Caracas, R., Reaman, D.M., Heinz, D.L., Dera, P., Prakapenka, V.B., 2014. Equations of state in the fe-fesi system at high pressures and temperatures. Journal of Geophysical Research: Solid Earth 119, 2810–2827.

Fischer, R.A., Campbell, A.J., Reaman, D.M., Miller, N.A., Heinz, D.L., Dera, P., Prakapenka, V.B., 2013. Phase relations in the fe–fesi system at high pressures and temperatures. Earth and Planetary Science Letters 373, 54–64.

Geballe, Z.M., Jeanloz, R., 2014. Solid phases of fesi to 47 gpa and 2800 k: New data. American Mineralogist 99, 720–723.

Heinz, D.L., Jeanloz, R., 1984. The equation of state of the gold calibration standard. Journal of Applied Physics 55, 885–893.

Hirao, N., Ohtani, E., Kondo, T., Kikegawa, T., 2004. Equation of state of iron–silicon alloys to megabar pressure. Physics and chemistry of minerals 31, 329–336.

Kinsland, G.L., Bassett, W.A., 1976. Modification of the diamond cell for measuring strain and the strength of materials at pressures up to 300 kilobar. Review of Scientific Instruments 47, 130–133.

de Koker, N., Steinle-Neumann, G., Vlček, V., 2012. Electrical resistivity and thermal conductivity of liquid fe alloys at high p and t, and heat flux in earths core. Proceedings of the National Academy of Sciences 109, 4070–4073.

Kraus, W., Nolze, G., 1998. Powdercell 2.0 for windows. J. Powder Diffraction 13, 256–259.

Kuwayama, Y., Hirose, K., Sata, N., Ohishi, Y., 2008. Phase relations of iron and iron–nickel alloys up to 300 gpa: Implications for composition and structure of the earth's inner core. Earth and Planetary Science Letters 273, 379–385.

Lin, J.F., Campbell, A.J., Heinz, D.L., Shen, G., 2003. Static compression of iron-silicon alloys: Implications for silicon in the earth's core. Journal of Geophysical Research: Solid Earth 108.

Lin, J.F., Heinz, D.L., Campbell, A.J., Devine, J.M., Shen, G., 2002. Iron-silicon alloy in earth's core? Science 295, 313–315.

Lin, J.F., Scott, H.P., Fischer, R.A., Chang, Y.Y., Kantor, I., Prakapenka, V.B., 2009. Phase relations of fe-si alloy in earth's core. Geophysical Research Letters 36.

Mao, H., Xu, J.A., Bell, P., 1986. Calibration of the ruby pressure gauge to 800 kbar under quasi-hydrostatic conditions. Journal of Geophysical Research: Solid Earth 91, 4673–4676.

Poirier, J.P., 1994. Light elements in the earth's outer core: a critical review. Physics of the earth and planetary interiors 85, 319–337.

Pozzo, M., Davies, C., Gubbins, D., Alfe, D., 2012. Thermal and electrical conductivity of iron at earths core conditions. Nature 485, 355.

Prakapenka, V., Kubo, A., Kuznetsov, A., Laskin, A., Shkurikhin, O., Dera, P., Rivers, M., Sutton, S., 2008. Advanced flat top laser heating system for high pressure research at gsecars: application to the melting behavior of germanium. High Pressure Research 28, 225–235.

Prescher, C., Prakapenka, V.B., 2015. Dioptas: a program for reduction of two-dimensional x-ray diffraction data and data exploration. High Pressure Research 35, 223–230.

Ringwood, 1977. Composition of the core and implications for origin of the earth. Geochemical Journal 11, 111–135.

Rodríguez-Carvajal, J., 1993. Recent advances in magnetic structure determination by neutron powder diffraction. Physica B: Condensed Matter 192, 55–69.

Santamaría-Pérez, D., Boehler, R., 2008. Fesi melting curve up to 70 gpa. Earth and Planetary Science Letters 265, 743–747.

Santamarıa-Pérez, D., Nuss, J., Haines, J., Jansen, M., Vegas, A., 2004. Iron silicides and their corresponding oxides: a high-pressure study of fe5si3. Solid state sciences 6, 673–678.

Shen, Y., Kumar, R.S., Pravica, M., Nicol, M.F., 2004. Characteristics of silicone fluid as a pressure transmitting medium in diamond anvil cells. Review of scientific instruments 75, 4450–4454.

Tateno, S., Kuwayama, Y., Hirose, K., Ohishi, Y., 2015. The structure of fe–si alloy in earth's inner core. Earth and Planetary Science Letters 418, 11–19.

Unterborn, C.T., Dismukes, E.E., Panero, W.R., 2016. Scaling the earth: a sensitivity analysis of terrestrial exoplanetary interior models. The Astrophysical Journal 819, 32.

Vočadlo, L., 2015. Earth's core: Iron and iron alloys .

Walker, D., Cranswick, L.M., Verma, P.K., Clark, S.M., Buhre, S., 2002. Thermal equations of state for b1 and b2 kcl. American Mineralogist 87, 805–812.

Wolf, A.S., Jackson, J.M., Dera, P., Prakapenka, V.B., 2015. The thermal equation of state of (mg, fe) sio3 bridgmanite (perovskite) and implications for lower mantle structures. Journal of Geophysical Research: Solid Earth 120, 7460–7489.

Zhang, F., Oganov, A.R., 2010. Iron silicides at pressures of the earth's inner core. Geophysical Research Letters 37.

CHAPTER 5

Evidence for non-linear sediment transport on terrace riser hillslopes, South Island, New Zealand

5.1 Introduction

The movement of granular material in the landscape has been recognized as a diffusive transport process for over a century (Davis, 1892; Gilbert, 1909). However, the applicability of the diffusion equation to specific morphology and processes has been debated for nearly as long (Pierce and Colman, 1986; Tucker and Bradley, 2010). Two key assumptions are made in the derivation of the diffusion equation for sediment transport. First, the sediment flux per unit length, q_s, must be proportional to the gradient of the hillslope. Symbolically, this statement can be written for 2 dimensions:

$$q_s = -\kappa \nabla z \tag{5.1}$$

where κ is diffusivity $\left[L^2/T\right]$ that characterizes the magnitude and frequency of disturbances, z is elevation $\left[L\right]$, and the negative sign is convention so that the downslope direction is positive. The slope-dependent transport processes include rain splash, creep, and bioturbation (Culling, 1963; Carson and Kirkby, 1972). The second assumption is a conservation of mass statement:

$$\frac{\partial z}{\partial t} = \nabla q_s \tag{5.2}$$

Combining equations 1 and 2 gives the linear diffusion equation:

$$\frac{\partial z}{\partial t} = -\kappa \nabla^2 z \tag{5.3}$$

where change in elevation is dependent on the curvature of landscapes. The linear diffusion equation has been used to model the degradation of geomorphic surfaces of fault scarps and marine and stream terrace risers (Rosenbloom and Anderson, 1994; Martin, 2000; Hilley and Arrowsmith, 2008; Wei et al., 2015). The morphologic age of hillslope scarps derived from linear diffusion can be applied to a variety of problems, including studies of active fault slip rates and spatio-temporal deformation patterns (Avouac, 1993; Hilley et al., 2010).

Despite the wide applicability of linear diffusion in describing landscape morphology, previous studies suggest that linear diffusion may not accurately capture hillslope degradation processes in certain cases (Pierce and Colman, 1986; Roering et al., 1999; Heimsath et al., 2005; Tucker and Bradley, 2010). A nonlinear formulation of the sediment flux, given by:

$$q_s = -\frac{\kappa \nabla z}{(1 - \frac{|\nabla z|}{S_c})^2} \tag{5.4}$$

where S_c is a critical slope, which is formally defined by the shear strength of the sediment (Roering et al., 1999). If S_c is very large, the nonlinear sediment flux in Eq. 5.4 approaches the linear flux in Eq. 5.1. However, for S_c values approaching landscape slopes, the linear and nonlinear sediment fluxes can be significantly different.

Pierce and Colman (1986) suggest the importance of nonlinear transport based on observations of a height dependence of terrace riser hillslope diffusivity. Other work has argued that the height dependence may be due to the use of the maximum hillslope gradient, rather than the full profile, to determine diffusivity (Pelletier et al., 2006). However, a statistically significant height dependence of terrace riser hillslope diffusivity has also been found in other

studies, using full profile diffusion modeling (Clarke and Burbank, 2010). Assessing the importance of linear or nonlinear diffusion process in degradation of scarp and terrace risers is often complicated by the unknown age of the geomorphic features and by limited terrace sampling at a single field site (Clarke and Burbank, 2010). In this study, we examine the profiles for a fleet of six terrace risers, on South Island, New Zealand, using models of linear and nonlinear diffusion. The ages of terrace risers are constrained by infra-red stimulated luminescence (IRSL) ages of feldspar sand grains sampled from the terrace treads. We find that though the linear diffusion model produces a strong height dependence of terrace riser hillslope diffusivity, nonlinear models produce much less height dependence of slope diffusivity. This observation suggests that nonlinear transport plays an important role in degrading fluvual terrace risers.

5.2 Field Site

The field site is a fleet of six terraces, located on South Island, New Zealand. The terrace treads are progressively offset by the Awatere Fault, a dextral 150 km long fault strand of the Marlborough Fault System (MFS) (Mason et al., 2006; Zinke et al., 2015). The terraces are located at the confluence of the Saxton River and the Awatere River, and are incised into valley wide last-glacial maximum age alluvial fill (Lensen, 1973; Knuepfer, 1992; Mason et al., 2006; Zinke et al., 2017). There are six terraces above the modern river, labelled T1-T6, from oldest to youngest. The terrace fleet at Saxton River is shown in Figure 5.1. The terraces are comprised of coarse gravel with interstitial sand and sparse sand lenses. Terrace treads are capped with fine grained loess, approximately 10 cm to 50 cm thick, and a soil horizon, approximately 5-15 cm thick. The loess deposits are not necessarily syn-depositional with the terrace gravels. The terrace riser is defined as the scarp between terrace treads. After incision and terrace tread abandonment, the risers will degrade over time.

5.3 Data Collection and Analysis

High resolution topography data was collected by aircraft in collaboration with the National Center for Airborne Laser Mapping (NCALM). The data processed by NCALM produce a digital elevation model (DEM) with a pixel resolution of 0.33 m with an areal coverage of 305 km^2. Ages of the terraces were determined using infra-red stimulated luminescence (IRSL) of potassium-rich feldspar sand grains (175 μm to 200 μm diameter). IRSL dates the time elapsed since sediment last was exposed to light. K-feldspar is suitable for sediment dating using infra-red stimulated luminescence (IRSL) because of the bright (high photon count) luminescence signal and ubiquitous distribution in the landscape (Rhodes, 2015). A potential drawback of using K-feldspar is signal fading over the timescale of interest. This problem is mitigated using the pIR-IRSL method, modified for single-grain dating (Buylaert et al., 2009; Rhodes, 2015). Ages are determined by luminescence single grain pIR-IRSL for a series of samples from each terrace tread gravel deposit. The ages are input into a Bayesian stratigraphic model, using OxCal. The details of the age model are described elsewhere (Zinke et al., 2017).

The terrace treads are labeled T1-T6, in order of oldest to youngest, following Mason et al. (2006) and Zinke et al. (2017). The terrace riser is defined as the scarp between two terrace treads, and is denoted, for example, as T1/T2. The terrace riser data was collected using one-dimensional profiles extracted from the DEM along steepest descent. We collected profiles from the T1/T2, T2/T3, T2/T5, and T4/T5 terrace risers. Profiles which had a channel intersecting the terrace tread and the riser, which could complicate modeling, were eliminated prior to analysis. A total of 20 risers were analyzed. The one dimensional profiles

were drawn from locations indicated by hatch marks shown on Figure 5.1. The initiation of terrace degradation is given by the abandonment age of the lower terrace tread, when river flow no longer undercuts the base of the terrace riser. This age is assigned as the luminescence-derived age of the lower terrace.

Analysis of hillslope profiles derived from the DEM can sometimes suffer from noisy data that can bias misfit between data and models (Clarke and Burbank, 2010). In order to mitigate this problem, the data was smoothed by convolution, with an averaging filter of 1.65 m (e.g. 5-cell) in length. The gradient of the raw data and smoothed data of an example profile across the T4/T5 terrace riser is shown in Figure 5.2. The gradient of the smoothed data is used to locate the inflection point of the terrace and construct an initial terrace riser profile.

Using the initial profiles of terrace risers, we model the degradation of terraces using linear and nonlinear models. The linear diffusion equation can be solved numerically or analytically, for certain initial and boundary conditions. The nonlinear diffusion, equation, however, can only be solved analytically in special cases, and for a restricted set of flux laws. We use numerical solvers to forward model both linear and nonlinear diffusion. The numerical models are benchmarked to an analytical solution for linear diffusion. The analytical solution for 1-D diffusion of a terrace riser is given by (Hanks and Andrews, 1989):

$$\begin{aligned} h(x,t) = \theta\sqrt{\frac{\kappa t}{\pi}}\Big[exp(-\frac{(x+\frac{a}{\theta})^2}{4\kappa t}) - exp(-\frac{(x-\frac{a}{\theta})^2}{4\kappa t})\Big] \\ + \frac{\theta}{2}\Big[(x+\frac{a}{\theta})erf(\frac{x+\frac{a}{\theta}}{\sqrt{4\kappa t}}) - (x-\frac{a}{\theta})erf(\frac{x-\frac{a}{\theta}}{\sqrt{4\kappa t}})\Big] \end{aligned} \tag{5.5}$$

where θ is the initial gradient, a is half the height of the terrace riser, κ is the diffusivity, and t is time. Linear diffusion is solved numerically by finite difference method, using forward-time, centered-space (FTCS). The nonlinear diffusion equation is solved using an implicit method, following Perron (2011). The nonlinear numerical model is also benchmarked to

the analytical solution, under the condition that the nonlinear sediment flux approaches the linear flux in Eq. 5.1. This occurs where $|\nabla z| << S_c$ so that the denominator in Eq. 5.6 is close to 1 (Fig. 5.3). Both the linear and nonlinear numerical models successfully recover diffusivities of synthetic riser profiles generated by the analytical diffusion equation.

The initial scarp slope is determined from terrace riser profiles that intersect the modern river, shown in black lines in Fig. 5.1. The risers have a mean slope of $36° \pm 2°$, which is taken to be the angle of repose. An initial profile with $\theta_0 = 36°$ is run forward in time, using the linear or nonlinear numerical diffusion model, for the age of the lower terrace. Misfit between model and data are calculated from the gradient of forward model outputs for the full terrace riser profile. The model outputs from a grid of κ values (and S_c values for the nonlinear model) are compared with each full terrace riser pofile and the misfit is calculated by the root mean square error (RMS). The method of RMS calculation is by the gradient of the model and data, following Wei et al. (2015).:

$$RMS = \left(\frac{1}{n} \sum_{i=1}^{n} \left[\nabla z_i - \nabla z_{model}(x_i) \right]^2 \right)^{\frac{1}{2}} \tag{5.6}$$

where ∇z_i is the riser gradient of the data, and $\nabla z_{model}(x_i)$ is the numerical model output gradient, evaluated at x_i. The minimum RMS value for each terrace riser defines the best fit κ and S_c value for that terrace riser profile. The error in κ is given by the RMS minimum value $+1\sigma$, which is defined by the resolution of the DEM as 5cm.

5.4 Results

The results for hillslope diffusivity, given linear diffusion of terraces of different ages, are shown in Figure 5.4. There is a strong height dependence of κ for linear diffusion. The height dependence persists for a terrace riser intersecting the same lower terrace, but with a

variation in height along the scarp, as evidenced by risers that intersect 4.3 ka T5 tread (Fig 5.4). In other words, a change in κ through time, with the linear diffusion equation, cannot explain the height dependence in the data set. The nonlinear model was run over a series of critical slope S_c values and κ values. The minimum misfit between model and data at each S_c value is calculated for a range of κ values. With decreasing critical slopes, the height dependence of diffusivity is significantly reduced. For $S_c = 0.8$, the diffusivity approaches a constant value, as shown in Fig. 5.4.

5.5 Discussion

The use of luminescence dates of terrace treads allows the determination of κ for nonlinear and linear models across a range of terrace ages and heights. The dates of terrace material derived from luminescence ages are depositional, so they do not strictly date the abandonment. However, geomorphic analysis of terrace tread fluvial features offset by the Awatere fault demonstrate that the lower terrace age marks the beginning of slip accrual (Cowgill, 2007; Zinke et al., 2017). This corroborating evidence from a slip rate study at this site (Zinke et al., 2015) supports lower terrace ages to represent initiation of terrace riser degradation, since the Awatere fault exposes the offset riser edge directly to the flow of the Saxton River, making preservation prior to abandonment unlikely (Zinke et al., 2017).

A height dependence of κ for linear diffusion of terrace scarps has been observed before at multiple field sites, and in different climates (Pierce and Colman, 1986; Clarke and Burbank, 2010). Several physical mechanisms can account for height dependence of κ. One possibility is that there is advection of material, due to small channels, called rills, forming on the terrace scarp (Pierce and Colman, 1986). Rills may become more significant with larger scarps.

A second possibility is that grain cascading occurs (Tucker and Bradley, 2010). This process involves rare departures from slope dependent mass flux that can disturb additional grains down slope. The further the grains can fall, the more significant these cascades become, leading to greater mass transport with height of the scarp. These processes involve some violation of linear diffusion since the mass flux does not scale linearly with slope.

The nonlinear diffusion model produces a reduced height dependence of κ as S_c approaches the angle of repose gradient, in contrast to the linear diffusion results. At values of S_c below 0.9, the height dependence approaches the error bounds on the nonlinear diffusivity. This suggests that a general hillslope diffusivity and critical slope can explain the degradation of terrace riser form at this field site, over the height (2 to 12 m) and age (4.2 to 7.2 Ka) range sampled. This highlights the importance of the nonlinear transport to explain the degraded topographic profiles in fluvial terrace risers.

5.6 Conclusion

We applied hillslope diffusion models to a fleet of six terrace risers with varying heights and ages. Our results show a strong height dependence of κ for linear diffusion models of terrace risers that are the same age. However, the nonlinear diffusion equation for sediment flux can remove the height dependence of κ. Using a best fit for the entire data set, for all heights and ages, we calculate $\kappa = 1.9 \pm 0.7 * 10^{-3} m^2/yr$ with $S_c = 0.80$ for the terrace riser fleet. The ability to describe the terrace riser elevation data set with a single κ value suggests that nonlinear diffusion plays an important role in degrading slopes on fluvial terrace risers. The linear diffusion equation has limited predictive power of the age of terrace risers with steep slopes or a large range in heights, and should be used with caution when attempting to date the geomorphic surfaces in the landscape.

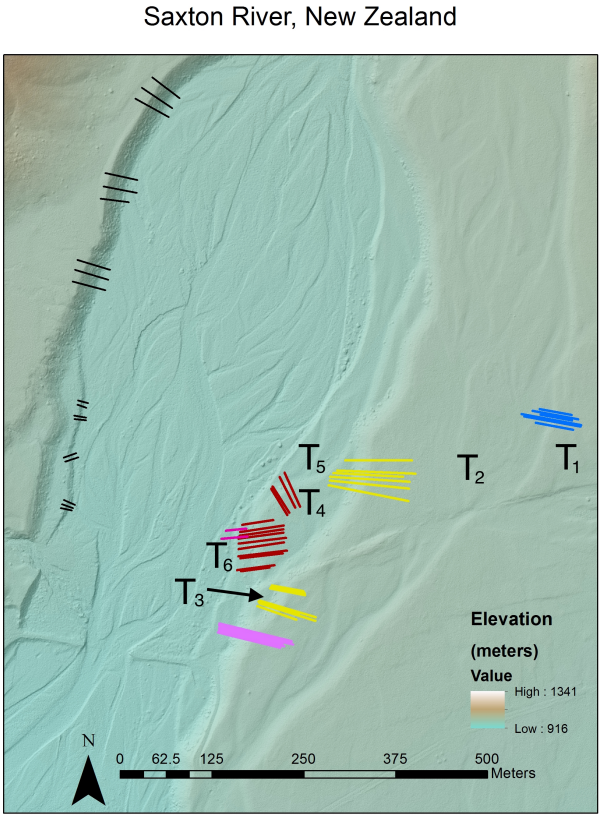

Figure 5.1: Saxton River terrace fleet with terraces labelled from oldest to youngest. Hatch marks indicate cross sections across terrace scarps. Black hatch marks indicate scarps that intersect the modern river.

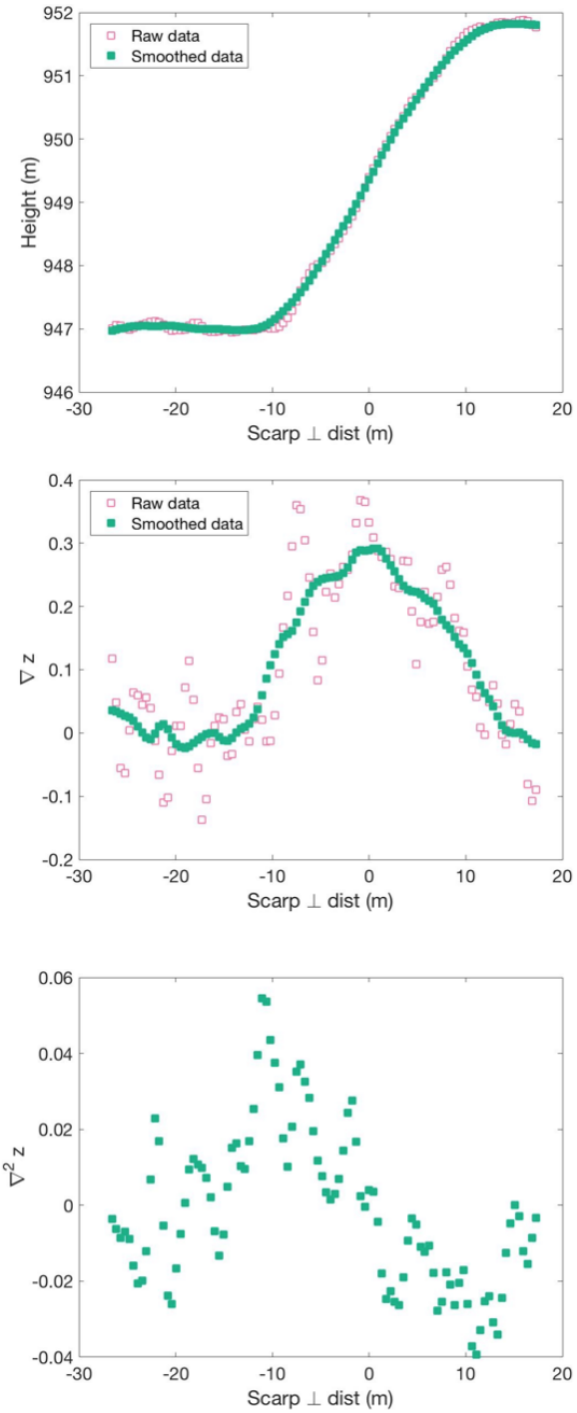

Figure 5.2: The T4/T5 terrace riser profile is shown for raw data (open squares) and smoothed data (filled squares) in the top panel. The gradient of the terrace riser is shown in the middle panel. The curvature is shown in the bottom panel.

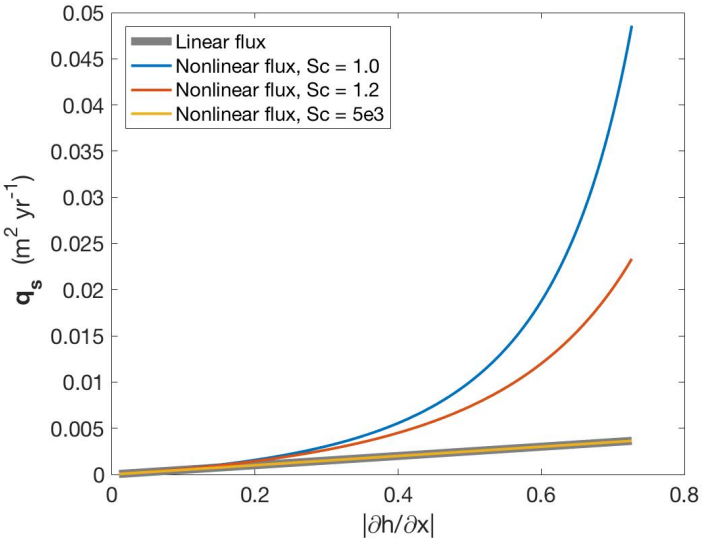

Figure 5.3: The sediment flux as a function of hillslope gradient for linear (Eq. 5.1) and nonlinear (Eq. 5.6) transport laws is shown, with different critical slopes (Sc) for the nonlinear model.

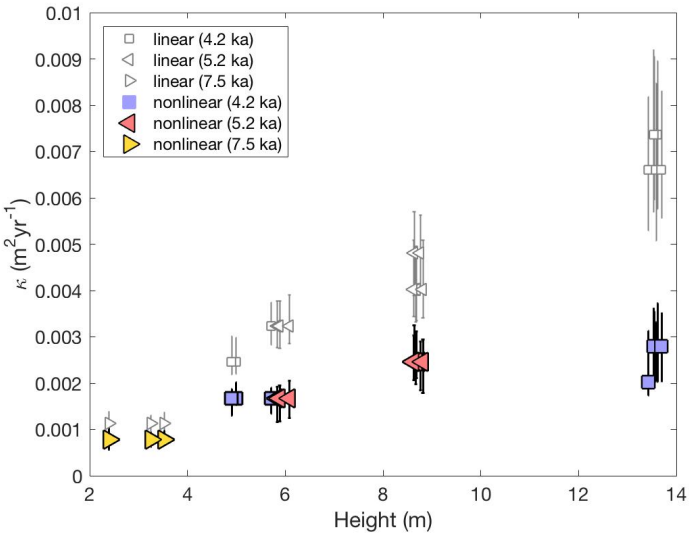

Figure 5.4: The diffusivity is shown for a series of terraces, of different ages and heights for linear and nonlinear numerical models, determined by minimizing RMS between the DEM profile and the models.

Bibliography

Avouac, J.P., 1993. Analysis of scarp profiles: evaluation of errors in morphologic dating. Journal of Geophysical Research: Solid Earth 98, 6745–6754.

Buylaert, J.P., Murray, A.S., Thomsen, K.J., Jain, M., 2009. Testing the potential of an elevated temperature irsl signal from k-feldspar. Radiation Measurements 44, 560–565.

Carson, M.A., Kirkby, M.J., 1972. Hillslope form and process. University press.

Clarke, B.A., Burbank, D.W., 2010. Evaluating hillslope diffusion and terrace riser degradation in new zealand and idaho. Journal of Geophysical Research: Earth Surface 115.

Cowgill, E., 2007. Impact of riser reconstructions on estimation of secular variation in rates of strike–slip faulting: Revisiting the cherchen river site along the altyn tagh fault, nw china. Earth and Planetary Science Letters 254, 239–255.

Culling, W., 1963. Soil creep and the development of hillside slopes. The Journal of Geology 71, 127–161.

Davis, W., 1892. The convex profile of bad-land divides. Science , 245–245.

Gilbert, G.K., 1909. The convexity of hilltops. The Journal of Geology 17, 344–350.

Hanks, T.C., Andrews, D., 1989. Effect of far-field slope on morphologic dating of scarplike landforms. Journal of Geophysical Research: Solid Earth 94, 565–573.

Heimsath, A.M., Furbish, D.J., Dietrich, W.E., 2005. The illusion of diffusion: Field evidence for depth-dependent sediment transport. Geology 33, 949–952.

Hilley, G., DeLong, S., Prentice, C., Blisniuk, K., Arrowsmith, J., 2010. Morphologic dating of fault scarps using airborne laser swath mapping (alsm) data. Geophysical Research Letters 37.

Hilley, G.E., Arrowsmith, J.R., 2008. Geomorphic response to uplift along the dragon's back pressure ridge, carrizo plain, california. Geology 36, 367–370.

Knuepfer, P.L., 1992. Temporal variations in latest quaternary slip across the australian-pacific plate boundary, northeastern south island, new zealand. Tectonics 11, 449–464.

Lensen, G., 1973. Guidebook for excursion a10, in: International Union for Quaternary Research Congress: Christchurch, New Zealand, 9th Congress, Field Trip Guide.

Martin, Y., 2000. Modelling hillslope evolution: linear and nonlinear transport relations. Geomorphology 34, 1–21.

Mason, D.P., Little, T.A., Van Dissen, R.J., 2006. Rates of active faulting during late quaternary fluvial terrace formation at saxton river, awatere fault, new zealand. Geological Society of America Bulletin 118, 1431–1446.

Pelletier, J.D., DeLong, S., Al-Suwaidi, A., Cline, M., Lewis, Y., Psillas, J., Yanites, B., 2006. Evolution of the bonneville shoreline scarp in west-central utah: Comparison of scarp-analysis methods and implications for the diffusion model of hillslope evolution. Geomorphology 74, 257–270.

Perron, J.T., 2011. Numerical methods for nonlinear hillslope transport laws. Journal of Geophysical Research: Earth Surface 116.

Pierce, K.L., Colman, S.M., 1986. Effect of height and orientation (microclimate) on geomorphic degradation rates and processes, late-glacial terrace scarps in central idaho. Geological Society of America Bulletin 97, 869–885.

Rhodes, E.J., 2015. Dating sediments using potassium feldspar single-grain irsl: initial methodological considerations. Quaternary International 362, 14–22.

Roering, J.J., Kirchner, J.W., Dietrich, W.E., 1999. Evidence for nonlinear, diffusive sediment transport on hillslopes and implications for landscape morphology. Water Resources Research 35, 853–870.

Rosenbloom, N.A., Anderson, R.S., 1994. Hillslope and channel evolution in a marine terraced landscape, santa cruz, california. Journal of Geophysical Research: Solid Earth 99, 14013–14029.

Tucker, G.E., Bradley, D.N., 2010. Trouble with diffusion: Reassessing hillslope erosion laws with a particle-based model. Journal of Geophysical Research: Earth Surface 115.

Wei, Z., Arrowsmith, J.R., He, H., 2015. Evaluating fluvial terrace riser degradation using lidar-derived topography: An example from the northern tian shan, china. Journal of Asian Earth Sciences 105, 430–442.

Zinke, R., Dolan, J.F., Rhodes, E.J., Van Dissen, R., McGuire, C.P., 2017. Highly variable latest pleistocene-holocene incremental slip rates on the awatere fault at saxton river, south island, new zealand, revealed by lidar mapping and luminescence dating. Geophysical Research Letters 44.

Zinke, R., Dolan, J.F., Van Dissen, R., Grenader, J.R., Rhodes, E.J., McGuire, C.P., Langridge, R.M., Nicol, A., Hatem, A.E., 2015. Evolution and progressive geomorphic manifestation of surface faulting: A comparison of the wairau and awatere faults, south island, new zealand. Geology 43, 1019–1022.

CHAPTER 6

Conclusion

6.1 Overview

The thermal conductivity of minerals across phase transitions has important implications for the thermal evolution of the interior of Earth. We have shown that (Mg,Fe)O exhibits an anomalous lattice thermal conductivity decrease with pressure in the mixed spin state. The lattice thermal conductivity decreases between 42 and 61 GPa, which can be attributed to a reduction in bulk sound speed, due to the mixed spin state of iron in an octahedral coordination environment. This decrease could produce an unusual depth profile of thermal conductivity through the Earth's mantle. Furthermore, some fraction of high spin state iron may persist all the way to the core-mantle boundary, making the mixed spin state of ferropericlase important for CMB heat flow (Holmström and Stixrude, 2015).

The thermal conductivity results from Chapter 3 can be extended throughout the lower mantle, using a simplified model, which I describe here. Extension to high pressure and temperature conditions is complicated by the broadening of the P-T phase space occupied the mixed spin state (Tsuchiya et al., 2006; Mao et al., 2011; Holmström and Stixrude, 2015). Figure 6.1 shows the pressure and temperature conditions of this work and others, plotted over the ab initio spin fraction phase diagram of (Holmström and Stixrude, 2015). Presently, it is not possible to make measurements *in situ* of thermal conductivity at the core-mantle

boundary pressure and temperature conditions.

6.2 Spin state model

In order to extrapolate our measurements, I make three general assumptions. First, taking the phase diagram of (Holmström and Stixrude, 2015), I estimate the high spin state fraction along the geothermal profile (Wolf et al., 2015), the results of which are shown in Figure 6.2. Second, I assume that the minimum in mixed spin thermal conductivity is associated with the minimum in bulk sound speed, as was done in Chapter 3. Lastly, I assign the minimum bulk sound speed as the mean of a normal distribution, with a spin fraction of 0.5 mapped to the mean. Using this framework, a thermal conductivity reduction from a hypothetical purely high spin state can be assigned at each point along the pressure and temperature profile of the lower mantle, with the spin fractions from Figure 6.2. At each point, the thermal conductivity is calculated using a temperature dependence of $(T_0/T)^{0.5}$, and the results are shown in Figure 6.3. The reduction in thermal conductivity of ferropericlase is over a broad depth range in the lower mantle, due to the fact that the mixed spin phase is broad. A different calculated spin state phase diagram, such as that of (Tsuchiya et al., 2006), would result in a different depth dependence, but the general result of a broad reduced thermal conductivity profile is robust.

6.3 Mantle Radiative thermal conductivity

The thermal conductivity of mantle minerals is the sum of lattice, radiative and electrical components. So far in this dissertation, only the lattice component has been discussed, but

radiative thermal conductivity is important to consider in order to describe the thermal conductivity at mantle conditions, particularly in the core-mantle boundary region where temperatures rise significantly. Radiative heat transport by photons is important for optically thick dielectric materials at high temperatures. These conditions are met for the silicates and oxides of the lower mantle, but uncertainty exists in the value of radiative thermal conductivity of the major minerals (Rainey, 2014).

Radiative thermal conductivity at high pressure and temperature remains controversial for several reasons. First, there is a fundamental question of whether it is possible to measure absorption in the diamond anvil cell, even at room temperature, due to the limited volume of the sample (Hofmeister, 2014). Secondly, absorption properties could change at high temperatures. Recent experiments show a large increase in absorption at high temperature that could limit radiative heat transport at lower mantle conditions (Lobanov et al., 2017). The problem with measuring absorption is significant enough that calculations of the radiative component of thermal conductivity in the mantle vary by orders of magnitude, from low values of 0.5 W/mK to values as high as 10 W/mK (Goncharov et al., 2008; Keppler et al., 2008).

Absorption coefficient values depend on both the methods used for measurement and on sample iron content. The absorption coefficient for mantle oxides and silicates increases with iron content. To first order, then, the radiative conductivity should decrease with increasing iron content. Accordingly, ferropericlase should be lower than bridgmanite, due to the higher iron content of ferropericlase than bridgmanite (Mg# = 0.83 for ferropericlase, Mg# = 0.93 for bridgmanite) (Cottaar et al., 2014). I reproduce calculations of radiative thermal conductivity as a function of depth in the mantle given a set of absorption coefficient measurements with different iron contents (Goncharov et al., 2006, 2008).

The radiative contribution to thermal conductivity can be calculated by the Rosseland mean approximation. Inherent in this formulation is the assumption that the transport of heat by photons in the mantle is diffusive in nature, due to the optically thick conditions of the material (Hofmeister, 1999; Rainey, 2014). For these conditions, the radiative conductivity is given as:

$$k_{rad} = \frac{16n^2\sigma T^3}{3B_R} \tag{6.1}$$

where

$$\frac{n^2}{B_R} = \frac{\pi}{4\sigma T^3}\int_0^\infty \frac{n_2}{B_\lambda}\frac{dI_{b,y}}{dT}d\lambda \tag{6.2}$$

and where n_λ is the wavelength-dependent index of refraction, σ is the Stephan-Boltzman constant, B_λ is the extinction coefficient, and $I_{b,\lambda}$ is the blackbody radiation intensity (Keppler et al., 2008; Rainey, 2014). The blackbody intensity derivative, with respect to temperature, $\frac{dI_{b,\lambda}}{dT}$ is given by:

$$\frac{dI_{b,\lambda}}{dT} = \frac{2hc^2}{\lambda^5}\frac{hc}{\lambda k_B T^2}\frac{e^{\frac{hc}{\lambda k_B T}}}{\left(e^{\frac{hc}{\lambda k_B T}}-1\right)^2} \tag{6.3}$$

where $I_{b,\lambda}$ is the intensity, h is the Planck constant, c is the speed of light, λ is wavelength, and k_B is the Boltzmann constant. The temperature derivative intensity spectral dependence is evaluated at a series of wavelengths and shown in Figure 6.4. The spectral range shown here covers existing measurements of the absorption coefficient. While the integral is technically evaluated over [0, ∞], Figure 6.4 shows that the peak intensity falls off by orders for temperatures in the Earth's mantle outside the spectral data range. Therefore, we make the assumption that the spectral range shown in Figure 6.4 is sufficient for radiative conductivity calculations.

The extinction coefficient, B_R, is a summation over scattering and absorption terms, but only absorption is considered in Eq. 6.2. Ignoring scattering can be justified by assum-

ing that the mean free path of absorption is much smaller than the scattering length scale (Rainey, 2014). The wavelength dependent absorption coefficient has been measured for (Mg,Fe)O at a range for iron contents and pressures (Goncharov et al., 2006, 2008, 2010; Keppler et al., 2008).

The absorption coefficient data was chosen from two studies (Goncharov et al., 2006, 2008). These studies used the same techniques and equipment, and their results illustrate the dependence of κ_{rad} on iron. The third study demonstrates differences between measurement techniques. To calculate κ_{rad} through the mantle, the absorption coefficients were interpolated between measured pressures. The radiative conductivity was calculated along geothermal profile (Wolf et al., 2015) using Eq. 6.1, over the spectral range $[0.25, 3]\mu m$. In some cases, the absorption coefficient measurements do not extend over the lower end of the proscribed spectral range, and a linear extrapolation of the data was applied.

The results of the K_{rad} are shown in Figure 6.6. In general, ferropericlase K_{rad} increases by about a factor of about 3 through the lower mantle. Reducing the iron content from atomic fraction x = 0.25 to x = 0.15 results in a radiative thermal conductivity that is twice as large. However, the contribution to the total thermal conductivity of ferropericlase is still likely small (about 10%), due to the high iron content of this mantle mineral (Mattern et al., 2005).

6.4 Mantle thermal conductivity depth dependence

The thermal conductivity of the lower mantle depends on the the depth profile of thermal conductivity of the major minerals ferropericlase and bridgmanite. The total thermal

conductivity of ferropericlase is shown in Figure 6.7. The lattice and radiative thermal conductivity of bridgmanite is calculated from measurements and modeling, using the same techniques (Rainey, 2014). A mixture model of the two minerals' thermal conductivity is carried out by two methods. The Voigt-Reuss-Hill model imagines a volumetric average between end members of the minerals arranged in series and in parallel. The Maxwell-garnet approximation imagines a volumetric average of a minor phase randomly included in a major phase. Both averaging schemes give similar results.

Pressure dependent thermal conductivity in the mantle could have profound implications for the style of mantle convection, the shape of plumes, and the stagnation of downwelling slabs (Tosi et al., 2013). A moderate increase in thermal conductivity with depth, as confirmed by the analysis in this chapter, would enhance slab stagnation at 660 km and limit the lateral extent of sources for plumes at the base of the mantle (Tosi et al., 2013). While the presence of a sharp reduction in thermal conductivity of ferropericlase will cause thermal conductivity to increase less rapidly in the lower mantle, the effect is likely minor due to the broadening of the spin transition phase space at high pressures and temperatures. This analysis suggests that thermal conductivity increases by a factor of about 2 from the top of the lower mantle to the core-mantle boundary. This result is consistent among different measurement techniques and mixture models (Ohta et al., 2017; Hsieh et al., 2018).

The reduction of thermal conductivity across the spin transition leads to a reduced total thermal conductivity in the CMB region. However, the effect is only modest on the total thermal conductivity because ferropericlase is 20% by volume. Accounting for the spin transition using the simple model described here reduces the CMB thermal conductivity from 5.5 W/mK to 5.2 W/mK, all other variables kept constant. There is uncertainty in the thermal conductivity temperature dependence for iron-bearing phases. The temperature dependence

of ferropericlase and Fe-bearing bridgmanite κ_{lat} at transition zone pressures was found to be m = 0.24 and 0.22, respectively (Manthilake et al., 2011). If these values are extrapolated to core-mantle boundary pressures, using our measured thermal conductivity pressure dependence, the CMB value doubles from 5.2 W/mK to 10.6 W/mK. This value could be thought of as an upper bound for the dataset presented here.

6.5 Core-mantle boundary heat flux

The globally averaged thermal conductivity of the core-mantle boundary region helps set the heat flux leaving the core. Since heat is transported by conduction in a thermal boundary layer (Bejan, 2013), the thermal conductivity of the layer sets the heat flux according to Fourier's law:

$$q = -\kappa \nabla T \tag{6.4}$$

For a given thermal conductivity and temperature gradient, Eq. 6.4 can be globally averaged to calculate the heat flux. Using a model for thermal conductivity temperature dependence of m = 0.5, and the mantle temperature profile of (Wolf et al., 2015), and an average thickness of 150 km, the total CMB heat flux is estimated to be 8.4 TW. The temperature profile used throughout the dissertation implies a CMB thermal gradient of 10 K/km, which is on the higher end of estimates. Estimates of the thermal gradient in the CMB from post-perovskite phase transition seismic reflections range from 6 to 11 K/km (Hernlund et al., 2005). Using a CMB thermal conductivity of 5.6 W/mK, the heat flux is between 5.1 and 9.3 TW. This range of values is lower than other recent estimates of heat flux (Ohta et al., 2017; Hsieh et al., 2018). Our work suggests that the inner core is older

than 1.5 Ga, which implies that preferential crystallization of an iron-rich solid inner core has played a significant role in compositional convection of the outer core. Compositional convection is more efficient than pure thermal convection in providing power to the geodynamo. This work supports a view of a long term contribution of inner core growth to the maintenance of Earths intrinsic magnetic field.

In this dissertation, I have presented new measurements of lattice thermal conductivity across pressure-induced phase transitions. The method was developed using ionic salts and NaCl thermal conductivity was measured across the B1/B2 transition for the first time. This method could be applied to other materials, including those with engineering applications to thermal management, such as rare-earth oxide insulators. Measurements of thermal conductivity from the high spin to mixed spin state of ferropericlase show a significant reduction across the spin transition. This result has now been reproduced by two other labs, using different, time-resolved techniques (Ohta et al., 2017; Hsieh et al., 2018). The reduction of thermal conductivity with pressure is an anomalous and interesting result, and is predicted by a simple model for the bulk sound speed of the material. Ferropericlase likely has only a minor impact on the depth profile of thermal conductivity through the Earth's mantle. The CMB total thermal conductivity, likewise, is relatively insensitive to anomalous behavior of ferropericlase due to the dominant contribution of brigmanite. New results published recently on the compressional wave speed of bridgmanite shows a significant reduction across the spin transition (Fu et al., 2018). This anomalous result could significantly affect transport properties, and further experiments on Fe-bearing bridgmanite, across the spin transition, are necessary.

Experimental results for the thermal conductivity of the lower mantle show increasingly good agreement on the pressure dependence of iron-bearing bridgmanite and ferropericlase.

The significant reduction across the spin transition, a major perturbation to ferropericlase thermal conductivity, does not alter the general conclusion that thermal conductivity approximately doubles from the top of the lower mantle to the CMB region. The largest discrepancies in the value of CMB thermal conductivity are due to uncertainty in the temperature dependence and radiative contribution to the total conductivity. Future work, possibly combining experiments with *ab initio* calculations, will be required to measure thermal conductivity at the combined pressure and temperature conditions of the lowermost mantle.

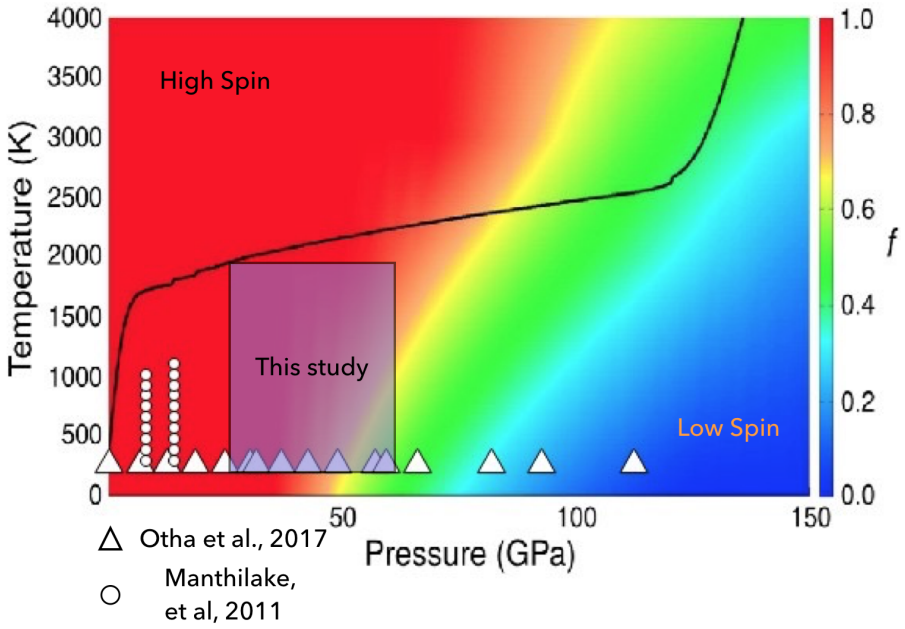

Figure 6.1: Phase diagram of the high spin state fraction of ferropericlase by *ab initio* simulation is reproduced here (Holmström and Stixrude, 2015) with pressure and temperature conditions of measurements of thermal conductivity, including this work.

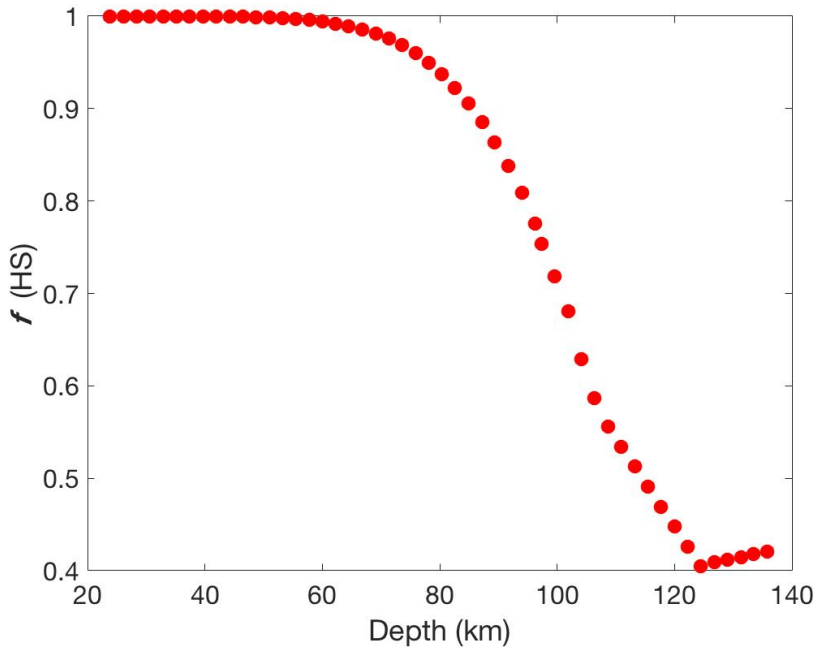

Figure 6.2: The fraction of high spin versus depth along a geothermal gradient (Wolf et al., 2015) using the calculated phase diagram of (Holmström and Stixrude, 2015), shown in Fig. 6.1

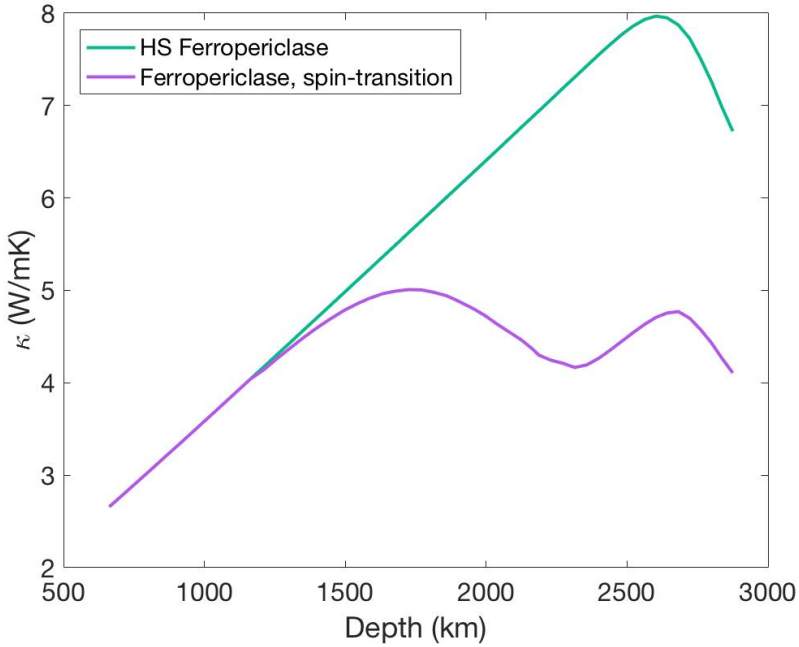

Figure 6.3: The lattice thermal conductivity of high spin ferropericlase, throughout the entire lower mantle is shown in the solid green line. The calculated mixed spin thermal conductivity profile, with a broad reduction though the lower mantle, as described in the text.

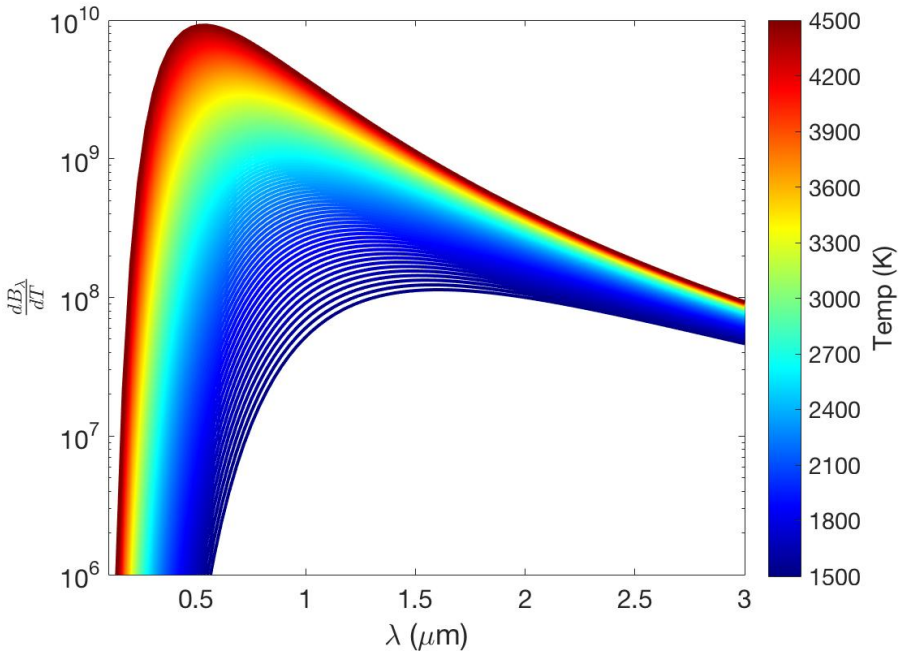

Figure 6.4: The blackbody intensity derivative with respect to temperature is plotted against wavelength for a series of temperatures between 1500 K and 4500 K. The wavelength range is over existing high pressure absorption coefficient data.

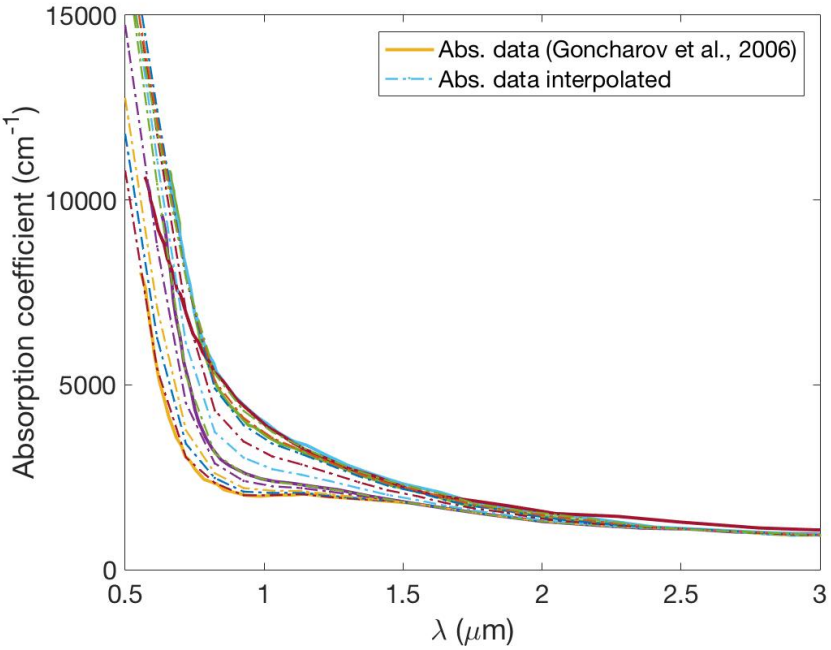

Figure 6.5: The measured absorption coefficient for $(Mg_{1-x}Fe_xO)$, with x = 0.25 from (Goncharov et al., 2006) is reproduced between 26 GPa and 74 GPa, with interpolation between each measurement along evenly spaced pressure steps.

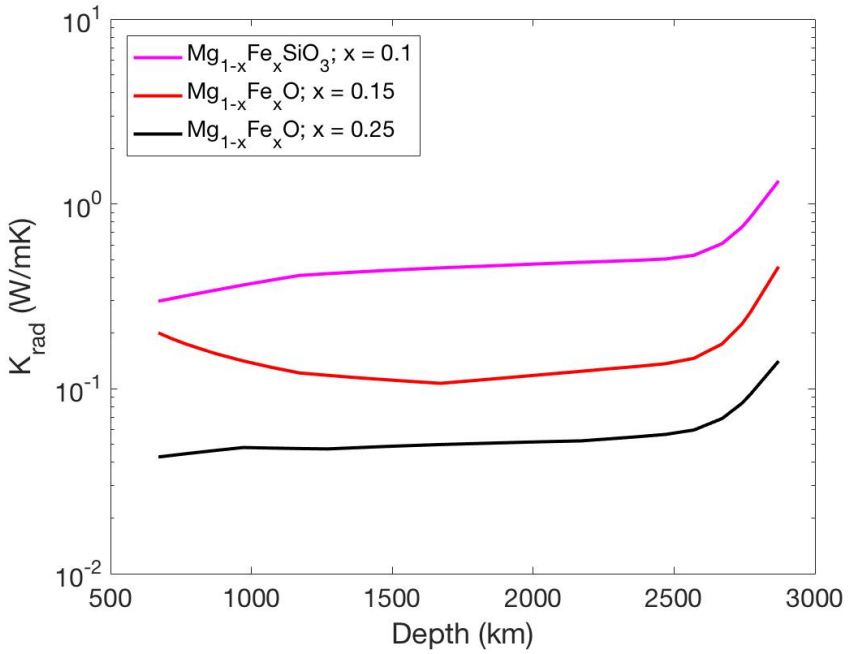

Figure 6.6: Radiative thermal conductivity of ferropericlase, ($Mg_{1-x}Fe_xO$), with x = 0.25, and x = 0.15, calculated from the absorption data (Goncharov et al., 2006, 2010), along a mantle geotherm (Wolf et al., 2015).

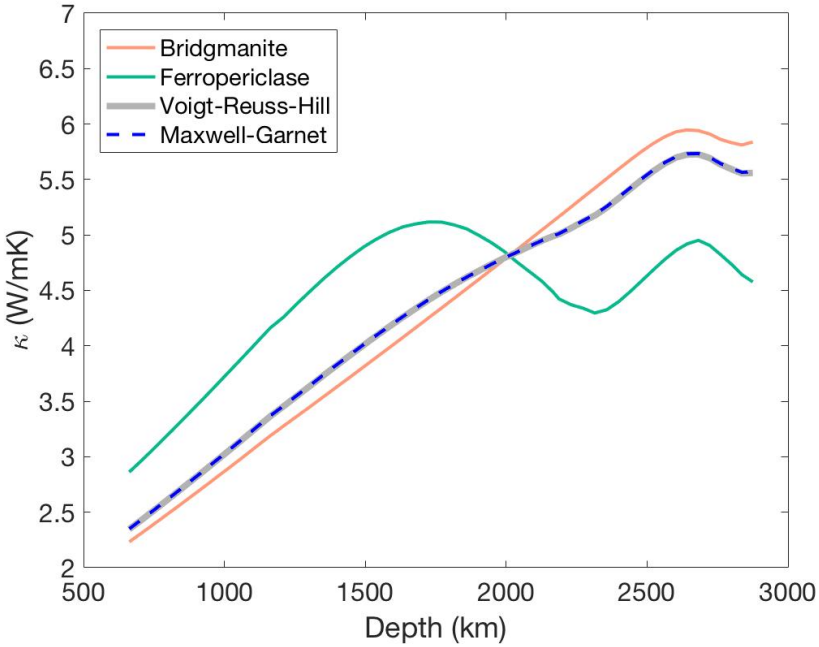

Figure 6.7: Combined lattice and radiative thermal conductivity along a geothermal profile as a function of depth in the mantle is shown for Fe-bearing bridgmanite, ferropericlase, and their volumetric average, with 80% bridgmanite and 20% ferropericlase.

Bibliography

Bejan, A., 2013. Convection heat transfer. John wiley & sons.

Cottaar, S., Heister, T., Rose, I., Unterborn, C., 2014. Burnman: A lower mantle mineral physics toolkit. Geochemistry, Geophysics, Geosystems 15, 1164–1179.

Fu, S., Yang, J., Zhang, Y., Okuchi, T., McCammon, C., Kim, H.I., Lee, S.K., Lin, J.F., 2018. Abnormal elasticity of fe-bearing bridgmanite in the earths lower mantle. Geophysical Research Letters .

Goncharov, A., Struzhkin, V., Montoya, J., Kharlamova, S., Kundargi, R., Siebert, J., Badro, J., Antonangeli, D., Ryerson, F., Mao, W., 2010. Effect of composition, structure, and spin state on the thermal conductivity of the earth's lower mantle. Physics of the Earth and Planetary Interiors 180, 148–153.

Goncharov, A.F., Haugen, B.D., Struzhkin, V.V., Beck, P., Jacobsen, S.D., 2008. Radiative conductivity in the earths lower mantle. Nature 456, 231.

Goncharov, A.F., Struzhkin, V.V., Jacobsen, S.D., 2006. Reduced radiative conductivity of low-spin (mg, fe) o in the lower mantle. Science 312, 1205–1208.

Hernlund, J.W., Thomas, C., Tackley, P.J., 2005. A doubling of the post-perovskite phase boundary and structure of the earth's lowermost mantle. Nature 434, 882.

Hofmeister, A., 1999. Mantle values of thermal conductivity and the geotherm from phonon lifetimes. Science 283, 1699–1706.

Hofmeister, A., 2014. Thermodynamic and optical thickness corrections to diffusive radiative transfer formulations with application to planetary interiors. Geophysical Research Letters 41, 3074–3080.

Holmström, E., Stixrude, L., 2015. Spin crossover in ferropericlase from first-principles molecular dynamics. Physical review letters 114, 117202.

Hsieh, W.P., Deschamps, F., Okuchi, T., Lin, J.F., 2018. Effects of iron on the lattice thermal conductivity of earths deep mantle and implications for mantle dynamics. Proceedings of the National Academy of Sciences , 201718557.

Keppler, H., Dubrovinsky, L.S., Narygina, O., Kantor, I., 2008. Optical absorption and radiative thermal conductivity of silicate perovskite to 125 gigapascals. Science 322, 1529–1532.

Manthilake, G.M., de Koker, N., Frost, D.J., McCammon, C.A., 2011. Lattice thermal conductivity of lower mantle minerals and heat flux from earths core. Proceedings of the National Academy of Sciences 108, 17901–17904.

Mao, Z., Lin, J.F., Liu, J., Prakapenka, V.B., 2011. Thermal equation of state of lower-mantle ferropericlase across the spin crossover. Geophysical Research Letters 38.

Mattern, E., Matas, J., Ricard, Y., Bass, J., 2005. Lower mantle composition and temperature from mineral physics and thermodynamic modelling. Geophysical Journal International 160, 973–990.

Ohta, K., Yagi, T., Hirose, K., Ohishi, Y., 2017. Thermal conductivity of ferropericlase in the earth's lower mantle. Earth and Planetary Science Letters 465, 29–37.

Rainey, E.S.G., 2014. The Thermal Conductivity of the Earth's Lower Mantle and Implications for Heat Flow at the Core-Mantle Boundary. University of California, Los Angeles.

Tosi, N., Yuen, D.A., de Koker, N., Wentzcovitch, R.M., 2013. Mantle dynamics with pressure-and temperature-dependent thermal expansivity and conductivity. Physics of the Earth and Planetary Interiors 217, 48–58.

Tsuchiya, T., Wentzcovitch, R.M., da Silva, C.R., de Gironcoli, S., 2006. Spin transition in magnesiowüstite in earths lower mantle. Physical Review Letters 96, 198501.

Wolf, A.S., Jackson, J.M., Dera, P., Prakapenka, V.B., 2015. The thermal equation of state of (mg, fe) sio3 bridgmanite (perovskite) and implications for lower mantle structures. Journal of Geophysical Research: Solid Earth 120, 7460–7489.